# Modelling of layered Cylindrical Dielectric Resonators with reference to Whispering Gallery Mode Resonators

K. H. Cherenack

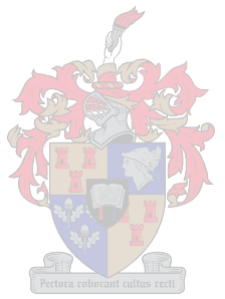


Thesis presented in Fulfillment of the requirements for the degree of Master of Engineering at the University of Stellenbosch

*Supervisor* Prof Petrie Meyer

December 2002

# Declaration

I, the undersigned, hereby declare that the work contained in this thesis is my original work and has not been previously in its entirety or in part been submitted at any university for a degree.

K. Cherenack

# Abstract

Keywords: Dielectric Resonators, Radial Mode Matching, Whispering Gallery Modes

The aim of this investigation was to develop accurate modelling techniques to determine the resonant frequencies of dielectric resonators. These resonators could be simple dielectric posts, rings or combinations of these two. To do this, a radial mode matching technique was implemented and applied to a post resonator, a ring resonator and finally a combination of the two. The resulting method was used to develop a model of a high-Q whispering gallery mode resonator consisting of a post and a ring resonator combination with an spurious free region region.

# Opsomming

Sleutelwoorde : Dielektriese Resoneerders, Radiale Modale-Pas Tegniek, 'Whispering Gallery' Modus

Die doel van hierdie navorsing was om 'n akkurate tegniek te ontwikkel om die resonante frekwensie van 'n dielektriese resoneerder vas te stel. Hierdie resoneerders kon eenvoudige resoneerders, ring resoneerders of kombinasies van die twee wees. 'n Radiale Modale-Pas tegniek is vir hierdie doel geïmplementeer en is op 'n eenvoudige resoneerder, 'n ring-resoneerder en kombinasies van die twee toegepas. Hierdie tegniek is dan gebruik om 'n hoë-Q resoneerder te ontwerp wat gebruik maak van 'n 'whispering gallery' modus. In hierdie geval is die resoneerder 'n kombinasie van 'n pil en 'n ring-resoneerder.

# Dedication

In memory of my father, Prof. Paul Cherenack

# Acknowledgements

I want to express my sincere gratitude to the people who have helped me with this thesis. This counts especially for those people who helped me without realizing it – my friends. Thank you Dien, Christine, Lize and all the rest of you for being there when I needed you.

A special word of thanks goes to Prof. Petrie Meyer for his support, encouragement and novel ideas. Without his help this thesis would never have been completed and would certainly not have been half as interesting! I also want to thank Prof. Ben Herbst for helping me out with linear systems. The same goes for all the people in my office in helping me with my program or just generally listening to my problems.

Finally, I would like to thank my mother for her unfailing belief and encouragement.

# Contents

# List of Figures

# List of Tables

## List of Abbreviations

| Abbreviation | Meaning |
|---|---|
| LMC | Longitudinal Magnetic Condition |
| LEC | Longitudinal Electric Condition |
| PEC | Perfect Electric Conductor |
| PMC | Perfect Magnetic Conductor |
| PRM | Partial Region Methods |

# Chapter 1

# Introduction

Resonators are used in many applications, such as filters, oscillators and tuned amplifiers. The most important characteristic of any resonator, aside from the resonant frequency, is the quality factor, or Q-factor. The Q-factor of a resonator is a measure of the efficiency of energy retention within a resonator, with a higher Q factor leading directly to a sharper phase transition of the impedance around the resonant frequency, and a smaller frequency band of resonant behavior. This phenomenon is also known as the selectivity of a circuit. For a detailed explanation of the quality factor, the reader is referred to Appendix A

At frequencies below 1 GHz it is possible to use lumped element circuits, which are composed of inductors and capacitors, as resonators. These can be implemented as either series or parallel LC circuits. Although lumped circuit resonators with Q factors of 1000 or more can be designed, they are only of real use at low frequencies as the properties of lumped element inductors and capacitors change at higher frequencies, as well as the loss.

At higher frequencies, microwave resonators can be constructed from closed sections of waveguide. Commonly used microwave resonators are rectangular and cylindrical metallic waveguides shorted at both ends. The electric and magnetic energy is stored in the cavity and power is mainly lost in the metallic walls. The most commonly used waveguide modes are the dominant $TE_{101}$ mode in rectangular cavities, the $TE_{111}$ mode in cylindrical cavities and the circular, low-loss $TE_{011}$ electric mode. Multiple modes can also be used in waveguide resonators, with dual-mode and triple mode used most often, but 5 modes having been demonstrated. At microwave frequencies the quality factor is proportional to volume. This means that in order to achieve high Q resonators, these waveguide resonators become increasingly bulky, expensive as well as impractical to manufacture.

In order to improve this aspect of waveguide resonators, scientists next filled them with a homogenous dielectric material. For a given Q factor, the inclusion of a dielectric leads to a size reduction of $1/\sqrt{(\epsilon_r)}$ of the dielectric filled waveguide resonator as compared to the size of an empty waveguide [17]. As the Q-factor of dielectric materials became increasingly higher, the main loss factor of resonators became due to conduction in the metallic shield. An early example

of this approach can be found in the work of George C. Southworth [27]. In his early investigations of the properties of cylindrical waveguides, he studied the behavior of these waveguides at wavelengths of 123-300 cm. As the air-filled waveguide lengths were too long to be practical, he proceeded to fill his waveguides with water $\epsilon_r = 80$ which led to a size reduction by a factor 9. The next development was to omit the metallic shield around the dielectric material, leading to a reduction in conduction losses and a corresponding increase in radiation losses from the resonator boundary. The first unmetallized dielectric objects (toroid) were investigated as resonators in 1939 by Richtmeyer [26]. In order to provide shielding for the radiation, a metallic boundary was later placed at a distance of at least twice the largest resonator dimension away from the actual dielectric resonator [10].

In the early 1960's, dielectric resonators were investigated in detail for the first time by by researchers from Columbia University, Okaya and Barash [21], [22]. The resonators were analyzed with respect to their resonant modes and resonator design. Extensive theoretical and experimental evaluations of dielectric resonators were done by Cohn and his co-workers at Rantec in the 1960s [10]. Other fundamental work on the behavior of dielectric filled waveguides and resonators was done by Van Bladel [6], [5], and [4] The dielectric material that was used by Cohn and other researchers at that time was $TiO_2$ or rutile, which had a high permittivity ($\epsilon_r \simeq 100$), but suffered from a very high temperature dependance. $TiO_2$ has a relative change of dielectric constant of about 1000 ppm/$^0$C which translates to a relative frequency change of 500 ppm/$^0$C as compared to a temperature sensitivity of 20 ppm/$^0$C for brass. This prevented the practical implementation of these resonators. The years after 1960 were mainly concerned with the development of better dielectric materials that had both high permittivities and were temperature stable. The first of these were barium tetratitanate ceramics developed by Raytheon [19] in the 1970's and barium tetratitanate with improved performance by Bell Labs [24]. These materials led to the actual implementation of dielectric resonators, but were too expensive and scarce to make these resonators commercially viable. The real breakthrough in this research came with the development of (Zr-Sn)$TiO_2$ by Murata Mfg.Co. from Japan [31]. Murata offered adjustable compositions with temperature coefficients that could be varied from +10 and -12 ppm/$^o$C. This allowed the design of commercially available dielectric resonators at reasonable prices.

The quality factor of modern dielectric resonators (usually a dielectric post resonator enclosed by a metallic sheath, which is placed at a distance from the dielectric) is limited by loss in the material and radiation losses. Typical Q factors can exceed 10 000 at 4 GHz. Commercial resonators, usually operating in TE and TM modes, have low quality factors when wavelengths approach the far infrared range. As the frequency increases, conventional dielectric resonators also become too small to be used effectively.

Dielectric resonators operating in hybrid modes avoid many of these problems. Whispering gallery modes are a family of hybrid modes that have a high angular variation. These modes were discovered in the field of acoustics by Lord Raleigh and were first investigated in resonators by J.

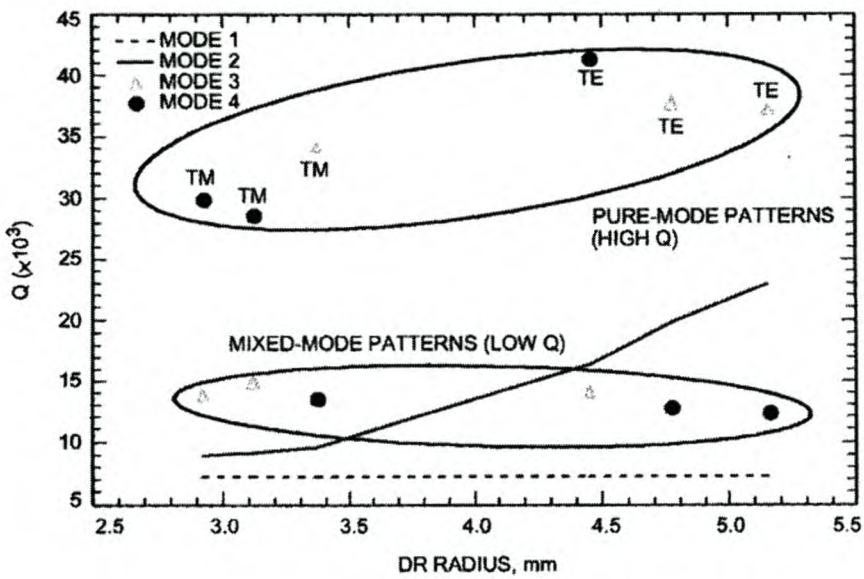


**Figure 1.1:** *A comparison of cavity Q factors between different modes [15]*

Arnaud in 1981 [29], demonstrating the possibility of using larger resonators at higher frequencies with an improvement in the Q factor. Whispering gallery modes are desirable as they have low external radiation, and the Q factor is mainly limited by the dielectric properties of the resonator itself. This means that the achievable Q factor can be very close to $Q = (\tan\delta)^{-1}$ if a proper whispering gallery mode has been established in the resonator, $\tan(\delta)$ being the loss tangent of the material.

The improved quality factor of resonators operating in whispering gallery modes was clearly demonstrated by Vedrenne and Arnaud [29]. In his paper, the intrinsic quality factor, $Q_i = \frac{40000}{f}$ was determined to be 8800 at 4.5 GHz, and the measured Q factor was 7070 at this frequency. Another investigation into the quality factor of these modes was made by Ji [15]. The simulated Q factors are shown in Figure 1.1. The figure was derived by using an simplified resonator model and implementing it using a finite-element program. In this figure modes that had a field distribution close to that of a TE mode were labelled TE, while modes which closely resembled TM modes were labelled TM. Modes that resembled neither were labelled as mixed modes. The figure clearly demonstrates the high Q factors that can be achieved using whispering gallery mode resonators.

Recently, whispering gallery modes have been used to design resonators with high Q factors, that are large enough for use at high frequencies. However, these resonators were hampered by their relatively small spurious free regions (SFR). The spurious free region can be defined as the frequency interval between the desired resonant mode and the nearest mode adjacent to it. Larger spurious free regions are essential in systems covering wider bandwidths. To improve the

spurious free region, different layered structures were implemented by Annino [1], Han [12] and Peng [23]. Both Annino and Peng made use of resonators placed above one another, centered around the z-axis. This is illustrated in Figure 1.2, where Figure 1.2(a) shows the approach by Peng and Figure 1.2(b) shows the approach by Annino. In Figure 1.2(b), the left hand figure shows the resonator with the central layer uncoupled from the outer layers, and the right hand figure shows the resonator with the central layer in direct contact with the outer layers. Peng concentrated mainly on the coupling between the two resonators. Annino discussed how an ultra wide-band resonator could be designed, whose effective frequencies differed by a factor of 20 or more.

The paper by Han [12] used a different approach, however. As can be seen in figure 1.2(c), a simple resonator was placed asymmetrically inside a ring resonator which was coupled to a straight waveguide. In this case, the frequency spectrum of the simple resonator and the ring resonator were measured individually. The SFR of the coupled structure was much larger than both the SFR of the simple resonator and the ring resonator. In fact, the SFR of the coupled resonator increased four times as compared to the disk resonator and seven times compared to the ring resonator. This remarkable achievement clearly demonstrates the advantages of using layered structures in improving the SFR.

The proposed structure is shown in Figure 1, consisting of a simple pill resonator enclosed by a ring resonator. Both resonators are centered around the z-axis. By using two resonators of different topologies, the frequency spectrum of the two will only overlap at the design frequency, hopefully creating a larger SFR. This thesis presents a mode matching technique for the analysis of layered dielectric resonating structures and can easily be generalized to any number of radial and axial layers. A similar technique is presented by Wang [30]. The analysis technique is further used to try to design a resonator with an improved SFR. Since the focus of this project is on the interaction of the dielectric resonators, the metallic sheath is moved far enough away from the ring resonator to have a minimal effect on the resonating frequency. It is important to note that the length, $l2$, of the ring resonator can be shorter than that of the post resonator. The shaded regions in Figure 1, consisting of the pill resonator and the ring resonator, is modelled as an isotropic material with a high relative permittivity, $\epsilon_r \geq 30$, and a permeability, $\mu$, equal to the permeability of free space. Figure 1 shows the equivalent circuit diagram of the proposed structure. The two parallel branch structures represent the post and the ring dielectric resonator respectively where each branch represents an individual resonance of the resonator. The ideal transformer, represented by M, models the coupling between the two resonators. Depending on which way the structure is feed and coupled into, the positions of the source and load could differ from what is shown here.

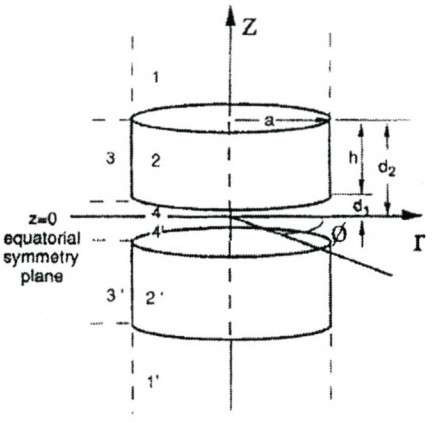


(a) The resonating structure investigated by Peng [23]

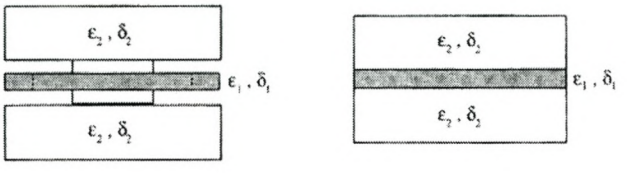


(b) The resonating structure investigated by Annino [1]. The figure shows a cut through the z-Φ axis.

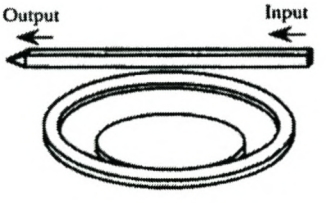


Eccentric coupled resonator

(c) The resonating structure investigated by Han [12]

**Figure 1.2:** *Different layered dielectric resonators that have been investigated in literature*

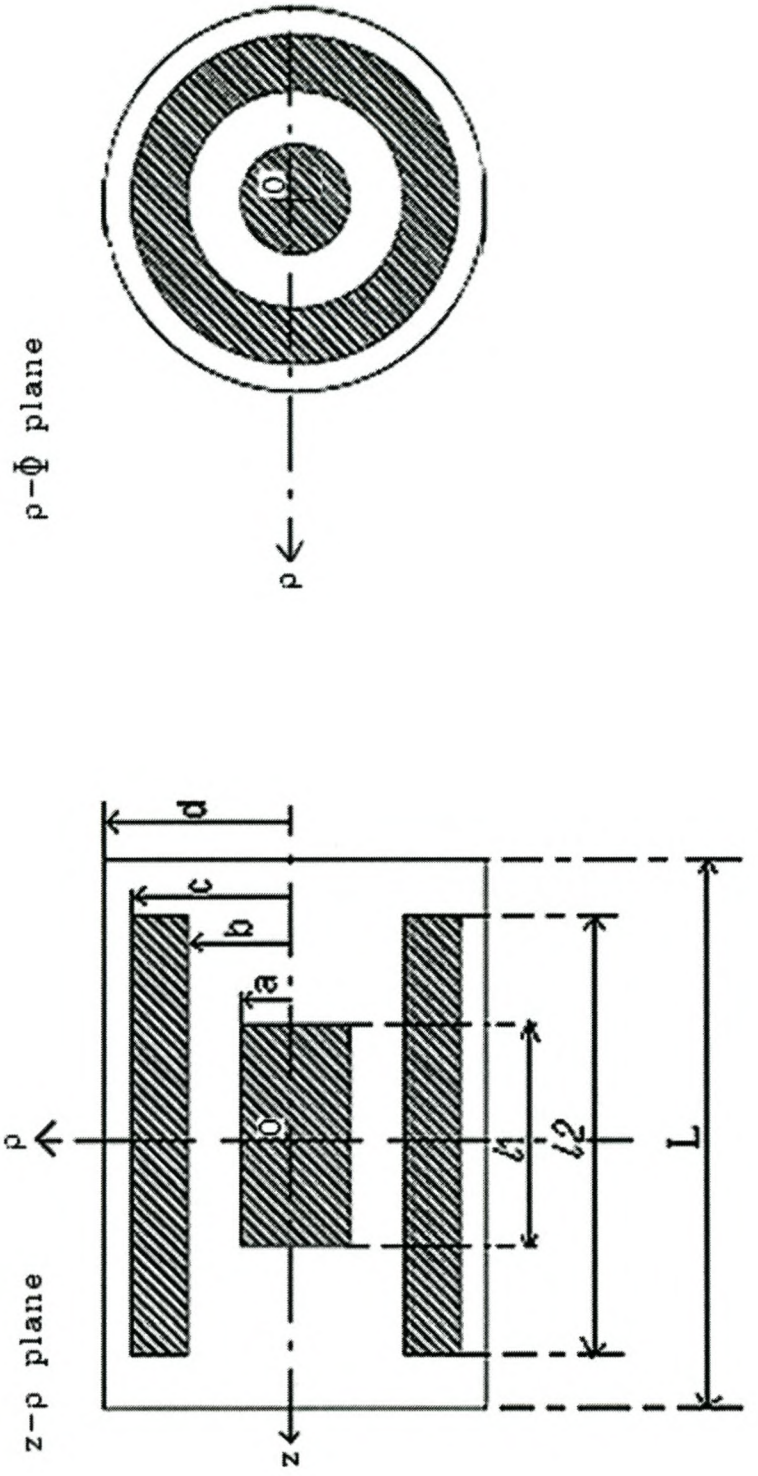


**Figure 1.3:** *The postulated resonating structure.*

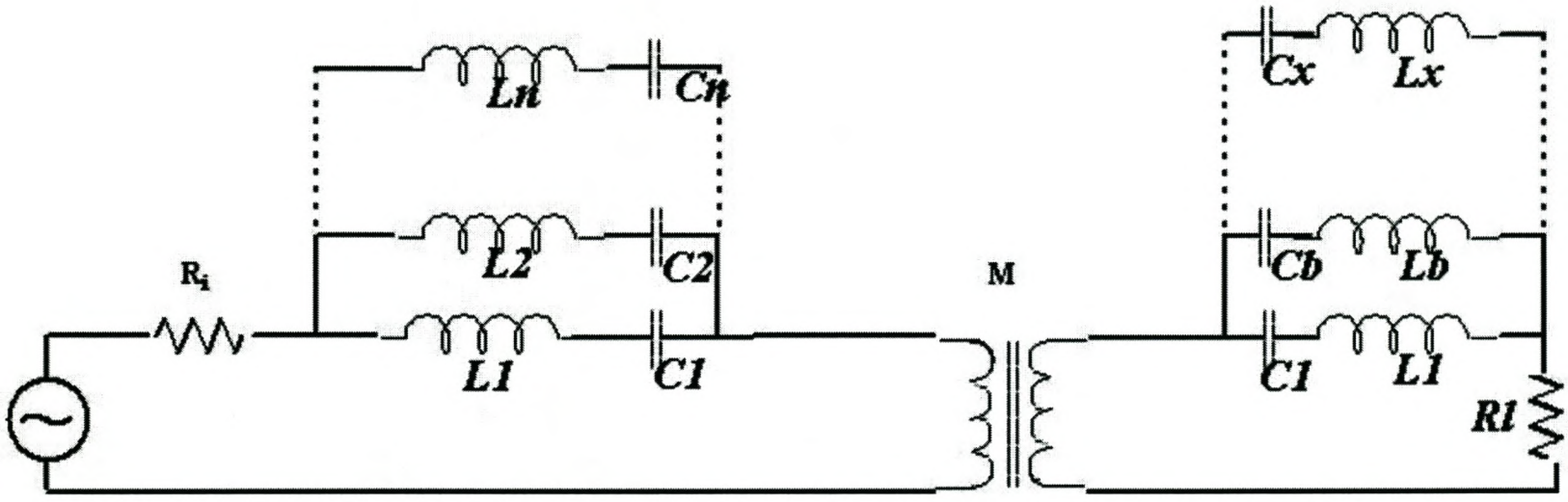


**Figure 1.4:** *Equivalent circuit diagram of the postulated resonating structure.*

This thesis is structured as follows:

Chapter 2 introduces some basic resonator concepts. The first section deals with parallel RLC resonators. These resonators are discussed with reference to their Q-factor, bandwidth and admittance. Following this the fields that can exist in cylindrical structures are derived and applied to a simple cylindrical waveguide resonator. To design an appropriate resonating structure, a modelling technique has to be developed to derive the resonant frequencies of the combined structure. The first step is to gain an understanding of the type of fields that can exist in the individual regions and at what frequencies the individual elements will resonate.

These aspects are addressed in Chapter 3. In this chapter the fields that can exist in dielectric loaded and stratified waveguides are derived. Several modelling techniques are investigated and the main technique that was implemented, radial mode matching, is discussed in detail. The results of the implementation of radial mode matching are discussed with respect to convergence and accuracy. Radial mode matching is expanded to a structure with multiple radial boundaries, which enables us to investigate the final proposed structure. Then axial mode matching is investigated and the dielectric loaded waveguide is implemented.

Now that all the necessary theory has been developed, a resonator design can be developed and is discussed in Chapter 4. A special emphasis is placed on comparison between the SFR of the combined structure and the SFR of the individual decoupled resonators (post and ring). The last chapter, Chapter 5, summarizes the research done in this report and makes recommendations of future areas of research.

# Chapter 2

# Resonators

This chapter introduces simple resonator concepts. First the parallel RLC circuit is discussed. It can be used as a rough model for most dielectric resonator circuits and is useful in explaining resonator parameters such as the Q factor and bandwidth. Following this, the cylindrical waveguide cavity resonator is presented. This is the simplest cylindrical waveguide resonator and can be modelled analytically. Many of the electromagnetic principles that are used in later chapters are introduced here. The fields that can exist in cylindrical structures are derived in a general form and then applied to a cylindrical waveguide cavity, then the admittance and Q factor at resonance are investigated.

## 2.1 Parallel Resonant Circuits

A simple resonant circuit, that demonstrates many of the qualities of cylindrical resonant cavities and dielectric resonators, is the parallel resonant circuit. It is made from discrete components and is used for applications operating below a frequency of 200 MHz. A circuit of this type is shown in Figure 2.1. The circuit is investigated with respect to its admittance, quality factor and bandwidth. The input admittance of this circuit, Y, can be written as

$$Y = \frac{1}{R} + \frac{1}{\jmath\omega L} + \jmath\omega C = G + \jmath b \tag{2.1}$$

where R = 1/G. The complex power delivered to the resonator is

$$P_G = \frac{1}{2} V I^* = \frac{1}{2}\frac{1}{Y} \mid I \mid^2 = \frac{1}{2} \mid V \mid^2 Y \tag{2.2}$$

$$= \frac{1}{2} \mid V \mid^2 (\frac{1}{R} + \frac{1}{\jmath\omega L} + \jmath\omega C)$$

and the power dissipated in the conductance G is

$$P_{loss} = \frac{1}{2}\frac{\mid V \mid^2}{R} \tag{2.3}$$

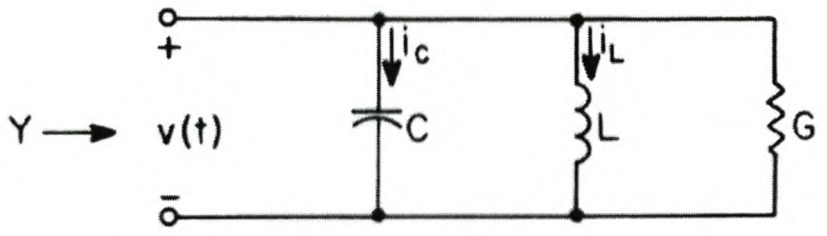


**Figure 2.1:** *Discrete components resonator [16]*

The average electric energy stored in the capacitor, C, is

$$W_e = \frac{1}{4} \mid V \mid^2 C \tag{2.4}$$

and the average magnetic energy stored in the inductor, L, is

$$W_m = \frac{1}{4} \mid I_l \mid^2 L = \frac{1}{4} \mid V \mid^2 \frac{1}{\omega^2 L} \tag{2.5}$$

where $I_l$ is the current flowing through the inductor. By substituting Equations 2.3, 2.4 and 2.5 into Equation 2.2, one can derive the following equation:

$$P_G = P_{loss} + 2\jmath\omega(W_m - W_e) \tag{2.6}$$

The input admittance can be re-written as

$$Y = \frac{\mid I \mid^2 /2}{P_{loss}} = \frac{\mid I \mid^2 /2}{P_{loss} + 2\jmath\omega(W_m - W_e)} \tag{2.7}$$

Resonance occures when $W_m = W_e$ where the complex power delivered to the circuit as described in Equation 2.6, is real and at a maximum. This also means that $Y = G$ and the admittance is purely real.

One can prove that if $W_m = W_e$ that

$$\omega_0 = \frac{1}{\sqrt{LC}} \tag{2.8}$$

and the Q factor is defined as

$$Q = \omega_0 \frac{\text{(average energy stored)}}{\text{(energy loss/second)}} = \omega_0 \frac{W_m + W_e}{P_l} = \frac{2W_e}{P_{loss}} = \omega_0 RC \tag{2.9}$$

The bandwidth, defined by the two frequency points a which the power delivered to the resonator is one half of that delivered at resonance, is solved as $B = \frac{1}{Q}$ [25]. Refer to Appendix A for a more general discussion of the quality factor and bandwidth.

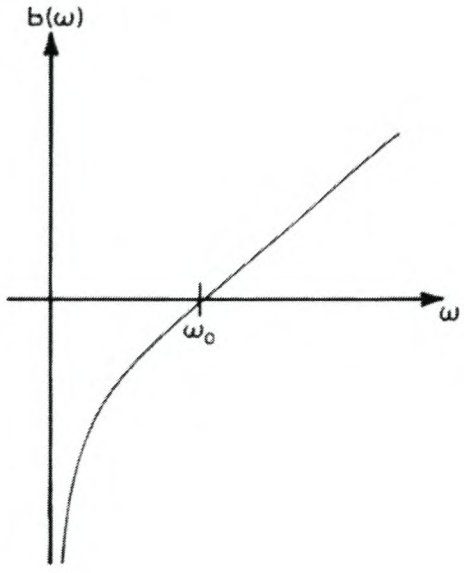


**Figure 2.2:** *Susceptance of parallel resonant circuit [16]*

If the susceptance, b, as defined in Equation 2.1 is plotted as a function of $\omega$, one obtains a graph as is shown in Figure 2.2. Two important facts can be seen from this figure. The parallel RLC circuit only has one resonance which corresponds to the susceptance zero-crossing. The gradient of the susceptance with respect to frequency can be derived as

$$\frac{d(b)}{d\omega} = C + \frac{1}{\omega^2 L} \tag{2.10}$$

Q can be written as

$$Q = \frac{RC}{\sqrt{(LC)}} = R\sqrt{\frac{C}{L}} \tag{2.11}$$

and can be increased by increasing C or decreasing L. The same is true of the gradient of the susceptance. Therefore it is true to say that an increase in the quality factor usually corresponds to an increase in the susceptance gradient (in this case an increase in R also increases the Q factor without affecting the susceptance). This means that if a circuit has a high quality factor, the resonant behavior of the circuit decreases more sharply for small frequency changes from resonance than in other circuits with lower quality factors.

If this parallel RLC circuit is now connected to an external circuit as is shown in Figure 2.3, it is possible to define two separate Q factors : $Q_0 = \omega_0 C R_L$ of the internal circuit and $Q_e = \omega_0 C R_C$ of the external circuit. The total Q factor of the circuit, $Q_L$, can be solved as

$$Q_L = \omega_0 C \frac{R_C R_L}{R_C + R_L} \tag{2.12}$$

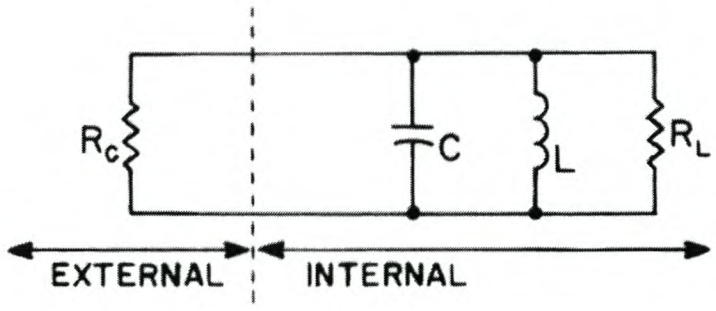


**Figure 2.3:** *Parallel RLC resonant circuit with an external load [25]*

It is easy to prove that the quality factor is dominated by the individual quality factor defined by the the largest loss. In the previous equation, if $R_l >> R_c$, then $Q_l \simeq \omega_0 C R_l$. Similarly, if $R_c >> R_l$, then $Q_l \simeq \omega_0 C R_C$. For more information on the loading effects of individual quality factors, refer to Appendix A. In the next section the theory of lossless cylindrical waveguide resonators is developed.

## 2.2 Cylindrical Waveguide Resonators

In order to investigate the behaviour of cylindrical waveguide cavities, it is necessary to derive the electric and magnetic fields. Using these fields it is then possible to investigate the internal power dissipation, stored energies and energy flow out of the cavity. A typical cylindrical cavity is shown in Figure 2.4. The first part of this section is concerned with deriving general equations

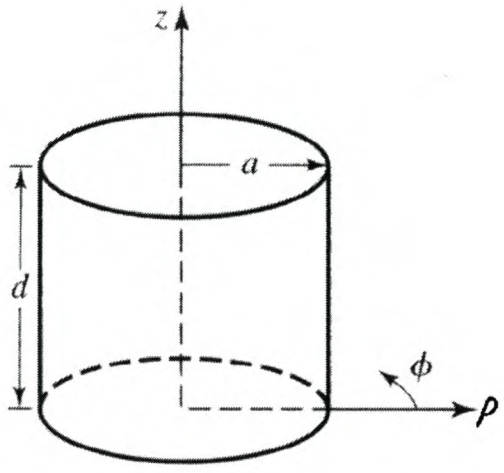


**Figure 2.4:** *A cylindrical resonant cavity [25]*

for electric and magnetic fields in cylindrical structures. Then the specific fields that can exist in a cylindrical resonator (TE and TM) are examined. Finally, the admittance and quality factor are investigated.

### 2.2.1 Fields in Cylindrical Structures

The derivation that follows is based on the work stated in Harrington [13]. The following Maxwell's equations define the electric and magnetic fields for the time-harmonic case in a source-free, homogenous region:

$$\begin{aligned} \overline{\nabla} \times \overline{H} &= \jmath\omega\epsilon\overline{E} \\ \overline{\nabla} \times \overline{E} &= -\jmath\omega\mu\overline{H} \\ \overline{\nabla} \cdot \overline{H} &= 0 \\ \overline{\nabla} \cdot (\epsilon_r \overline{E}) &= 0 \end{aligned} \tag{2.13}$$

The relative permittivity, $\epsilon_r$, is defined as

$$\epsilon_r = \frac{\epsilon_c}{\epsilon_0} = \frac{\epsilon - \jmath\frac{\sigma}{\omega}}{\epsilon_0} = \frac{\epsilon}{\epsilon_0} - \jmath\frac{\sigma}{\omega\epsilon_0} = \epsilon' - \jmath\epsilon'' \tag{2.14}$$

where $\epsilon_c$ is the complex dielectric constant of the material and $\epsilon_0 = 8.854 \times 10^{-12}$ farad/meter is the permittivity of free space. Since we are assuming a loss-less material in the interior of the cylindrical cavity, the conductivity $\sigma = 0$, and $\epsilon = \epsilon_0\epsilon_r$. The relative permeability is defined as

$$\mu_r = \frac{\mu}{\mu_0} \tag{2.15}$$

where $\mu_0 = 4\pi \times 10^{-7}$ henry/meter is the permeability of free space. We are assuming a non-magnetic material and therefore $\mu = \mu_0$ is the permeability of the material and $w = 2\pi f$.

To simplify the problem, the concept of duality is introduced. Two vector potentials are defined which correspond to electric type and magnetic type field excitations. They are $\overline{A}$, the magnetic vector potential and $\overline{F}$, the electric vector potential. $\overline{A}$ is defined by

$$\overline{H}_1 = \overline{\nabla} \times \overline{A} \tag{2.16}$$

and similarly, F is defined by

$$\overline{E}_2 = -\overline{\nabla} \times \overline{F} \tag{2.17}$$

Both potentials give rise to separate electric and magnetic fields. The total electric and magnetic fields in a structure can be derived as the summation of individual fields as follows:

$$\begin{aligned} \overline{E} &= \overline{E}_1 + \overline{E}_2 \\ \overline{H} &= \overline{H}_1 + \overline{H}_2 \end{aligned} \tag{2.18}$$

To define $\overline{A}$ uniquely, the Coulomb gauge is used and $\nabla \cdot \overline{A} = 0$ is assumed for the source free region. $\overline{A}$ can be solved as

$$\nabla^2 \overline{A} + \kappa^2 \overline{A} = 0 \text{ where } \kappa^2 = w^2 \mu\epsilon \tag{2.19}$$

using Maxwell's equations, and the fields generated by $\overline{A}$ are given as

$$\overline{E}_1 = \frac{1}{\jmath w\epsilon} \nabla \times \nabla \times \overline{A} \tag{2.20}$$

$$\overline{H}_1 = \nabla \times \overline{A} \tag{2.21}$$

Using duality, similar equations can be derived for the fields generated by $\overline{F}$ and the total fields can be derived from Equation 2.18 as:

$$\overline{E} = -\overline{\nabla} \times \overline{F} + \frac{1}{\jmath\omega\epsilon} \overline{\nabla} \times \overline{\nabla} \times \overline{A} \quad \text{with} \quad \overline{\nabla}^2 A + \kappa^2 \overline{A} = 0 \tag{2.22}$$

$$\overline{H} = \overline{\nabla} \times \overline{A} + \frac{1}{\jmath\omega\mu} \overline{\nabla} \times \overline{\nabla} \times \overline{F} \quad \text{with} \quad \overline{\nabla}^2 F + \kappa^2 \overline{F} = 0$$

This report deals with fields in cylindrical structures. Therefore the co-ordinate system indicated in Figure 2.5 was used.

**Figure 2.5:** *Cylindrical Co-ordinate System [25]*

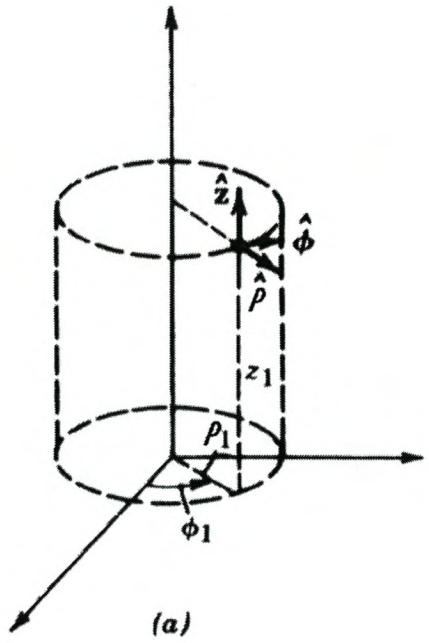


In cylindrical co-ordinates, we choose

$$\overline{A} = \Psi^a \overline{z} \tag{2.23}$$

$$\overline{F} = \Psi^f \overline{z} \tag{2.24}$$

where $\Psi^a$ and $\Psi^f$ are arbitrary scalars. This leads to the scalar Helmholtz equation by substituting Equation 2.23 into $\left(\nabla^2 + \kappa^2\right)\overline{A} = 0$ and Equation 2.24 into $\left(\nabla^2 + \kappa^2\right)\overline{F} = 0$. The Helmholtz equation for cylindrical co-ordinates is given by

$$\frac{1}{\rho}\frac{\partial}{\partial\rho}\left(\rho\frac{\partial\Psi}{\partial\rho}\right) + \frac{1}{\rho^2}\frac{\partial^2\Psi}{\partial\phi^2} + \frac{\partial^2\Psi}{\partial z^2} + \kappa^2\Psi = 0 \tag{2.25}$$

In this equation $\Psi$ can represent either $\Psi^a$ or $\Psi^f$. The electric and magnetic fields can be solved by substituting Equation 2.23 and Equation 2.24 into Equation 2.22. The field components are:

$$E_\rho = \frac{1}{\jmath\omega\epsilon}\frac{\partial^2\Psi^a}{\partial\rho\,\partial z} - \frac{1}{\rho}\frac{\partial\Psi^f}{\partial\phi} \tag{2.26}$$

$$E_\phi = \frac{1}{\jmath\omega\epsilon}\frac{1}{\rho}\frac{\partial^2\Psi^a}{\partial\phi\,\partial z} + \frac{\partial\Psi^f}{\partial\rho} \tag{2.27}$$

$$E_z = \frac{1}{\jmath\omega\epsilon}\left(\frac{\partial^2}{\partial z^2} + \kappa^2\right)\Psi^a \tag{2.28}$$

$$H_\rho = \frac{1}{\jmath\omega\mu}\frac{\partial^2\Psi^f}{\partial\rho\,\partial z} + \frac{1}{\rho}\frac{\partial\Psi^a}{\partial\phi} \tag{2.29}$$

$$H_\phi = \frac{1}{\jmath\omega\mu}\frac{1}{\rho}\frac{\partial^2\Psi^f}{\partial\phi\,\partial z} - \frac{\partial\Psi^a}{\partial\rho} \tag{2.30}$$

$$H_z = \frac{1}{\jmath\omega\mu}\left(\frac{\partial^2}{\partial z^2} + \kappa^2\right)\Psi^f \tag{2.31}$$

Equation 2.25 defines two separate sets of solutions for the electromagnetic fields. If $\Psi^a = 0$, one can see from Equation 2.28 that $E_z = 0$. These modes are also known as transverse electric or TE modes. Similarly, setting $\Psi^f = 0$ results in $H_z = 0$. These modes are defined as transverse magnetic or TM modes. The two cases are normally treated separately.

The partial differential equation, Equation 2.25, is reduced to a set of ordinary differential equations by separation of variables.

If we let $\Psi = R(\rho)\Phi(\phi)Z(z)$, Equation 2.25 can be written as

$$\frac{\rho}{R}\frac{\partial}{\partial\rho}\left(\rho\frac{\partial R}{\partial\rho}\right) + \frac{1}{\rho^2}\frac{\partial\Phi}{\partial\phi^2} + \frac{\partial Z}{\partial z^2} + \kappa^2 = 0 \tag{2.32}$$

This equation can then be split into

$$\frac{d^2Z}{dz^2} - \gamma^2 Z = 0 \tag{2.33}$$

$$\frac{d^2\Phi}{d\phi^2} + n^2\Phi = 0 \tag{2.34}$$

$$\frac{\rho}{R}\frac{d}{dr}\left(\rho\frac{dR}{d\rho}\right) - \frac{n^2}{\rho^2} + \left(\kappa^2 + \gamma^2\right)\rho^2 = 0 \tag{2.35}$$

Equation 2.35 can be re-written as

$$\frac{d^2R}{d\rho^2} + \frac{1}{\rho}\frac{dR}{d\rho} + (\beta^2 - n^2/\rho^2) \tag{2.36}$$

where $\beta^2 = \gamma^2 + \kappa^2$.

The solutions to these partial differential equations are well known. They are given by

$$Z(z) = \begin{cases} e^{\pm\gamma z} \\ \text{or} \\ \begin{pmatrix} \cosh(\gamma z) \\ \sinh(\gamma z) \end{pmatrix} \end{cases} \tag{2.37}$$

$$\Phi(\phi) \begin{cases} e^{\pm jn\phi} \\ \text{or} \\ \begin{pmatrix} \cos(n\phi) \\ \sin(n\phi) \end{pmatrix} \end{cases} \tag{2.38}$$

$$R(\rho) = \begin{cases} \begin{pmatrix} J_n(\beta\rho) \\ Y_n(\beta\rho) \end{pmatrix} \\ \text{or} \\ \begin{pmatrix} H_n^{(1)}(\beta\rho) \\ H_n^{(2)}(\beta\rho) \end{pmatrix} \end{cases} \tag{2.39}$$

$$\text{with } \beta^2 = \gamma^2 + \kappa^2 \tag{2.40}$$

If $\gamma$ becomes imaginary,

$$\beta^2 = -\gamma^2 + \kappa^2 \tag{2.41}$$

and $Z(z)$ can be derived as

$$Z(z) = \begin{cases} e^{\pm j|\gamma|z} \\ \text{or} \\ \begin{pmatrix} \cos(\gamma z) \\ \sin(\gamma z) \end{pmatrix} \end{cases} \tag{2.42}$$

It is now possible to solve for cylindrical fields in terms of functions that are only dependant on one co-ordinate, namely $R(\rho)$, $\Phi(\phi)$ and $Z(z)$, where the specific combination is determined by the problem at hand . The method used to solve for these fields is to find functions $R(\rho)$, $\Phi(\phi)$ and $Z(z)$ that satisfy the specific boundary conditions, substitute them into Equation 2.32 and solve for the individual fields components using Equations 2.26–2.31.

At this point the previously derived general equations can be applied to a specific cylindrical cavity as shown in Figure 2.4. According to convention, the modes in cylindrical waveguide cavities are labelled according to the number of field variations along the respective axes of symmetry. Each mode is labelled as either $TE_{nml}$ or $TM_{nml}$ where n refers to the number of circumferential ($\phi$) variations, $m$ refers to the number of radial ($\rho$) variations, and $l$ refers to the number of axial ($z$) variations. The TE and TM fields are dealt with separately.

### 2.2.2 TE fields

For TE fields, $\Psi^a = 0$ and from Equations 2.26 - 2.31 we can write the cylindrical cavity fields as

$$\begin{aligned} E_\rho &= -\frac{1}{\rho}\frac{\partial \Psi^f}{\partial \phi} \\ E_\phi &= \frac{\partial \Psi^f}{\partial \rho} \\ E_z &= 0 \end{aligned} \tag{2.43}$$

$$\begin{aligned} H_\rho &= \frac{1}{\jmath\omega\mu}\frac{\partial^2}{\partial \rho}\frac{\Psi^f}{\partial z} \\ H_\phi &= \frac{1}{\jmath\omega\mu}\frac{1}{\rho}\frac{\partial^2}{\partial \phi}\frac{\Psi^f}{\partial z} \\ H_z &= \frac{1}{\jmath\omega\mu}\left(\frac{\partial^2}{\partial z^2} + \kappa^2\right)\Psi^f \end{aligned} \tag{2.44}$$

From Equations 2.37, 2.38 and 2.39,

$$\begin{aligned} \Psi^f &= Z(z)\Phi(\phi)R(\rho) \\ &= (A\cos(\gamma z) + B\sin(\gamma z)) * (C\cos(n\phi) + D\sin(n\phi)) * (E\ J_n(\beta\rho) + F\ Y_n(\beta\rho)) \end{aligned} \tag{2.45}$$

The magnetic fields are now given by

$$\begin{aligned} \jmath\omega\mu H_\rho &= \beta\gamma(-A\sin(\gamma z) + B\cos(\gamma z)) * (C\cos(n\phi) + D\sin(n\phi)) \\ &\quad *(EJ_n'(\beta\rho) + FY_n'(\beta\rho)) \end{aligned} \tag{2.46}$$

$$\begin{aligned} \jmath\rho\omega\mu H_\phi &= n\gamma(-A\sin(\gamma z) + B\cos(\gamma z)) * (-C\sin(n\phi) + D\cos(n\phi)) \\ &\quad *(EJ_n(\beta\rho) + FY_n(\beta\rho)) \end{aligned} \tag{2.47}$$

$$\begin{aligned} \jmath\mu\epsilon H_z &= \beta^2(A\cos(\gamma z) + B\sin(\gamma z)) * (C\cos(n\phi) + D\sin(n\phi)) \\ &\quad *(EJ_n(\beta\rho) + FY_n(\beta\rho)) \end{aligned} \tag{2.48}$$

and the electric fields are given by

$$\begin{aligned} \rho E_\rho &= n(A\cos(\gamma z) + B\sin(\gamma z)) * (-C\sin(n\phi) + D\cos(n\phi)) \\ &\quad *(EJ_n(\beta\rho) + FY_n(\beta\rho)) \end{aligned} \tag{2.49}$$

$$\begin{aligned} E_\phi &= \beta(A\cos(\gamma z) + B\sin(\gamma z)) * (C\cos(n\phi) + D\sin(n\phi)) \\ &\quad *(EJ_n'(\beta\rho) + FY_n'(\beta\rho)) \end{aligned} \tag{2.50}$$

$$E_z = 0$$

Now we have to consider the boundary conditions. At $z = 0$ and $z = d$, the tangential electric field must be zero. Therefore, A=0 and

$$B\sin(\gamma d) = 0 \tag{2.51}$$

This means that

$$\gamma d = l\pi \quad \text{for} \quad l = 0, 1, 2, 3, ..... \tag{2.52}$$

The problem can be further subdivided by having either an electrical wall or a magnetic wall at $\phi = 0$, leading to two sets of solutions that are referred to in this report as LEC and LMC, for Longitudinal Electric Condition or Longitudinal Magnetic Condition respectively.
Therefore, for LEC at $\phi = 0$, $H_\phi(\rho, z, \phi = 0) = H_\phi(\rho, z, \phi = 2\pi) = 0$ and for LMC at $\phi = 0$, $H_z(\rho, z, \phi = 0) = H_z(\rho, z, \phi = 2\pi) = 0$. This gives $D = 0$ for LEC solutions and $C = 0$ for LMC solutions.

Now consider the $\rho$ dependency. Since $\rho = 0$ is a point at which the fields must exist, F must be zero as $Y_n(\beta\rho) = \infty$ at $\rho = 0$. At $\rho = a$, the tangential electric fields must be zero. $E_z$ is zero from the definition of TE fields. Therefore, it is left to solve for $E_\phi = \frac{\partial \Psi^f}{\partial \rho} = 0$. For this to be true,

$$\frac{d(J_n(\beta a))}{d\rho} = J_n' = 0 \tag{2.53}$$

The roots of $J_n'(x) = 0$ are defined as $r'_{nm}$, where $J_n'(r'_{nm}) = 0$ and $r'_{nm}$ is the m$th$ root of $J_n'$. This means that

$$\beta_{nm} = \frac{r'_{nm}}{a} \tag{2.54}$$

where the axial propagation constant is defined as $\gamma^2 = \beta^2 - \kappa^2$. Therefore,

$$\gamma = \sqrt{\kappa^2 - \left(\frac{r'_{nm}}{a}\right)} \tag{2.55}$$

and $\kappa = \omega\sqrt{\mu\epsilon}$.

Finally, this gives the resonant frequency as

$$f_{nml} = \frac{c}{2\pi\sqrt{\mu_r\epsilon_r}}\sqrt{\left(\frac{r'_{nm}}{a}\right)^2 + \left(\frac{l\pi}{d}\right)^2} \tag{2.56}$$

where $n = 0, 1, 2, ..,\ m = 1, 2, 3, ...$ and $l = 1, 2, 3, ....$ The frequencies defined by this equation are the resonant frequencies of the respective $TE_{nml}$ modes that can exist in the cylindrical cavity. The final wave equation can be written as

$$\Psi^f = K \sin(\frac{l\pi}{d}z) \cos(n\phi)\ J_n(\frac{r'_{nm}}{a}\rho)$$

for LEC solutions, where $K = BCE$, or

$$\Psi^f = K \sin(\frac{l\pi}{d}z) \sin(n\phi)\ J_n(\frac{r'_{nm}}{a}\rho)$$

for LMC solutions, where $K = BDE$. Only LMC exists for n=0.

The final magnetic fields are now given by

$$\begin{aligned}
\jmath\omega\mu H_\rho &= K\frac{r'_{nm}}{a}\frac{l\pi}{d}\cos(\frac{l\pi}{d}z)\cos(n\phi)J'_n(\frac{r'_{nm}}{a}\rho) \\
\jmath\rho\omega\mu H_\phi &= -Kn\frac{l\pi}{d}\cos(\frac{l\pi}{d}z) * \sin(n\phi)J_n(\frac{r'_{nm}}{a}\rho) \\
\jmath\mu\epsilon H_z &= K\left(\frac{r'_{nm}}{a}\right)^2 \sin(\frac{l\pi}{d}z) * \cos(n\phi)J_n(\frac{r'_{nm}}{a}\rho)
\end{aligned}$$

for the LEC case, where $K = BCE$ or

$$\begin{aligned}
\jmath\omega\mu H_\rho &= K\frac{r'_{nm}}{a}\frac{l\pi}{d}\cos(\frac{l\pi}{d}z)\sin(n\phi)J'_n(\frac{r'_{nm}}{a}\rho) \\
\jmath\rho\omega\mu H_\phi &= Kn\frac{l\pi}{d}\cos(\frac{l\pi}{d}z)\cos(n\phi)J_n(\frac{r'_{nm}}{a}\rho) \\
\jmath\mu\epsilon H_z &= K\left(\frac{r'_{nm}}{a}\right)^2 \sin(\frac{l\pi}{d}z)\sin(n\phi)J_n(\frac{r'_{nm}}{a}\rho)
\end{aligned}$$

for the LMC case, where $K = BDE$.

The final electric fields are given by

$$\begin{aligned}
\rho E_\rho &= Kn\sin(\frac{l\pi}{d}z)\sin(n\phi)J_n(\frac{r'_{nm}}{a}\rho) \\
E_\phi &= K\frac{r'nm}{a}\sin(\frac{l\pi}{d}z)\cos(n\phi)J'_n(\frac{r'_{nm}}{a}\rho) \\
E_z &= 0
\end{aligned} \tag{2.57}$$

for LEC and

$$\begin{aligned}
\rho E_\rho &= -Kn\sin(\frac{l\pi}{d}z)\cos(n\phi)J_n(\frac{r'_{nm}}{a}\rho) \\
E_\phi &= K\frac{r'nm}{a}\sin(\frac{l\pi}{d}z)\sin(n\phi)J'_n(\frac{r'_{nm}}{a}\rho) \\
E_z &= 0
\end{aligned} \tag{2.58}$$

for the LMC case.

### 2.2.3 TM fields

For TM fields, $\Psi^f = 0$ and from Equations 2.26 - 2.31 we can write the cylindrical cavity fields as

$$E_\rho = \frac{1}{j\omega\epsilon}\frac{\partial^2}{\partial\rho}\frac{\Psi^a}{\partial z} \tag{2.59}$$

$$E_\phi = \frac{1}{j\omega\epsilon}\frac{1}{\rho}\frac{\partial^2}{\partial\phi}\frac{\Psi^a}{\partial z} \tag{2.60}$$

$$E_z = \frac{1}{j\omega\epsilon}\left(\frac{\partial^2}{\partial z^2} + \kappa^2\right)\Psi^a$$

$$H_\rho = \frac{1}{\rho}\frac{\partial\Psi^a}{\partial\phi} \tag{2.61}$$

$$H_\phi = -\frac{\partial\Psi^a}{\partial\rho} \tag{2.62}$$

$$H_z = 0$$

From Equations 2.37, 2.38 and 2.39 we can write

$$\begin{aligned}\Psi^a &= Z(z)\Phi(\phi)R(\rho) \\ &= (A\cos(\gamma z) + B\sin(\gamma z)) * (C\cos(n\phi) + D\sin(n\phi)) * (E\ J_n(\beta\rho) + F\ Y_n(\beta\rho))\end{aligned} \tag{2.63}$$

The electric fields are given by

$$\begin{aligned}j\omega\epsilon E_\rho &= \beta\gamma(-A\sin(\gamma z) + B\cos(\gamma z)) * (C\cos(n\phi) + D\sin(n\phi)) \\ &\quad *(EJ_n'(\beta\rho) + FY_n'(\beta\rho))\end{aligned} \tag{2.64}$$

$$\begin{aligned}j\rho\omega\epsilon E_\phi &= n\gamma(-A\sin(\gamma z) + B\cos(\gamma z)) * (-C\sin(n\phi) + D\cos(n\phi)) \\ &\quad *(EJ_n(\beta\rho) + FY_n(\beta\rho))\end{aligned} \tag{2.65}$$

$$\begin{aligned}j\omega\epsilon E_z &= \beta^2(A\cos(\gamma z) + B\sin(\gamma z)) * (C\cos(n\phi) + D\sin(n\phi)) \\ &\quad *(EJ_n(\beta\rho) + FY_n(\beta\rho))\end{aligned} \tag{2.66}$$

and the magnetic fields are given by

$$\begin{aligned}\rho H_\rho &= n(A\cos(\gamma z) + B\sin(\gamma z)) * (-C\sin(n\phi) + D\cos(n\phi)) \\ &\quad *(EJ_n(\beta\rho) + FY_n(\beta\rho))\end{aligned} \tag{2.67}$$

$$\begin{aligned}H_\phi &= -\beta(A\cos(\gamma z) + B\sin(\gamma z)) * (C\cos(n\phi) + D\sin(n\phi)) \\ &\quad *(EJ_n'(\beta\rho) + FY_n'(\beta\rho))\end{aligned} \tag{2.68}$$

$$H_z = 0$$

As before, we now consider the boundary conditions. At $z = 0$ and $z = d$, the tangential electric field must be zero and A=0. Consequently

$$B\cos(\gamma d) = 0 \tag{2.69}$$

and

$$\gamma d = l\pi \quad \text{for} \quad l = 0, 1, 2, 3, ..... \tag{2.70}$$

The problem can again be further subdivided by having either an electrical wall or a magnetic wall at $\phi = 0$. For LEC at $\phi = 0$, $E_z(\rho, z, \phi = 0) = E_z(\rho, z, \phi = 2\pi) = 0$ and for LMC at $\phi = 0$, $H_\phi(\rho, z, \phi = 0) = H_\phi(\rho, z, \phi = 2\pi) = 0$. This gives $C = 0$ for LEC solutions and $D = 0$ for LMC solutions.

Only LMC fields are considered in the rest of this section. Therefore, $D = 0$. Considering the $\rho$ dependency it is possible to solve for $R(r)$. Since $\rho = 0$ is a point at which the fields must exist, constant F must be zero as $Y_n(\beta\rho) = \infty$ at $\rho = 0$. At $\rho = a$, the tangential electric fields must be zero. For this to be true,

$$J_n(\beta a) = J_n = 0 \tag{2.71}$$

The roots of $J_n(x) = 0$ are defined as $r_{nm}$, where $J_n(r_{nm}) = 0$ and $r_{nm}$ is the m$th$ root of $J_n$. This means that

$$\beta_{nm} = \frac{r_{nm}}{a} \tag{2.72}$$

The axial propagation constant is defined as $\gamma^2 = \beta^2 - \kappa^2$. and

$$\gamma = \sqrt{\kappa^2 - \left(\frac{r_{nm}}{a}\right)} \tag{2.73}$$

where $\kappa = \omega\sqrt{\mu\epsilon}$. This gives the resonant frequency as

$$f_{nml} = \frac{c}{2\pi\sqrt{\mu_r\epsilon_r}}\sqrt{\left(\frac{r_{nm}}{a}\right)^2 + \left(\frac{l\pi}{d}\right)^2} \tag{2.74}$$

where $n = 0, 1, 2, ..,$ $m = 1, 2, 3, ...$ and $l = 0, 1, 2, 3, ....$ The frequencies defined by this equation are the resonant frequencies of the respective $TM_{nml}$ modes that can exist in the cylindrical cavity. The final electric fields (LMC) are given by

$$\begin{aligned}
\jmath\omega\epsilon E_\rho &= K\frac{r_{nm}}{a}\frac{l\pi}{d}\sin(\frac{l\pi}{d}z)\cos(n\phi)J_n'(\frac{r_{nm}}{a}\rho) \\
\jmath\rho\omega\epsilon E_\phi &= -Kn\frac{l\pi}{d}\sin(\frac{l\pi}{d}z) * \sin(n\phi)J_n(\frac{r_{nm}}{a}\rho) \\
\jmath\omega\epsilon E_z &= K\left(\frac{r_{nm}}{a}\right)^2\cos(\frac{l\pi}{d}z) * \cos(n\phi)J_n(\frac{r_{nm}}{a}\rho)
\end{aligned}$$

where $K = BCE$, and the final magnetic fields (LMC) are given by

$$\begin{aligned}
\rho H_\rho &= Kn\cos(\frac{l\pi}{d}z)\sin(n\phi)J_n(\frac{r_{nm}}{a}\rho) \\
H_\phi &= -K\frac{rnm}{a}\sin(\frac{l\pi}{d}z)\cos(n\phi)J_n'(\frac{r_{nm}}{a}\rho) \\
H_z &= 0
\end{aligned} \tag{2.75}$$

Now that the TE and TM fields of a cylindrical cavity have been derived, two aspects of resonators, the admittance and quality factor, are discussed.

### 2.2.4 Admittance

For a simple, lossless, airfilled cavity, where $\epsilon = \epsilon_0$ and $\sigma = 0$, the time-average stored electric energy in a volume, V, can be written as [25]

$$W_e = \frac{\epsilon}{4} \iiint_V \mid E \mid^2 dv \tag{2.76}$$

and

$$W_m = \frac{\mu}{4} \iiint_V \mid H \mid^2 dv \tag{2.77}$$

The Poynting vector can be defined as $S = \overline{E} \times \overline{H}$ which has units of power density (watts/$m^2$). The total power, $P_e$ leaving a volume V bounded by a surface, S, can now be written as

$$P_e = \oiint_S (\overline{E} \times \overline{H}) \cdot \overline{s} = \oiint_s S \cdot d\overline{s} \tag{2.78}$$

For time-harmonic electromagnetic fields, the time-average Poynting vector is given as

$$S_{av} = \frac{1}{2} Re[\overline{E} \times \overline{H}^*] \tag{2.79}$$

We can write the complex power leaving a point as

$$\begin{aligned} \nabla \cdot (\overline{E} \times \overline{H}^*) &= \overline{H}^* \cdot \nabla \times \overline{E} - \overline{E} \cdot \nabla \times \overline{H}^* \\ &= -\jmath\omega\mu \mid \overline{H} \mid^2 + \jmath\omega\epsilon \mid \overline{E} \mid^2 \end{aligned} \tag{2.80}$$

This can be re-written in integral form as

$$\frac{1}{2} \oiint_C \overline{E} \times \overline{H}^* \cdot d\overline{s} = -2\jmath\omega \iiint_v \left\{ \frac{1}{4}\mu \mid \overline{H} \mid^2 - \frac{1}{4}\epsilon \mid \overline{E} \mid^2 \right\} dv$$

The current, I, is defined as

$$I = \oint_c \overline{H} \cdot d\overline{s} \tag{2.81}$$

and the voltage, V, is defined by

$$V = \oint_c \overline{E} \cdot d\overline{s} \tag{2.82}$$

Therefore we can write the complex power flow as

$$\begin{aligned} P_l &= \frac{1}{2} \oiint_C \overline{E} \times \overline{H}^* \cdot d\overline{s} \\ &= \frac{1}{2} \iint_{S_o} \overline{H}^* \cdot (\overline{n} \times \overline{E} ds) \\ &= -\frac{VI^*}{2} \end{aligned} \tag{2.83}$$

where $\overline{n}$ is the unit normal vector to the metallic boundary and $S_0$ is the surface of the cylindrical resonator. Using this information, and substituting the average stored electric and magnetic power into Equation 2.81, one can derive the following equation:

$$\frac{VI^*}{2} = \jmath 2\omega(W_m - W_e) \tag{2.84}$$

This means that the admittance, Y, of a cylindrical resonator can be solved as

$$\begin{aligned} Y &= \frac{I}{V} \\ &= -\jmath b \\ &= \jmath 4\omega(W_m - W_e) \end{aligned} \tag{2.85}$$

From the previously derived TE and TM fields of a cylindrical cavity resonator, it is easy to prove that $W_e = W_m$ at resonance and therefore the admittance due to loss in the cavity of a cavity resonator filled with a lossless material is zero. Of course, in a physical circuit there will still be loss due to conduction in the metallic sheath, and coupling losses. Therefore, at resonance, the admittance will have a certain real component.

If the cavity is filled with a homogenous dielectric material with $\epsilon = \epsilon_r\epsilon_0$ and the conductivity $\sigma \neq 0$, rhe complex power leaving a point now becomes

$$\begin{aligned} \nabla \cdot (\overline{E} \times \overline{H}^*) &= \overline{H}^* \cdot \nabla \times \overline{E} - \overline{E} \cdot \nabla \times \overline{H}^* \\ &= -\sigma \mid \overline{E} \mid^2 - \jmath\omega\mu \mid \overline{H} \mid^2 + \jmath\omega\epsilon \mid \overline{E} \mid^2 \end{aligned} \tag{2.86}$$

and is rewritten as

$$\begin{aligned} \frac{1}{2}\oiint_C \overline{E} \times \overline{H}^* \cdot d\overline{s} &= -\frac{1}{2}\iiint_v \sigma \mid \overline{E} \mid^2 dv \\ &\quad -2\jmath\omega \iiint_v \left\{ \frac{1}{4}\mu \mid \overline{H} \mid^2 - \frac{1}{4}\epsilon \mid \overline{E} \mid^2 \right\} dv \end{aligned} \tag{2.87}$$

Finally, the admittance is written as

$$\begin{aligned} Y &= \frac{I}{V} \\ &= G - \jmath b \\ &= \mid V \mid^{-2} \left[ \iiint_V \sigma \mid \overline{E} \mid^2 dv + \jmath 4\omega(W_m - W_e) \right] \end{aligned} \tag{2.88}$$

where the term containing $\sigma$ represents the dielectric loss. The power lost in the conducting metallic sheath is discussed in the next section which deals with the individual quality factors which can be defined in the cylindrical cavity that correspond to different types of loss.

### 2.2.5 Quality Factor

We know that

$$Q = \frac{\omega_0(W_e + W_m)}{P_l} \tag{2.89}$$

If the cavity is filled with a lossless dielectric, the losses that occur are due to conduction at the metallic boundary, and due to radiation into the external region. To solve for the conduction losses in the metallic sheath, it is necessary to solve for the power loss in the conducting walls. This is equal to [25]

$$\begin{aligned} P_c &= \frac{1}{2}\mathrm{Re}\oiint_c (\overline{E} \times \overline{H}^*) \cdot \overline{n} ds \\ &= \frac{1}{2}\mathrm{Re}\oiint_c (\overline{n} \times \overline{E}) \cdot \overline{H}^* ds \\ &= \frac{1}{2}\mathrm{Re}\oiint_c (\eta\overline{H}) \cdot \overline{H}^* ds \end{aligned} \tag{2.90}$$

where $\overline{n}$ is the unit normal vector to the metallic boundary and

$$\eta = \sqrt{\frac{\mu_o}{\epsilon}} \tag{2.91}$$

Therefore

$$P_c = \frac{\mathrm{Re}(\eta)}{2} \oiint_c |\overline{H}|^2 \, ds \tag{2.92}$$

and

$$\mathrm{Re}(\eta) = \mathrm{Re}\left[(1+j)\sqrt{\frac{\omega\mu}{2\sigma}}\right] = \sqrt{\frac{\omega\mu}{2\sigma}} = R_s \tag{2.93}$$

We now substitute this back into Equation 2.90 and derive the following equation for power loss through conduction at the metallic boundary:

$$P_c = \frac{R_s}{2} \oiint_c |\overline{H}|^2 \, ds \tag{2.94}$$

From Pozar [25] the conducting quality factor for the $TE_{nml}$ mode, $Q_c$, can be written as

$$\begin{aligned} Q_c &= \frac{\omega_0(W_e + W_m)}{P_c} \\ &= \frac{(\kappa a)^3 \eta a d}{4(r_{nm})^2 R_s} \frac{1 - \frac{n}{r_{nm}}^2}{\left\{\frac{ad}{2}\left[1 + \left(\frac{\beta a n}{(r'_{nm})^2}\right)^2\right] + \left(\frac{\beta a^2}{r'_{nm}}\right)^2 \left(1 - \frac{n^2}{(r'_n m)^2}\right)\right\}} \end{aligned} \tag{2.95}$$

If the dielectric material filling the cavity is not lossless then $\epsilon'' \neq 0$ as defined in Equation 2.14, and it is possible to define a quality factor due to power dissipation in the dielectric, $Q_d$. The power dissipated in the dielectric is given by [25]

$$\begin{aligned} P_d &= \frac{1}{2}\iiint_V \overline{J} \cdot \overline{E}^* dv \\ &= \frac{\omega\epsilon''}{2} \iiint_V || E_\rho |^2 + | E_\phi |^2 | \, dv \end{aligned} \tag{2.96}$$

Therefore we can solve for $Q_d$ as

$$Q_d = \frac{\omega(W_e + W_m)}{P_d} = \frac{\epsilon'}{\epsilon''} = \frac{1}{\tan\delta} \tag{2.97}$$

where $\tan\delta = \frac{\epsilon''}{\epsilon'}$ is defined as the loss tangent. As discussed in Section 2.1, the total quality factor is therefore

$$\frac{1}{Q} = \frac{1}{Q_c} + \frac{1}{Q_d} \tag{2.98}$$

Note that it is assumed that losses in the metallic enclosure are small enough not to affect the E and H-field distribution.

## 2.3 Conclusion

This section has discussed the resonator characteristics of cylindrical cavities which are either air-filled or filled with a homogenous dielectric material. To model a dielectric resonator one needs to investigate the behavior of cylindrical cavities that are only partially filled with a dielectric material. As soon as the material in the cavity is not homogenous, it is not longer possible to find an analytical solution for the structure. This means that some type of modelling technique has to be used to numerically solve for the resonant frequency and field distribution of the resonator.

Chapter 3 is concerned with developing the specific modelling technique that was used to investigate layered dielectric resonators. Since mode matching techniques are the dominant method used, the discussion centers around them, although other modelling techniques are briefly mentioned. Of the two main mode matching techniques, axial and radial mode matching, radial mode matching was chosen for the final implementation. In the process of developing the necessary building blocks for mode matching, the fields in dielectric loaded waveguides and two layer stratified waveguides are derived. Since the fields that exist in dielectric loaded waveguides can provide useful insights concerning the final field distributions in dielectric loaded resonators, the implementation is discussed in more detail.

# Chapter 3

# Mode Matching

## 3.1 Introduction

A dielectric resonator normally consists of a cylindrical waveguide cavity into which a dielectric material is placed. The material in the cavity is therefore no longer homogenous, and it is no longer possible to model the fields in such a structure easily. A simple example of a dielectric resonator is a cylindrical air-filled metallic cavity into which a dielectric pill resonator is introduced, as is shown in Figure 3.1.

This chapter discusses modelling techniques developed to investigate dielectric resonators. Generally, they can be divided into different categories depending on the way that the electromagnetic fields are defined in the model and what mathematical approach is implemented. Most articles only investigate these modelling techniques as applied to simple dielectric structures. The techniques described in this chapter will focus on the structure shown in Figure 3.1. In the section on radial mode matching, this technique is expanded to layered dielectric resonating structures.

Several simple methods for the modelling of dielectric resonators in the absence of conducting boundaries exist. Well-known methods are the models by Cohn, and that by Itoh and Rudokas. In the Cohn model, the walls of the dielectric resonator are replaced by a perfect magnetic wall (PMC). The fields calculated by this method can be up to 20% off the measured values and are not very useful for practical purposes. Several refinements of this model have been investigated. Results as accurate as 4.8% have been achieved and perturbational corrections to the Cohn model can improve accuracy to 0.5% for unshielded resonators [10]. Unfortunately the perturbational model is not as accurate for shielded resonators with discrepancies up to 1.5% [16]. In the Itoh and Rudokas model, a dielectric rod waveguide is modelled [14].

The fields in these simple models are only approximations of the true fields and the models are generally too inaccurate to give meaningful results. Rigorous techniques have been developed, which are capable of giving results with errors of 1 % and less. In this case, the solution

that is calculated converges towards the ideal answer as the number of field approximations in the resonating structure approaches infinity. Rigorous techniques are defined as methods where the solution that is calculated converges towards the ideal answer as the number of field approximations in the resonating structure approaches infinity. Practically, only a finite amount of approximations is used, and the solution converges towards the ideal value as the number of approximations increases.

Rigorous techniques can be subdivided according to the way in which fields are defined in the resonator regions. Partial Region Methods (PRM), define the fields in each individual resonator section. This means that the resonator is divided into radial or axial sections which can be modelled as homogenous waveguides, dielectric loaded waveguides or layered stratified waveguides, depending on the way the regions are defined. The most common method used to model shielded dielectric resonators is the mode matching technique. Other methods such as finite-element and finite-difference methods are used to solve for the resonant modes without subdividing the resonator into sections. The governing differential equation is either approximated in terms of finite differences over the whole resonator cross section or the unknown field is expanded in terms of finite elements. These methods have only been applied for axisymmetric modes. It is also possible to apply Green's free-space function in various surface or volume integration methods.

In all rigorous methods, the fields used satisfy Maxwell's equations. This gives us the following equations for the electric and magnetic fields that hold for all regions of the resonator:

$$\begin{aligned} \overline{\nabla} \times \overline{H} &= \jmath\omega\epsilon\overline{E} \\ \overline{\nabla} \times \overline{E} &= -\jmath\omega\mu\overline{H} \\ \overline{\nabla} \cdot \overline{H} &= 0 \\ \overline{\nabla} \cdot \left(\epsilon_r \overline{E}\right) &= 0 \end{aligned} \tag{3.1}$$

Following the derivation in [16], the operators L and M can be defined:

$$L = \begin{bmatrix} 0 & \overline{\nabla}\times \\ \overline{\nabla}\times & 0 \end{bmatrix} \tag{3.2}$$

$$M = \begin{bmatrix} \epsilon_0\epsilon_r\tilde{1} & 0 \\ 0 & 0 \end{bmatrix} \tag{3.3}$$

$$\overline{\Phi} = \begin{bmatrix} \overline{E} \\ \overline{H} \end{bmatrix} \tag{3.4}$$

where $\tilde{1}$ is the identity tensor of rank two.

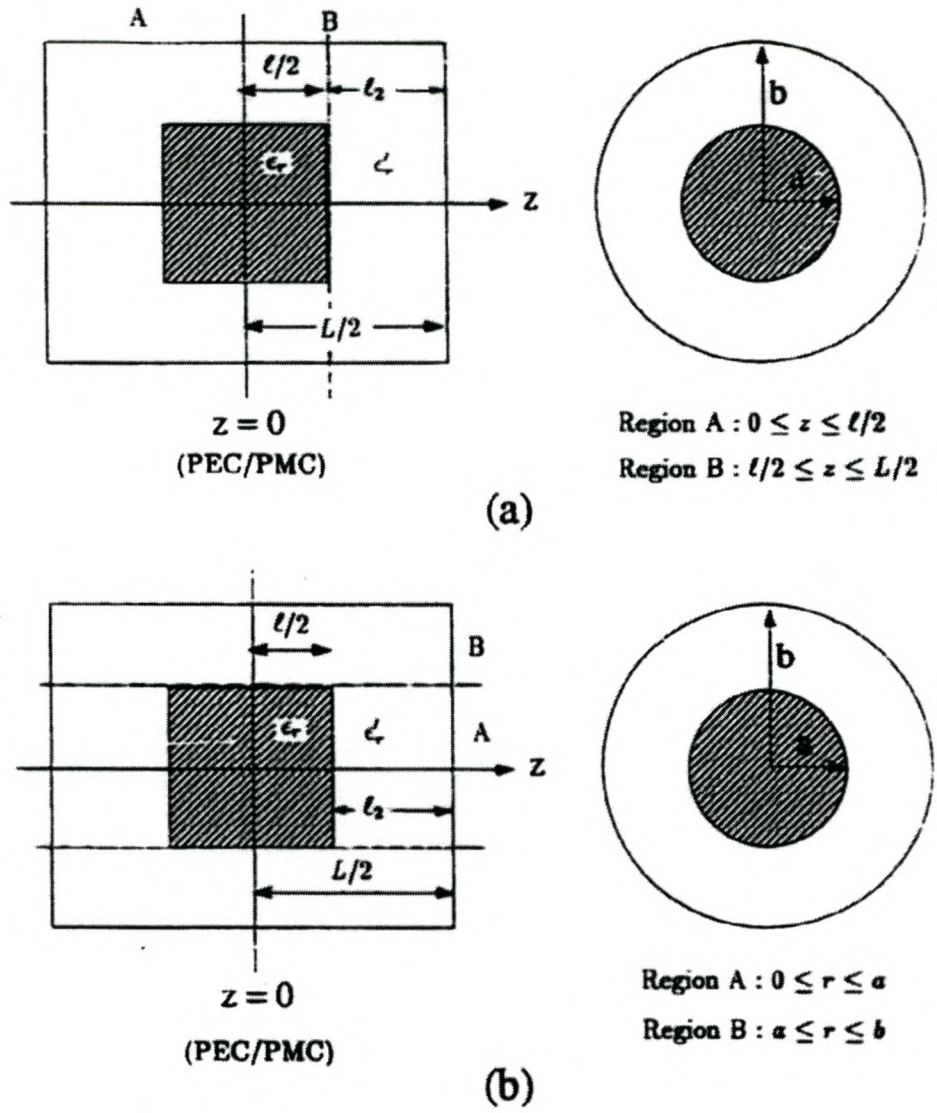


**Figure 3.1:** *A symmetric dielectric loaded resonator divided into two regions with an (a) axial boundary at $z = l/2$ and a (b) radial boundary at $\rho = a$. As defined in the text, $\epsilon_r = \epsilon_{r1}$ and $\epsilon_r' = \epsilon_{r2}$ [9]*

Using these operators, we can now rewrite Equation 3.1 as

$$\begin{aligned} L\overline{\Phi} &= \jmath\omega M\overline{\Phi} \\ \overline{n}\times\overline{E} &= \overline{0} \quad \text{on S} \end{aligned} \tag{3.5}$$

where S represents a PEC cavity with unit normal $\overline{n}$.

The operators $L$ and $M$ are self-adjoint with the inner product given by [16]

$$\langle\overline{\Phi}_1,\overline{\Phi}_2\rangle = \iiint_V (\overline{E}_1\cdot\overline{E}_2+\overline{H}_1\cdot\overline{H}_2)dV \tag{3.6}$$

For mode matching, the solution $\overline{\Phi}$ can be written as the following series

$$\overline{\Phi}=\sum_j \alpha_j\overline{f}_j \tag{3.7}$$

where $\alpha_j$ are constant coefficients to be determined and $\overline{f}_j$ are suitable basis functions. If this sum is now substituted into Equation 3.5 and the inner product is taken with respect to $f_i$ where $i=1,\ldots,N$, one can derive the following matrix eigenvalue equation:

$$\begin{aligned} L\sum_j \alpha_j\overline{f}_j &= \jmath\omega M\sum_j \alpha_j\overline{f}_j \\ \langle\overline{f}_i,L\overline{f}_j\rangle\alpha &= \jmath\omega\langle\overline{f}_i,M\overline{f}_j\rangle\alpha \end{aligned} \tag{3.8}$$

where $\alpha=[\alpha_1\ \alpha_2\ \alpha_3\ldots\alpha_N]'$. If a complete set of basis functions $\overline{f}_j$ is used, exact solutions to the original problem can be obtained. In other words, one lets $N\rightarrow\infty$. The resonant frequencies of the resonator are determined from the eigenvalues $\jmath\omega$.

In mode matching methods, the resonating system is divided into a number of regions regular enough to be solved by separation of variables of the wave equation. The fields in each partial region are represented by a series of appropriate waveguide modes with unknown coefficients. Adjacent fields are matched at the boundaries to satisfy continuity conditions, and an infinite system of simultaneous linear equations is obtained. This system has non-trivial solutions when the determinant is zero. The resonant frequencies can be found by truncating the system to a finite NxN matrix and searching for the zeros of the determinant. Mode matching techniques can be divided into different categories depending on how the regions in the structure being modelled are defined. The two most prominent methods are axial (longitudinal) and radial mode matching. These methods can be discussed with reference to Figure 3.1.

For radial mode matching, the resonating structure is divided into regions which have radial boundaries. This means that a simple dielectric resonator as is shown in Figure 3.1, will be divided into a two-layer stratified waveguide with radius $a$ and bounded by $0\leq z<l/2$ and a hollow homogenous waveguide bounded by $a<\rho\leq b$ and bounded by $l/2\leq z<L/2$. Note

that due to symmetry, the plane at $z = 0$ is modelled as either a perfect electric conductor (PEC) or as a perfect magnetic conductor (PMC). Therefore only half of the structure needs to be modelled as long as the fields in the structure satisfy the imposed boundary conditions. The fields in the inner region are those of in the two-layer stratified waveguides and the fields in the outer annular region are simply those of a cylindrical resonator where special attention has to be given to the definition of the radial function, $R(\rho)$. It is important to note that the solution in all of the regions can be written in terms of pure TM or TE modes. This is not the case for axial mode matching, as will be seen below.

In axial mode matching, the resonating structure is divided into regions with axial boundaries and the simple dielectric resonator, will be divided into a dielectric loaded waveguide waveguide bounded by $0 \leq z < l/2$ with radius $\rho = b$ and a hollow homogenous waveguide bounded by $l/2 < z \leq L/2$ with radius $\rho = b$. Again, the plane at $z = 0$ is modelled as either a perfect electric conductor (PEC) or as a perfect magnetic conductor (PMC) The fields in the dielectric loaded waveguide waveguide are the same as those derived in Section 3.3.1 and the fields in other region are those of a cylindrical air-filled resonator bounded by $l \leq z \leq L$.

When deciding which mode matching technique to implement the following issues were investigated : speed of convergence, implementation of hybrid modes and the ease of integration of the necessary field equations at the boundary.

**Convergence** It was shown by Kajfez [16], that for radial mode matching, the modes converge very slowly if their electric field components are very strong and singular at the edges of the dielectric resonator. The same was assumed to be true for axial mode matching applied to fields with a strong radial component. It was speculated that the reason for these observations was that in both cases an attempt was made to represent potentially singular functions in terms of continuous waveguide modes. From this information one can conclude that depending on which type of mode is to be investigated one method will be more effective than the other. However, since the aim of this investigation was to implement a general mode matching method to be applied to all modes, this argument was not considered to be important.

**Complex Modes** Axial mode matching techniques will result in resonator sections that are modelled as dielectric loaded waveguides. It has been found by Chen [8], that for certain frequencies, complex hybrid modes with complex propagation constants can exist in the case of infinite dielectric loaded guides as shown in Figure 3.11. When solving for the resonant frequency by matching axial modes at the boundary of a resonator, it is necessary to include these modes in the solution, as they have been shown to be linearly independent of all other propagating and evanescent modes and therefore constitute part of the complete set of solutions. Ignoring complex modes would lead to a violation of complex power conservation across the discontinuity and in the actual implementation, certain resonant modes can be missed. With the inclusion of complex axial propagation constants $\gamma$, one is left with fields that have Bessel functions with complex arguments. These lead to math-

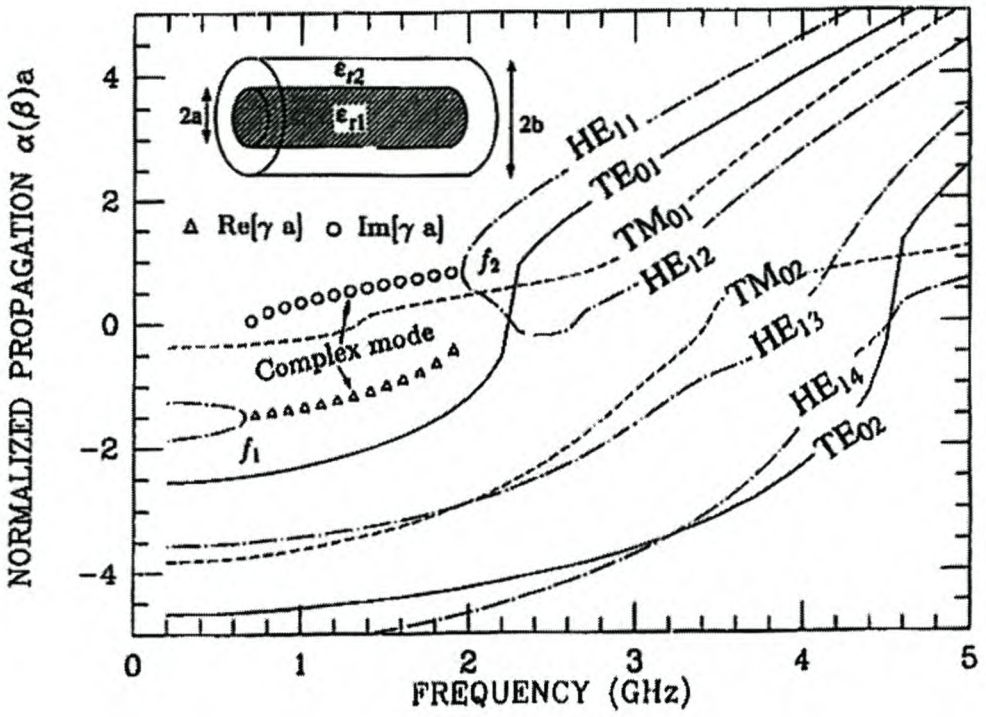


**Figure 3.2:** *$\omega - \beta$ diagram of a circular dielectric loaded waveguide. a=0.4 in., b=0.6 in., $\epsilon_{r1} = 36$ and $\epsilon_{r2} = 1$ [9]. The propagation constant is defined as $\gamma = \alpha + j\beta$ and the solutions are separated and plotted as $\alpha a$ and $\beta a$ on the same graph. Imaginary solutions are plotted as a negative real values. The zero crossings define the frequency point where the specific mode changes from imaginary to real and therefore the fields change from being evanescent to propagating.*

ematical equations that can be difficult to solve numerically. In the case of radial mode matching, the sections containing the dielectric are modelled as stratified waveguides, that have no complex hybrid modes. It should be obvious that searching a two-dimensional function-space for complex arguments will be much more time-consuming than searching along a straight line for purely real or purely imaginary solutions to the characteristic equation. Since it is difficult to predict when the hybrid modes will come into existence, such a search would have to be carried out for axial mode matching regardless of whether any complex modes exist. This aspect was considered to be a strong argument in favor of implementing radial mode matching.

**Complexity** It must also be noted that if dielectric structures which are more complex than a simple dielectric pill resonator need to be implemented, it is necessary to derive the fields equations for multiple-layered dielectric waveguides for axial mode matching. This will result in additional complexity of equations. One can also consider the behavior of the

two matching methods at the boundaries. In both cases the transverse fields have to be matched at the boundary between adjacent regions. For longitudinal mode matching, this results in integrations of products of Bessel functions over a $\rho - \phi$ plane for a fixed $z$. These integrations can be incredibly difficult to solve analytically. In comparison, for radial mode matching we are required to solve integrations of products of sinusoids over a $z - \phi$ plane for a fixed $\rho$. The answers to these equations are commonly known.

The preceding arguments indicate that is much easier to implement radial mode matching than axial mode matching and radial mode matching was therefore implemented. For completeness however, both matching methods are presented in the following sections.

This chapter starts out in Section 3.2, by describing the radial mode matching technique in detail. First the fields that can exist in two-layer stratified waveguides are derived in Section 3.2.1 and then the specific equations derived for radial mode matching are presented in Section 3.2.2. It is first applied using only one boundary, as would be the case for modelling a simple dielectric resonator. The results of the implemented technique are discussed with specific attention to convergence and accuracy in Section 3.2.2. The method is then extended to two-layer and three-layer structures in Section 3.2.3. Following this, axial mode matching is discussed in Section 3.3. First, infinite dielectric loaded waveguides are examined with respect to their fields in Section 3.3.1. The field distributions are plotted and examined in Section 3.3.2. This implementation can provide useful insights regarding the possible field distributions in simple dielectric resonators and has proved helpful in designing the final whispering gallery resonating structure. Then the theory of axial mode matching is presented in Section 3.3.3.

## 3.2 Radial Mode Matching

If radial mode matching is applied to a structure as is shown in Figure 3.1, the resulting regions are either homogenous or two-layer stratified waveguides. The fields in homogenous lossless cavities have been derived in Section 2.2. However, it is still necessary to derive the fields in a two-layer stratified dielectric waveguide.

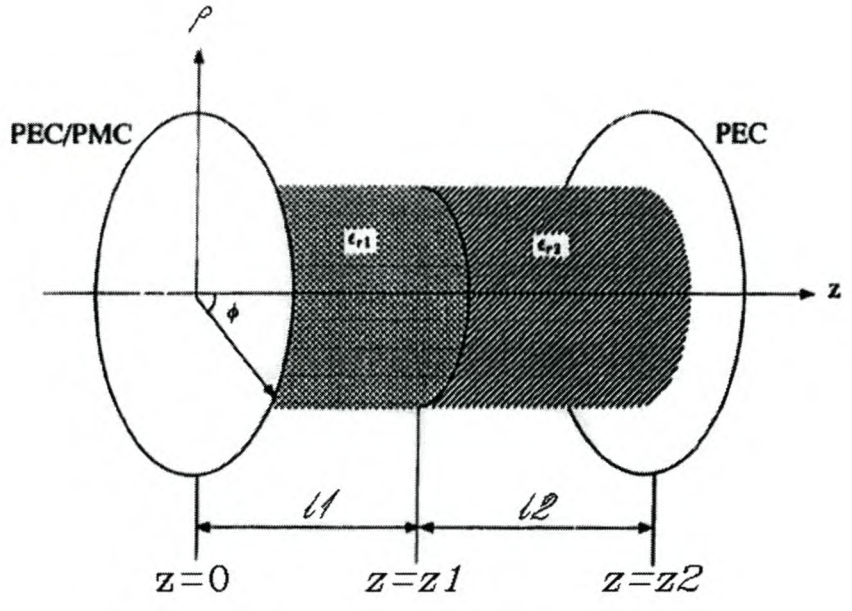


**Figure 3.3:** *A two-layered stratified dielectric waveguide. It is important to remember that the waveguide extends into infinity in the radial ρ direction [9]*

### 3.2.1 Two-layer Stratified Waveguides

A typical example of a two-layer stratified waveguide is shown in Figure 3.3. In this case it is assumed that the waveguide extends to infinity in the $\pm z$ direction. The structure is divided into 2 regions with an axial boundary, where region 1 is bounded by $0 \leq z < l_1$ and region 2 is bounded by $l_1 \leq z < L$ where $L = l_1 + l_2$. The permittivity of the dielectric material in region 1 is defined as $\epsilon_1 = \epsilon_{r1}\epsilon_0$, and the permittivity of the material in region 2 is $\epsilon_2 = \epsilon_{r2}\epsilon_0$. The fields in this structure are divided into $TE_{nm}$ or $TM_{nm}$ modes.

**TE Modes**

Starting with the general wave equation, using Equation 2.45 we can write

$$\begin{aligned}\Psi_i^f &= (A_i \sinh(\gamma_i z) + B_i \cosh(\gamma_i z)) * (C_i \cos(n\phi) + D_i \sin(n\phi)) \\ &\quad *(E_i J_n(\beta\rho) + F_i Y_n(\beta\rho))\end{aligned} \tag{3.9}$$

where $i = 1, 2$ in region 1 and 2. The structure can be divided into LEC and LMC solutions. In this derivation we choose to work with LMC fields. Therefore $C_1 = C_2 = 0$ for the TE solution. The fields must be finite at $\rho = 0$. Therefore $F_1 = F_2 = 0$ and the radial dependancy $R_1(\beta\rho) = E_1 J_n(\beta_1\rho)$ and $R_2(\beta\rho) = E_2 J_n(\beta\rho)$ where $\beta^2 = \kappa_1^2 + \gamma_1^2 = \kappa_2^2 + \gamma_2^2$. The boundary at $z = 0$ consists of either an electric (PEC) or magnetic wall (PMC).

For a PEC wall at $z = 0$, $H_{z,1} = 0$, and therefore $B_1$=0. If we assume a PMC wall, $H_{\phi,1} = 0$ which means that $A_1$=0. At $z = L$, $H_{z,2} = 0$ and therefore

$$A_2 \sinh(\gamma_2 L) + B_2 \cosh(\gamma_2 L) = 0 \tag{3.10}$$

Now we can write $A_2$ as

$$A_2 = -B_2 \frac{\sinh(\gamma_2 L)}{\cosh(\gamma_2 L)} \tag{3.11}$$

and the wave equation becomes

$$\Psi_i^f = \begin{cases} \begin{cases} \Psi_1^f = A_1 \sinh(\gamma_1 z) * C_1 \sin(n\phi) * E_1 J_n(\beta\rho) & \text{for PEC} \\ \Psi_1^f = B_1 \cosh(\gamma_1 z) * C_1 \sin(n\phi) * E_1 J_n(\beta\rho) & \text{for PMC} \end{cases} \\ \Psi_2^f = Z(z) * C_2 \sin(n\phi) * E_2 J_n(\beta\rho). \end{cases} \tag{3.12}$$

where

$$Z(z) = B_2 \left[ \frac{-\cosh(\gamma_2 L)}{\sinh(\gamma_2 L)} \sinh(\gamma_2 z) + \cosh(\gamma_2 z) \right] \tag{3.13}$$

$$= B_2 \frac{\sinh(\gamma_2 (L - z))}{\sinh(\gamma_2 L)} \tag{3.14}$$

At the interface between region 1 and region 2 at $z = l$, the tangential electric and magnetic fields must match. Therefore $H_{\phi,1} = H_{\phi,2}$ and

$$-\frac{\gamma_2}{\epsilon_2} B_2 \frac{\cosh(\gamma_2 l_2)}{\sinh(\gamma_2 L)} = \gamma_1 \begin{cases} A_1 \cosh(\gamma_1 l_1) & \text{for PEC} \\ B_1 \sinh(\gamma_1 l_1) & \text{for PMC} \end{cases} \tag{3.15}$$

where $l_2 = (L - l_1)$.

From $H_{z,1} = H_{z,2}$ we know that

$$B_2 \frac{\sinh(\gamma_2 l_2)}{\sinh(\gamma_2 L)} = \begin{cases} A_1 \sinh(\gamma_1 l_1) & \text{for PEC} \\ B_1 \cosh(\gamma_1 l_1) & \text{for PMC} \end{cases} \tag{3.16}$$

If one divides Equation 3.15 by Equation 3.16, the following equation is obtained:

$$-\gamma_2 \coth(\gamma_2 l_2) = \gamma_1 \begin{cases} \coth(\gamma_1 l_1) & \text{for PEC} \\ \tanh(\gamma_1 l_1) & \text{for PMC} \end{cases} \tag{3.17}$$

Equation 3.15 is rewritten as

$$\gamma_1 A_1 \frac{\cosh(\gamma_1 l_1)}{\sinh(\gamma_2 l_2)} = -\gamma_2 B_2 \frac{\coth(\gamma_2 l_2)}{\sinh(\gamma_2 L)} \quad \text{for PEC} \tag{3.18}$$

$$\gamma_1 B_1 \frac{\sinh(\gamma_1 l_1)}{\sinh(\gamma_2 l_2)} = -\gamma_2 B_2 \frac{\coth(\gamma_2 l_2)}{\sinh(\gamma_2 L)} \quad \text{for PMC} \tag{3.19}$$

At this point Equation 3.17 is substituted into the previous equation and this leads to

$$\frac{B_2}{\sinh(\gamma_2 L)} \gamma_1 \coth(\gamma_1 l_1) = \gamma_1 A_1 \frac{\cosh(\gamma_1 l_1)}{\sinh(\gamma_2 l_2)} \quad \text{for PEC} \tag{3.20}$$

$$\frac{B_2}{\sinh(\gamma_2 L)} \gamma_1 \tanh(\gamma_1 l_1) = \gamma_1 B_1 \frac{\sinh(\gamma_1 l_1)}{\sinh(\gamma_2 l_2)} \quad \text{for PMC} \tag{3.21}$$

This gives us

$$A_1 = \frac{\sinh(\gamma_2 l_2)}{\sinh(\gamma_1 l_1)} \frac{B_2}{\sinh(\gamma_2 L)} \tag{3.22}$$

$$B_1 = \frac{\sinh(\gamma_2 l_2)}{\cosh(\gamma_1 l_1)} \frac{B_2}{\sinh(\gamma_2 L)} \tag{3.23}$$

Now we can write the final wave equation as

$$\Psi_i^f = \begin{cases} \begin{cases} \Psi_1^f = K J_n(\beta\rho)\sin(n\phi)\frac{\sinh(\gamma_2 l_2)}{\sinh(\gamma_1 l1)}\sinh(\gamma_1 z) & \text{for PEC} \\ \Psi_1^f = K J_n(\beta\rho)\sin(n\phi)\frac{\sinh(\gamma_2 l_2)}{\cosh(\gamma_1 l1)}\cosh(\gamma_1 z) & \text{for PMC} \end{cases} \\ \Psi_2^f = K J_n(\beta\rho \sin(n\phi))\sinh(\gamma_2(L-z)). \end{cases} \tag{3.24}$$

where all the constants were combined into K. In the LEC case, the $\sin(n\phi)$ must be replaced with $\cos(n\phi)$. All the modes will be treated separately during the analysis of the resonant frequency, and constant K is used for all modes, with the assumption that K takes on different values for each mode. The electric and magnetic TE (LMC) modal fields are now calculated by

substituting $\Psi^f$ into Equations 2.26 - 2.31. This gives us the following equations:

$$H_z = \frac{K\beta^2}{j\omega\mu} J_n(\beta\rho)\sin(n\phi) * \begin{cases} \frac{\sinh(\gamma_2 l_2)}{\sinh(\gamma_1 l_1)}\sinh(\gamma_1 z) & z \le l1 \quad \text{for PEC} \\ \sinh(\gamma_2(L-z)) & z \ge l1 \quad \text{for PEC} \\ \frac{\sinh(\gamma_2 l_2)}{\cosh(\gamma_1 l_1)}\cosh(\gamma_1 z) & z \le l1 \quad \text{for PMC} \\ \sinh(\gamma_2(L-z)) & z \ge l1 \quad \text{for PMC} \end{cases} \tag{3.25}$$

$$E_\phi = K\beta J_n'(\beta\rho)\sin(n\phi) * \begin{cases} \frac{\sinh(\gamma_2 l_2)}{\sinh(\gamma_1 l_1)}\sinh(\gamma_1 z) & z \le l1 \quad \text{for PEC} \\ \sinh(\gamma_2(L-z)) & z \ge l1 \quad \text{for PEC} \\ \frac{\sinh(\gamma_2 l_2)}{\cosh(\gamma_1 l_1)}\cosh(\gamma_1 z) & z \le l1 \quad \text{for PMC} \\ \sinh(\gamma_2(L-z)) & z \ge l1 \quad \text{for PMC} \end{cases} \tag{3.26}$$

$$H_\phi = \frac{K}{j\rho\omega\mu} J_n(\beta\rho) n\cos(n\phi) * \begin{cases} \gamma_1\frac{\sinh(\gamma_2 l_2)}{\sinh(\gamma_1 l_1)}\cosh(\gamma_1 z) & z \le l1 \quad \text{for PEC} \\ -\gamma_1\cosh(\gamma_2(L-z)) & z \ge l1 \quad \text{for PEC} \\ \gamma_1\frac{\sinh(\gamma_2 l_2)}{\cosh(\gamma_1 l_1)}\sinh(\gamma_1 z) & z \le l1 \quad \text{for PMC} \\ -\gamma_2\cosh(\gamma_2(L-z)) & z \ge l1 \quad \text{for PMC} \end{cases} \tag{3.27}$$

and $E_z = 0$.

### TM Modes

Using Equation 2.63 we can write

$$\begin{aligned} \Psi_i^a = {} & (A_i\sinh(\gamma_i z) + B_i\cosh(\gamma_i z)) * (C_i\cos(n\phi) + D_i\sin(n\phi)) \\ & *(E_i J_n(\beta\rho) + F_i Y_n(\beta\rho)) \end{aligned} \tag{3.28}$$

where $i = 1, 2$ in region 1 and 2. In this derivation we choose to work with LMC fields. Therefore $D_1 = D_2 = 0$ for the TE solution. As before, the fields must be finite at $\rho = 0$ and $F_1 = F_2 = 0$. The radial dependancy $R_1(\beta\rho) = E_1 J_n(\beta_1\rho)$ and $R_2(\beta\rho) = E_2 J_n(\beta\rho)$ where $\beta^2 = \kappa_1^2 + \gamma_1^2 = \kappa_2^2 + \gamma_2^2$. The boundary at $z = 0$ consists of either an electric (PEC) or magnetic wall (PMC).

For a PEC wall at $z = 0$, $E_{\phi,1} = 0$, leading to $A_1 = 0$. For a PMC wall at $z = 0$, $E_{z,1} = 0$ and $B_1 = 0$. At $z = L$, $E_{\phi,2} = 0$ and

$$A_2\cosh(\gamma_2 L) + B_2\sinh(\gamma_2 L) = 0 \tag{3.29}$$

Therefore

$$A_2 = -B_2\frac{\sinh(\gamma_2 L)}{\cosh(\gamma_2 L)} \tag{3.30}$$

We can now re-write the wave equation as

$$\Psi_i^a = \begin{cases} \begin{cases} \Psi_1^a = B_1\cosh(\gamma_1 z) * C_1\cos(n\phi) * E_1 J_n(\beta\rho) & \text{for PEC} \\ \Psi_1^a = A_1\sinh(\gamma_1 z) * C_1\cos(n\phi) * E_1 J_n(\beta\rho) & \text{for PMC} \end{cases} \\ \Psi_2^a = Z(z) * C_2\cos(n\phi) * E_2 J_n(\beta\rho). \end{cases} \tag{3.31}$$

where

$$Z(z) = B_2\left[\frac{-\sinh(\gamma_2 L)}{\cosh(\gamma_2 L)}\sinh(\gamma_2 z) + \frac{\cosh(\gamma_2 L)}{\cosh(\gamma_2 L)}\cosh(\gamma_2 z)\right] \tag{3.32}$$

$$= B_2\frac{\cosh(\gamma_2(L-z))}{\cosh(\gamma_2 L)} \tag{3.33}$$

At the interface between region 1 and region 2 at $z = l$, the tangential electric and magnetic fields must match. Therefore $E_{\phi,1} = E_{\phi,2}$ and

$$-\frac{\gamma_2}{\epsilon_2}B_2\frac{\sinh(\gamma_2 l_2)}{\cosh(\gamma_2 L)} = \frac{\gamma_1}{\epsilon_1}\begin{cases} A_1\sinh(\gamma_1 l_1) & \text{for PEC} \\ B_1\cosh(\gamma_1 l_1) & \text{for PMC} \end{cases} \tag{3.34}$$

where $l_1 = l$ and $l_2 = (L - l)$.

From $\epsilon_{r1}E_{z,1} = \epsilon_{r2}E_{z,2}$ we know that

$$\frac{\epsilon_{r2}}{\epsilon_2}B_2\frac{\cosh(\gamma_2 l_2)}{\cosh(\gamma_2 L)} = \frac{\epsilon_{r1}}{\epsilon_1}\begin{cases} A_1\cosh(\gamma_1 l_1) & \text{for PEC} \\ B_1\sinh(\gamma_1 l_1) & \text{for PMC} \end{cases} \tag{3.35}$$

If one divides Equation 3.34 by Equation 3.35, the following equation is obtained:

$$-\frac{\epsilon_{r1}}{\epsilon_{r2}}\gamma_2\tanh(\gamma_2 l_2) = \gamma_1\begin{cases} \tanh(\gamma_1 l_1) & \text{for PEC} \\ \coth(\gamma_1 l_1) & \text{for PMC} \end{cases} \tag{3.36}$$

Now Equation 3.34 is rewritten as

$$\gamma_1 B_1\tanh(\gamma_1 l_1) = -\gamma_2\frac{\epsilon_{r1}}{\epsilon_{r2}}B_2\frac{\cosh(\gamma_2 l_2)}{\cosh(\gamma_1 l_1)}\frac{\tanh(\gamma_2 l2)}{\cosh(\gamma_2 l_2)} \quad \text{for PEC} \tag{3.37}$$

$$\gamma_1 A_1\coth(\gamma_1 l_1) = -\gamma_2\frac{\epsilon_{r1}}{\epsilon_{r2}}B_2\frac{\cosh(\gamma_2 l_2)}{\sinh(\gamma_1 l_1)}\frac{\tanh(\gamma_2 l2)}{\cosh(\gamma_2 L)} \quad \text{for PMC} \tag{3.38}$$

At this point Equation 3.36 is substituted into the previous equation and this leads to

$$B_1 = B_2\frac{\cosh(\gamma_2 l_2)}{\cosh(\gamma_1 l_1)\cosh(\gamma_2 L)} \quad \text{for PEC} \tag{3.39}$$

$$A_1 = B_2\frac{\cosh(\gamma_2 l_2)}{\sinh(\gamma_1 l_1)\cosh(\gamma_2 L)} \quad \text{for PMC} \tag{3.40}$$

Now we can write the final wave equation as

$$\Psi_i^a = \begin{cases} \begin{cases} \Psi_1^a = KJ_n(\beta\rho)\cos(n\phi)\frac{\cosh(\gamma_2 l_2)}{\cosh(\gamma_1 l1)}\cosh(\gamma_1 z) & \text{for PEC} \\ \Psi_1^a = KJ_n(\beta\rho)\cos(n\phi)\frac{\cosh(\gamma_2 l_2)}{\sinh(\gamma_1 l1)}\sinh(\gamma_1 z) & \text{for PMC} \end{cases} \\ \\ \Psi_2^a = KJ_n(\beta\rho\cos(n\phi))\cosh(\gamma_2(L-z)). \end{cases} \tag{3.41}$$

where all the constants were combined into K. In the LEC case, the $\cos(n\phi)$ must be replaced with $\sin(n\phi)$. As all the modes will be treated separately during the analysis of the resonant frequency,

the constant K is used for all modes, with the assumption that K takes on different values for each mode. The electric and magnetic TM modal fields are now calculated by substituting $\Psi^a$ into Equations 2.26 - 2.31. This gives us the following equations:

$$E_z = \frac{K\beta^2}{j\omega\epsilon_0} J_n(\beta\rho)\cos(n\phi) * \begin{cases} \frac{1}{\epsilon_{r1}}\frac{\cosh(\gamma_2 l_2)}{\cosh(\gamma_1 l_1)}\cosh(\gamma_1 z) & z \le l1 \quad \text{for PEC} \\ \frac{1}{\epsilon_{r2}}\cosh(\gamma_2(L-z)) & z \ge l1 \quad \text{for PEC} \\ \frac{1}{\epsilon_{r1}}\frac{\cosh(\gamma_2 l_2)}{\sinh(\gamma_1 l_1)}\sinh(\gamma_1 z) & z \le l1 \quad \text{for PMC} \\ \frac{1}{\epsilon_{r2}}\cosh(\gamma_2(L-z)) & z \ge l1 \quad \text{for PMC} \end{cases} \tag{3.42}$$

$$H_\phi = -K\beta J_n'(\beta\rho)\cos(n\phi) * \begin{cases} \frac{\cosh(\gamma_2 l_2)}{\cosh(\gamma_1 l_1)}\cosh(\gamma_1 z) & z \le l1 \quad \text{for PEC} \\ \cosh(\gamma_2(L-z)) & z \ge l1 \quad \text{for PEC} \\ \frac{\cosh(\gamma_2 l_2)}{\sinh(\gamma_1 l_1)}\sinh(\gamma_1 z) & z \le l1 \quad \text{for PMC} \\ \cosh(\gamma_2(L-z)) & z \ge l1 \quad \text{for PMC} \end{cases} \tag{3.43}$$

$$E_\phi = \frac{K}{j\rho\omega\epsilon_0} J_n(\beta\rho) - n\sin(n\phi) * \begin{cases} \frac{\gamma_1}{\epsilon_{r1}}\frac{\cosh(\gamma_2 l_2)}{\cosh(\gamma_1 l_1)}\sinh(\gamma_1 z) & z \le l1 \quad \text{for PEC} \\ \frac{-\gamma_1}{\epsilon_{r2}}\sinh(\gamma_2(L-z)) & z \ge l1 \quad \text{for PEC} \\ \frac{\gamma_1}{\epsilon_{r1}}\frac{\cosh(\gamma_2 l_2)}{\sinh(\gamma_1 l_1)}\cosh(\gamma_1 z) & z \le l1 \quad \text{for PMC} \\ \frac{-\gamma_2}{\epsilon_{r2}}\sinh(\gamma_2(L-z)) & z \ge l1 \quad \text{for PMC} \end{cases} \tag{3.44}$$

and $H_z = 0$

### The Characteristic Equation

In both derivations, we used only the E-field or H-field matching at $z = l$. Entering the other condition in each case leads to a characteristic equation. First consider TE modes: At the boundary $z = l_1$, $H_{\phi,1} = H_{\phi,2}$ and from the derived fields one can write the following equation

$$0 = \begin{cases} \gamma_1\frac{\sinh(\gamma_2 l_2)}{\sinh(\gamma_1 l_1)\cosh(\gamma_1 l_1)} + \gamma_2\cosh(\gamma_2 l_2) & \text{for PEC} \\ \gamma_1\frac{\sinh(\gamma_2 l_2)}{\cosh(\gamma_1 l_1)\sinh(\gamma_1 l_1)} + \gamma_2\cosh(\gamma_2 l_2) & \text{for PMC} \end{cases} \tag{3.45}$$

This can be re-written as

$$0 = \begin{cases} \gamma_1\coth(\gamma_1 l_1) + \gamma_2\coth(\gamma_2 l_2) & \text{for PEC} \\ \gamma_1\tanh\gamma_1 l_1 + \gamma_2\coth(\gamma_2 l_2) & \text{for PMC} \end{cases} \tag{3.46}$$

Using the same method for TM modes, where $E_{\phi,1} = E_{\phi,2}$ at $z = l1$, the characteristic equation is solved as

$$0 = \begin{cases} \gamma_1\tanh(\gamma_1 l_1) + \frac{\epsilon_{r1}}{\epsilon_{r2}}\gamma_2\tanh(\gamma_2 l_2) & \text{for PEC} \\ \gamma_1\coth\gamma_1 l_1 + \frac{\epsilon_{r1}}{\epsilon_{r2}}\gamma_2\tanh(\gamma_2 l_2) & \text{for PMC} \end{cases} \tag{3.47}$$

The values of $\gamma_1$ and $\gamma_2$ which satisfy these equations are the propagation constants of resonant modes which exist in the system at a particular frequency. Having derived the fields that can exist in a two-layered stratified waveguide, it is now possible to investigate the theory of radial mode matching in the next subsection.

### 3.2.2 Theory of Radial Mode Matching

The theory is explained with reference to the structure shown in Figure 3.1. Note that the resonator is surrounded by a cylindrical metallic shield. In this method, the boundary of interest is at $\rho = a$. Due to symmetry only half of the structure needs to modelled to obtain the correct results. The cylindrical region containing the dielectric resonator bounded by $0 \leq \rho \leq a$ and $0 \leq z \leq L/2$ is modelled as a two-layer stratified waveguide, where the permittivity $\epsilon_r$ is independent of the radial co-ordinate $\rho$. This will be referred to as region A and can again be divided into two parts. Part 1 containing the dielectric resonator, with permittivity $\epsilon_{A,r1}$, is adjacent to the symmetry plane $z = 0$ and has a height of $l/2$. Part 2 is filled with air and the permittivity is $\epsilon_{A,r2} = 1$. The second region is contained between $0 \leq \rho \leq b$ and $l/2 \leq z \leq L/2$. This region will be referred to as region B and is assumed to be air-filled. The transverse fields in each region are expanded in terms of cylindrical waveguide modes and tangential continuity must be enforced at the boundary $\rho = a$.

We can express the electric and magnetic fields as linear combinations of eigenmodes. In region A, the electric and magnetic fields are given as

$$\begin{aligned} \overline{E}_A(\rho,\phi,z) &= \sum_i A_i \hat{\mathrm{e}}_{Ai}(z,\phi) f^e_{Ai}(\rho) \\ \overline{H}_A(\rho,\phi,z) &= \sum_i A_i \hat{\mathrm{h}}_{Ai}(z,\phi) f^h_{Ai}(\rho) \end{aligned} \tag{3.48}$$

where $e_i$ and $h_i$ represent functions that are dependant on $z$ and $\phi$. Additionally, $f^e_i$ and $f^h_i$ are functions that are dependant on $\rho$. The fields in region B are given by

$$\begin{aligned} \overline{E}_B(\rho,\phi,z) &= \sum_j B_j \hat{\mathrm{e}}_{Bj}(z,\phi) f^e_{Bj}(\rho) \\ \overline{H}_B(\rho,\phi,z) &= \sum_j B_j \hat{\mathrm{h}}_{Bj}(z,\phi) f^h_{Bj}(\rho) \end{aligned} \tag{3.49}$$

The mode coefficients $A_i$ and $B_j$ are determined by considering the boundary conditions over the interface between the two regions. In this particular case the tangential fields must match at the boundary between the two regions. Therefore we know that

$$\overline{E}_A(\rho = a,\phi,z) = \overline{E}_B(\rho = a,\phi,z) \tag{3.50}$$

$$\overline{H}_A(\rho = a,\phi,z) = \overline{H}_B(\rho = a,\phi,z) \tag{3.51}$$

Now the cross product of Equation 3.50 with $\hat{\mathrm{h}}_{Ai}$ is taken and the entire equation is integrated over the interface, resulting in the following equation

$$A_i\langle \hat{\mathrm{e}}_{Ai}, \hat{\mathrm{h}}_{Ai}\rangle f^e_{Ai}(a) = \sum_j B_j \langle \hat{\mathrm{e}}_{Bj}, \hat{\mathrm{h}}_{Ai}\rangle f^e_{Bj}(a) \tag{3.52}$$

where the inner products are defined as

$$\begin{aligned} \langle \hat{\mathrm{e}}_{Ai}, \hat{\mathrm{h}}_{Ai}\rangle &= \int\int_s \hat{\mathrm{e}}_{Ai}(z,\phi) \times \hat{\mathrm{h}}_{Ai}(z,\phi) \cdot \overline{\rho}\; ad\phi dz \\ \langle \hat{\mathrm{e}}_{Bj}, \hat{\mathrm{h}}_{Ai}\rangle &= \int\int_s \hat{\mathrm{e}}_{Bj}(z,\phi) \times \hat{\mathrm{h}}_{Ai}(z,\phi) \cdot \overline{\rho}\; ad\phi dz \end{aligned} \tag{3.53}$$

In cylindrical co-ordinates, Equation 3.53 can be re-written as

$$\begin{aligned} \langle \hat{\mathrm{e}}_{Ai}, \hat{\mathrm{h}}_{Bj}\rangle &= \int\int_s (e_{\phi,Ai} h_{z,Bj} - e_{z,Ai} h_{\phi,Bj})\, ad\phi dz \\ \langle \hat{\mathrm{e}}_{Bj}, \hat{\mathrm{h}}_{Ai}\rangle &= \int\int_s (e_{\phi,Bj} h_{z,Ai} - e_{z,Bj} h_{\phi,Ai})\, ad\phi dz \end{aligned} \tag{3.54}$$

We also make use of the orthogonality property of eigenmodes that

$$\langle \hat{\mathrm{e}}_{Ai}, \hat{\mathrm{h}}_{Aj}\rangle = 0 \text{ for i} \neq j \tag{3.55}$$

Similarly the cross-product of Equation 3.51 is taken with $\hat{\mathrm{e}}_{Ai}$ and integrated over the interface surface, S. This results in the following equation

$$A_i\langle \hat{\mathrm{e}}_{Ai}, \hat{\mathrm{h}}_{Ai}\rangle f^h_{Ai}(a) = \sum_j B_j \langle \hat{\mathrm{e}}_{Ai}, \hat{\mathrm{h}}_{Bj}\rangle f^h_{Bj}(a) \tag{3.56}$$

From Equation 3.56 and Equation 3.52 we can derive the following homogenous linear set of equations:

$$\sum_j X_{ij} B_j = 0 \tag{3.57}$$

where

$$X_{ij} = \langle \hat{\mathrm{e}}_{Ai}, \hat{\mathrm{h}}_{Bj}\rangle f^e_{Ai}(a) f^h_{Bj}(a) - \langle \hat{\mathrm{e}}_{Bj}, \hat{\mathrm{h}}_{Ai}\rangle f^h_{Ai}(a) f^e_{Bj}(a) \tag{3.58}$$

constitute the coefficients of the linear system. In this case $i = 1 \ldots N_i$ represents the number of modes in region A and $j = 1 \ldots N_j$ represents the number of modes in region B. This systems has the following matric form

$$\begin{bmatrix} X_{11} & X_{12} & \ldots & X_{1N} \\ X_{21} & X_{22} & \ldots & X_{2N} \\ \ldots & \ldots & \ldots & \ldots \\ \ldots & \ldots & \ldots & \ldots \\ X_{N1} & X_{N2} & \ldots & X_{NN} \end{bmatrix} \begin{bmatrix} B1 \\ B2 \\ .. \\ .. \\ B_N \end{bmatrix} = \overline{X}B = 0 \tag{3.59}$$

At the points where the determinant of $\overline{X}$ is zero, the linear system has non-trivial solutions. Therefore, frequencies satisfying the equation

$$\det \overline{X} = 0 \tag{3.60}$$

are the resonant frequencies of the structure. It is necessary to use a computer to numerically solve for the linear system and therefore N must be finite. The exact solution will only be obtained if $N \to \infty$. In this case, $N = N_i = N_j$. Once the resonant frequency has been obtained, it can be substituted back into Equation 3.57 to solve for the field coefficients $A_i$ and $B_j$.

When writing the above theory in a form that can be implemented on a computer to find the resonant frequencies, the following steps are carried out:

- The fields in each region are defined.
- Using the field definitions, the inner product functions ($\hat{\mathrm{e}}_{Ai}$, $\hat{\mathrm{h}}_{Ai}$, $f^e_{Ai}$ and $f^h_{Ai}$ for region A) and the corresponding functions in region B are derived
- The inner products are solved using Equation 3.54
- The set of linear homogenous equations is set up using Equation 3.58. Now a zero finding algorithm can be used to find zeros of the determinant of the linear system defined by $\overline{X}$

### Inner Product Functions in Region A

The fields that exist in region A have been derived in Section 3.2.1. Now the $\hat{\mathrm{e}}^{TE}_{Ai}$ and $\hat{\mathrm{h}}^{TE}_{Ai}$ functions are defined.

For LMC, TE modes in region A they are

$$\hat{\mathrm{e}}^{TE}_{Ai} = E^{TE}_{\phi,Ai}(z)\sin(n\phi)\overline{\phi} \tag{3.61}$$

$$\hat{\mathrm{h}}^{TE}_{Ai} = H^{TE}_{\phi,Ai}(z)\cos(n\phi) + H^{TE}_{z,Ai}(z)\sin(n\phi)\overline{\phi} \tag{3.62}$$

where

$$\jmath\omega\mu H^{TE}_{z,Ai} = \beta^2_{Ai} * \begin{cases} \frac{\sinh(\gamma_{Ai,2}l_2)}{\sinh(\gamma_{Ai,1}l_1)}\sinh(\gamma_{Ai,1}z) & z \le l1 \quad \text{for PEC} \\ \sinh(\gamma_{Ai,2}(L-z)) & z \ge l1 \quad \text{for PEC} \\ \frac{\sinh(\gamma_{Ai,2}l_2)}{\cosh(\gamma_{Ai,1}l_1)}\cosh(\gamma_{Ai,1}z) & z \le l1 \quad \text{for PMC} \\ \sinh(\gamma_{Ai,2}(L-z)) & z \ge l1 \quad \text{for PMC} \end{cases} \tag{3.63}$$

$$\jmath\rho\omega\mu H^{TE}_{\phi,Ai} = n * \begin{cases} \gamma_{Ai,1}\frac{\sinh(\gamma_{Ai,2}l_2)}{\sinh(\gamma_{Ai,1}l_1)}\cosh(\gamma_{Ai,1}z) & z \le l1 \quad \text{for PEC} \\ -\gamma_{Ai,2}\cosh(\gamma_{Ai,2}(L-z)) & z \ge l1 \quad \text{for PEC} \\ \gamma_{Ai,1}\frac{\sinh(\gamma_{Ai,2}l_2)}{\cosh(\gamma_{Ai,1}l_1)}\sinh(\gamma_{Ai,1}z) & z \le l1 \quad \text{for PMC} \\ -\gamma_{Ai,2}\cosh(\gamma_{Ai,2}(L-z)) & z \ge l1 \quad \text{for PMC} \end{cases} \tag{3.64}$$

$$E^{TE}_{\phi,Ai} = \beta_{Ai} * \begin{cases} \frac{\sinh(\gamma_{Ai,2}l_2)}{\sinh(\gamma_{Ai,1}l_1)}\sinh(\gamma_{Ai,1}z) & z \le l1 \quad \text{for PEC} \\ \sinh(\gamma_{Ai,2}(L-z)) & z \ge l1 \quad \text{for PEC} \\ \frac{\sinh(\gamma_{Ai,2}l_2)}{\cosh(\gamma_{Ai,1}l_1)}\cosh(\gamma_{Ai,1}z) & z \le l1 \quad \text{for PMC} \\ \sinh(\gamma_{Ai,2}(L-z)) & z \ge l1 \quad \text{for PMC} \end{cases} \tag{3.65}$$

Similarly, for LMC, TM modes in region A

$$\hat{\mathrm{h}}^{TM}_{Ai} = H^{TM}_{\phi,Ai}(z)\cos(n\phi)\overline{\phi} \tag{3.66}$$

$$\hat{\mathrm{e}}^{TM}_{Ai} = E^{TM}_{\phi,Ai}(z)\sin(n\phi) + E^{TM}_{z,Ai}(z)\cos(n\phi)\overline{\phi} \tag{3.67}$$

and

$$\jmath\omega\epsilon_0 E^{TM}_{z,Ai} = \beta^2_{Ai} * \begin{cases} \frac{1}{\epsilon_{A,r1}}\frac{\cosh(\gamma_{Ai,2}l_2)}{\cosh(\gamma_{Ai,1}l_1)}\cosh(\gamma_{Ai,1}z) & z \le l1 \quad \text{for PEC} \\ \frac{1}{\epsilon_{A,r2}}\cosh(\gamma_{Ai,2}(L-z)) & z \ge l1 \quad \text{for PEC} \\ \frac{1}{\epsilon_{A,r1}}\frac{\cosh(\gamma_{Ai,2}l_2)}{\sinh(\gamma_{Ai,1}l_1)}\sinh(\gamma_{Ai,1}z) & z \le l1 \quad \text{for PMC} \\ \frac{1}{\epsilon_{A,r2}}\cosh(\gamma_{Ai,2}(L-z)) & z \ge l1 \quad \text{for PMC} \end{cases} \tag{3.68}$$

$$\jmath\rho\omega\epsilon_0 E^{TM}_{\phi,Ai} = -n * \begin{cases} \frac{\gamma_{Ai,1}}{\epsilon_{A,r1}}\frac{\cosh(\gamma_{Ai,2}l_2)}{\cosh(\gamma_{Ai,1}l_1)}\sinh(\gamma_{Ai,1}z) & z \le l1 \quad \text{for PEC} \\ \frac{-\gamma_{Ai,1}}{\epsilon_{A,r2}}\sinh(\gamma_{Ai,2}(L-z)) & z \ge l1 \quad \text{for PEC} \\ \frac{\gamma_{Ai,1}}{\epsilon_{A,r1}}\frac{\cosh(\gamma_{Ai,2}l_2)}{\sinh(\gamma_{Ai,1}l_1)}\cosh(\gamma_{Ai,z} & z \le l1 \quad \text{for PMC} \\ \frac{-\gamma_{Ai,2}}{\epsilon_{A,r2}}\sinh(\gamma_{Ai,2}(L-z)) & z \ge l1 \quad \text{for PMC} \end{cases} \tag{3.69}$$

$$H^{TM}_{\phi,Ai} = -\beta_{Ai} * \begin{cases} \frac{\cosh(\gamma_{Ai,2}l_2)}{\cosh(\gamma_{Ai,1}l_1)}\cosh(\gamma_{Ai,1}z) & z \le l1 \quad \text{for PEC} \\ \cosh(\gamma_{Ai,2}(L-z)) & z \ge l1 \quad \text{for PEC} \\ \frac{\cosh(\gamma_{Ai,2}l_2)}{\sinh(\gamma_{Ai,1}l_1)}\sinh(\gamma_{Ai,1}z) & z \le l1 \quad \text{for PMC} \\ \cosh(\gamma_{Ai,2}(L-z)) & z \ge l1 \quad \text{for PMC} \end{cases} \tag{3.70}$$

Here the subscript $i$ indicates the position of the axial or radial propagation constant with respect to the first solved root, $\gamma_{A1,1}$, $\gamma_{A1,2}$ or $\beta_{A1}$. Since region A contains the axis $z = 0$, the radial dependency $R(\beta_{Ai}\rho)$ is the same as that of the lossless cylindrical waveguide resonator discussed in Section 2.2. This gives

$$f^e_{Ai}(\rho) = J'_n(\beta_{Ai}\rho) \tag{3.71}$$
$$f^h_{Ai}(\rho) = J_n(\beta_{Ai}\rho)$$

for TE modes and

$$f^e_{Ai}(\rho) = J_n(\beta_{Ai}\rho) \tag{3.72}$$
$$f^h_{Ai}(\rho) = J'_n(\beta_{Ai}\rho)$$

for TM modes.

### Inner Product Functions in Region B

Region B consists of a ring-shaped lossless cylindrical waveguide. The fields in this regions are similar to those derived for the lossless cavity resonator in Section 2.2 with two exceptions. Due to the fact that the resonator is divided into two symmetrical halves at $z = 0$, another solution set is possible depending on whether the wall of symmetry is defined as PEC or PMC. Also, the fields need not exist at $\rho = 0$ which results in a change in the radial function, $R(\rho)$, as will be discussed below.

The fields in the cylindrical cavity resonator are bounded by a metallic sheath, and therefore all boundary walls are assumed to be PEC. For the dielectric resonator the $z = 0$ plane is replaced by either a PEC or PMC wall. Therefore, when modelling region B as cylindrical waveguide, one of the end walls can be replaced by a PMC wall. For TE modes $Z(z) = \sin(\gamma z)$ for a PEC boundary at $z = 0$ and $Z(z) = \cos(\gamma z)$ for a PMC boundary at $z = 0$. Similarly, for TM modes, $Z(z) = \cos(\gamma z)$ for a PEC boundary at $z = 0$ and $Z(z) = \sin(\gamma z)$ for a PMC boundary at $z = 0$. In order to obtain axial dependencies that are similar to those in region A, the $\sin(\gamma z)$ and $\cos(\gamma z)$ terms are replaced by $\sinh(\zeta z)$ and $\cosh(\zeta z)$ where $\zeta = \jmath\gamma$. By making use of Equations 2.43 and 2.44 for TE modes and Equations 2.59 and 2.61 for TM modes, the $\hat{\mathrm{e}}_{Bj}^{TE}$ and $\hat{\mathrm{h}}_{Bj}^{TE}$ functions are derived for region B. We find that

$$\begin{aligned} \hat{\mathrm{e}}_{Bj}^{TE} &= E_{\phi,Bj}^{TE}(z)\sin(n\phi)\overline{\phi} \\ \hat{\mathrm{h}}_{Bj}^{TE} &= H_{\phi,Bj}^{TE}(z)\cos(n\phi) + H_{z,Bj}^{TE}(z)\sin(n\phi)\overline{\phi} \end{aligned} \tag{3.73}$$

for LMC, TE modes in region B where

$$\begin{aligned} \jmath\omega\mu H_z^{TE} &= \beta_{Bj}^2 \begin{cases} \sinh(\zeta_{Bj}z) & \text{for PEC} \\ \cosh(\zeta_{Bj}z) & \text{for PMC} \end{cases} \\ \jmath\rho\omega\mu H_\phi^{TE} &= n\zeta_{Bj} \begin{cases} \cosh(\zeta_{Bj}z) & \text{for PEC} \\ \sinh(\zeta_{Bj}z) & \text{for PMC} \end{cases} \\ E_\phi^{TE} &= \beta_{Bj} \begin{cases} \sinh(\zeta_{Bj}z) & \text{for PEC} \\ \cosh(\zeta_{Bj}z) & \text{for PMC} \end{cases} \end{aligned} \tag{3.74}$$

Similarly, we can derive that,

$$\begin{aligned} \hat{\mathrm{h}}_{Bj}^{TM} &= H_{\phi,Bj}^{TM}(z)\cos(n\phi)\overline{\phi} \\ \hat{\mathrm{e}}_{Bj}^{TM} &= E_{\phi,Bj}^{TM}(z)\sin(n\phi) + E_{z,Bj}^{TM}(z)\cos(n\phi)\overline{\phi} \end{aligned} \tag{3.75}$$

where for LMC, TM modes in region B, where

$$\begin{aligned} \jmath\omega\epsilon_B E_z^{TM} &= \beta_{Bj}^2 \begin{cases} \cosh(\zeta_{Bj}z) & \text{for PEC} \\ \sinh(\zeta_{Bj}z) & \text{for PMC} \end{cases} \\ \jmath\rho\omega\epsilon_B E_\phi^{TM} &= -n\zeta_{Bj} \begin{cases} \sinh(\zeta_{Bj}z) & \text{for PEC} \\ \cosh(\zeta_{Bj}z) & \text{for PMC} \end{cases} \\ H_\phi^{TM} &= -\beta_{Bj} \begin{cases} \cosh(\zeta_{Bj}z) & \text{for PEC} \\ \sinh(\zeta_{Bj}z) & \text{for PMC} \end{cases} \end{aligned} \tag{3.76}$$

where the subscript $j$ indicates the position of the axial or radial propagation constant with respect to the first solved root, $\zeta_{Bj}$ or $\beta_{Bj}$.

Due to the fact that $\rho = 0$ is not contained in region B, the general radial dependency of the scalar potential defined by Equation 2.2.1, where $\Psi = \Psi_f$ for TE modes and $\Psi = \Psi_a$ for TM modes, is defined as follows:

$$R(\rho) = E\ J_n(\beta\rho) + F\ Y_n(\beta\rho) \tag{3.77}$$

Therefore if the boundary condition at $\rho = b$ is applied, the following equations are derived

$$R(b) = E\ J_n(\beta b) + F\ Y_n(\beta b) \tag{3.78}$$

For TE modes, $dR(\rho)/d\rho\ |_{(\rho=b)} = 0$ and therefore

$$E\ J_n'(\beta b) + F\ Y_n'(\beta b) = 0 \tag{3.79}$$

gives us

$$\begin{aligned} R(\rho) &= E\ (J_n(\beta\rho) - \frac{J_n'(\beta b)}{Y'n(\beta b)} Y_n(\beta\rho)) \\ &= \frac{E}{J'n(\beta b)} \left(J_n(\beta\rho)Y_n'(\beta b) - Y_n(\beta\rho)J_n'(\beta b)\right) \end{aligned} \tag{3.80}$$

For TM modes $R(\rho)\ |_{(\rho=b)} = 0$ and therefore

$$E\ J_n(\beta b) + F\ Y_n(\beta b) = 0 \tag{3.81}$$

and

$$\begin{aligned} R(\rho) &= E\ (J_n(\beta\rho) - \frac{J_n(\beta b)}{Y_n(\beta b)} Y_n(\beta\rho)) \\ &= \frac{E}{Jn(\beta b)} \left(J_n(\beta\rho)Y_n(\beta b) - Y_n(\beta\rho)J_n(\beta b)\right) \end{aligned} \tag{3.82}$$

Therefore we determine that

$$\begin{aligned} f_{Bj}^e(\rho) &= J_n'(\beta_{Bj}\rho)Y_n'(\beta_{Bj}b) - Y_n'(\beta\rho)J_n'(\beta_{Bj}b) \\ f_{Bj}^h(\rho) &= J_n(\beta_{Bj}\rho)Y_n'(\beta_{Bj}b) - Y_n(\beta_{Bj}\rho)J_n'(\beta_{Bj}b) \end{aligned} \tag{3.83}$$

for TE modes and

$$\begin{aligned} f^e_{Bj}(\rho) &= J_n(\beta_{Bj}\rho)Y_n(\beta_{Bj}b) - Y_n(\beta\rho)J_n(\beta_{Bj}b) \\ f^h_{Bj}(\rho) &= J'_n(\beta_{Bj}\rho)Y_n(\beta_{Bj}b) - Y'_n(\beta_{Bj}\rho)J_n(\beta_{Bj}b) \end{aligned} \tag{3.84}$$

for TM modes.

It is important to note that as the value of the radial propagation constant changes from real to imaginary, $\beta^2 = -\gamma^2 - \kappa^2$ and Equation 2.36 can be re-written as

$$\frac{d^2R}{d\rho^2} + \frac{1}{\rho}\frac{dR}{d\rho} - \left(\beta^2 + n^2/\rho^2\right) \tag{3.85}$$

The solutions of this equation are

$$R(\rho) = \left\{ \begin{pmatrix} J_n(\jmath\beta\rho) \\ Y_n(\jmath\beta\rho) \end{pmatrix} \right. \tag{3.86}$$

Bessel functions with complex arguments are usually re-defined as [25]

$$I_n(x) = (\jmath)^{-n} J_n(\jmath x) \tag{3.87}$$

$$K_n(x) = \frac{\pi}{2}(\jmath)^{n+1} H_n^{(1)}(\jmath x) \tag{3.88}$$

This change in the definition of $R(\rho)$ will introduce discontinuities into the determinant and can result in incorrect roots found by the root finding algorithm. This fact has to be kept in mind when the roots of the determinant are solved in order to eliminate some of the additional roots.

### Solving for the Inner Products

Using Equation 3.54, the inner products can be derived. In order to obtain equations for the inner products that could easily be applied to different types of layered structures, it was decided to also divide region B into two parts and model it as a two-layer stratified waveguide (for a structure that has an air-filled region B, one then simply assumes the same permittivity in both regions, and the two-layer stratified fields simplify to those of the annular air-filled cylindrical waveguide as described above). This means that in the following inner product equations, there will now also be two axial propagation constants, $\zeta_{Bj,1}$ and $\zeta_{Bj,2}$ which are respectively defined for each part. The height of the fictional two-layer stratified waveguide in region B is $l2$ with the condition that $l1 < l2 < L/2$. In order to avoid confusion, the following relationships are

summarized:

$$\kappa_{Ai,1}^2 = \kappa_0^2 \epsilon_{Ai,r1} \tag{3.89}$$

$$\kappa_{Ai,2}^2 = \kappa_0^2 \epsilon_{Ai,r2} \tag{3.90}$$

$$\kappa_{Bj,1}^2 = \kappa_0^2 \epsilon_{Bj,r1}$$

$$\kappa_{Bj,2}^2 = \kappa_0^2 \epsilon_{Bj,r2}$$

$$\gamma_{Ai,1}^2 = \beta_{Ai}^2 - \kappa_{Ai,1}^2$$

$$\gamma_{Ai,2}^2 = \beta_{Ai}^2 - \kappa_{Ai,2}^2$$

$$\zeta_{Bj,1}^2 = \beta_{Bj}^2 - \kappa_{Bj,1}^2$$

$$\zeta_{Bj,2}^2 = \beta_{Bj}^2 - \kappa_{Bj,2}^2$$

where $\kappa_0^2 = (2\pi f)^2 \mu_0 \epsilon_0$. The solution of the inner products for different combinations of TE or TM modes in regions A and B are now given.

### Inner Products (TE mode in region A, TE mode in region B)

The inner products are given by

$$\langle \hat{\mathrm{e}}_{Ai}, \hat{\mathrm{h}}_{Bj} \rangle = \frac{\beta_{Ai}}{\beta_{Ai}^2} \left( A_1 z_1 + A_2 + z_2 + A_3 z_3 \right) \tag{3.91}$$

and

$$\langle \hat{\mathrm{e}}_{Bj}, \hat{\mathrm{h}}_{Ai} \rangle = \frac{\beta_{Bj}}{\beta_{Bj}^2} \left( A_1 z_1 + A_2 + z_2 + A_3 z_3 \right) \tag{3.92}$$

where for a PEC wall at $z = 0$

$$A_1 = \frac{\sinh\left(\gamma_{Ai,2}(L - l1)/2\right)}{\sinh\left(\gamma_{Ai,1} l1/2\right)} \frac{\sinh\left(\zeta_{Bj,2}(L - l2)/2\right)}{\sinh\left(\zeta_{Bj,1} l2/2\right)} \tag{3.93}$$

$$A_2 = \frac{\sinh\left(\zeta_{Bj,2}(L - l2)/2\right)}{\sinh\left(\zeta_{Bj,1} l2/2\right)}$$

$$A_3 = 1$$

$$z_1 = \int_0^{l1} \sinh\left(\gamma_{Ai,1} z\right) \sinh\left(\zeta_{Bj,1} z\right) dz$$

$$z_2 = \int_{l1}^{l2} \sinh\left(\gamma_{Ai,2}(L/2 - z)\right) \sinh\left(\zeta_{Bj,1} z\right) dz$$

$$z_3 = \int_{l2}^{L/2} \sinh\left(\gamma_{Ai,2}(L/2 - z)\right) \sinh\left(\zeta_{Bj,2}(L/2 - z)\right) dz$$

and for a PMC wall at $z = 0$

$$\begin{aligned} A_1 &= \frac{\sinh(\gamma_{Ai,2}(L-l1)/2)}{\cosh(\gamma_{Ai,1}l1/2)} \frac{\sinh(\zeta_{Bj,2}(L-l2)/2)}{\cosh(\zeta_{Bj,1}l2/2)} \\ A_2 &= \frac{\sinh(\zeta_{Bj,2}(L-l2)/2)}{\cosh(\zeta_{Bj,1}l2/2)} \\ A_3 &= 1 \\ z_1 &= \int_0^{l1} \cosh(\gamma_{Ai,1}z)\cosh(\zeta_{Bj,1}z)dz \\ z_2 &= \int_{l1}^{l2} \sinh(\gamma_{Ai,2}(L/2-z))\cosh(\zeta_{Bj,1}z)dz \\ z_3 &= \int_{l2}^{L/2} \sinh(\gamma_{Ai,2}(L/2-z))\sinh(\zeta_{Bj,2}(L/2-z))dz \end{aligned} \tag{3.94}$$

**Inner Products (TM mode in region A, TM mode in region B)**

Here the inner products are

$$\langle \hat{\mathrm{e}}_{Ai}, \hat{\mathrm{h}}_{Bj} \rangle = -\frac{\beta_{Bj}}{\beta_{Bj}^2}(A_1 z_1 + A_2 z_2 + A_3 z_3) \tag{3.95}$$

and

$$\langle \hat{\mathrm{e}}_{Bj}, \hat{\mathrm{h}}_{Ai} \rangle = -\frac{\beta_{Ai}}{\beta_{Ai}^2}(A_4 z_1 + A_5 z_2 + A_6 z_3) \tag{3.96}$$

where for a PEC wall at $z = 0$

$$\begin{aligned} A_1 &= \frac{\cosh(\gamma_{Ai,2}(L-l1)/2)}{\kappa_{Ai,1}^2\cosh(\gamma_{Ai,1}l1/2)} \frac{\cosh(\zeta_{Bj,2}(L-l2)/2)}{\cosh(\zeta_{Bj,1}l2/2)} \\ A_2 &= \frac{\cosh(\zeta_{Bj,2}(L-l2)/2)}{\kappa_{Ai,2}^2\cosh(\zeta_{Bj,1}l2/2)} \\ A_3 &= \frac{1}{\kappa_{Ai,2}^2} \\ A_4 &= \frac{\cosh(\gamma_{Ai,2}(L-l1)/2)}{\cosh(\gamma_{Ai,1}l1/2)} \frac{\cosh(\zeta_{Bj,2}(L-l2)/2)}{\kappa_{Bj,1}^2\cosh(\zeta_{Bj,1}l2/2)} \\ A_5 &= \frac{\cosh(\zeta_{Bj,1}(L-l2)/2)}{\kappa_{Bj,2}^2\cosh(\zeta_{Bj,1}l2/2)} \\ A_6 &= \frac{1}{\kappa_{Bj,2}^2} \end{aligned} \tag{3.97, 3.98}$$

and

$$\begin{aligned} z_1 &= \int_0^{l1} \cosh(\gamma_{Ai,1}z)\cosh(\zeta_{Bj,1}z)dz \\ z_2 &= \int_{l1}^{l2} \cosh(\gamma_{Ai,2}(L/2-z))\cosh(\zeta_{Bj,1}z)dz \\ z_3 &= \int_{l2}^{L/2} \cosh(\gamma_{Ai,2}(L/2-z))\cosh(\zeta_{Bj,2}(L/2-z))dz \end{aligned} \tag{3.99}$$

while for a PMC wall at $z = 0$

$$\begin{aligned} A_1 &= \frac{\cosh(\gamma_{Ai,2}(L-l1)/2)}{\kappa_{Ai,1}^2 \sinh(\gamma_{Ai,1} l1/2)} \frac{\cosh(\zeta_{Bj,2}(L-l2)/2)}{\sinh(\zeta_{Bj,1} l2/2)} \\ A_2 &= \frac{\cosh(\zeta_{Bj,2}(L-l2)/2)}{\kappa_{Ai,2}^2 \sinh(\zeta_{Bj,1} l2/2)} \\ A_3 &= \frac{1}{\kappa_{Ai,2}^2} \\ A_4 &= \frac{\cosh(\gamma_{Ai,2}(L-l1)/2)}{\sinh(\gamma_{Ai,1} l1/2)} \frac{\cosh(\zeta_{Bj,2}(L-l2)/2)}{\kappa_{Bj,1}^2 \sinh(\zeta_{Bj,1} l2/2)} \\ A_5 &= \frac{\cosh(\zeta_{Bj,1}(L-l2)/2)}{\kappa_{Bj,2}^2 \sinh(\zeta_{Bj,1} l2/2)} \\ A_6 &= \frac{1}{\kappa_{Bj,2}^2} \end{aligned} \tag{3.100, 3.101}$$

and

$$\begin{aligned} z_1 &= \int_0^{l1} \sinh(\gamma_{Ai,1} z) \sinh(\zeta_{Bj,1} z) dz \\ z_2 &= \int_{l1}^{l2} \cosh(\gamma_{Ai,2}(L/2 - z)) \sinh(\zeta_{Bj,1} z) dz \\ z_3 &= \int_{l2}^{L/2} \cosh(\gamma_{Ai,2}(L/2 - z)) \cosh(\zeta_{Bj,2}(L/2 - z)) dz \end{aligned} \tag{3.102}$$

**Inner Products (TE mode in region A, TM mode in region B)**

We find that

$$\langle \hat{\mathrm{e}}_{Ai}, \hat{\mathrm{h}}_{Bj} \rangle = 0 \tag{3.103}$$

and

$$\langle \hat{\mathrm{e}}_{Bj}, \hat{\mathrm{h}}_{Ai} \rangle = \frac{n}{\rho \beta_{Bj}^2} (A_1 z_1 + A_2 z_2 - A_3 z_3) + \frac{n}{\rho \beta_{Ai}^2} (A_4 z_4 - A_5 z_5 - A_6 z_6) \tag{3.104}$$

where for a PEC wall at $z = 0$

$$\begin{aligned} A_1 &= \frac{\zeta_{Bj,1}}{\kappa_{Bj,1}^2} \frac{\sinh(\gamma_{Ai,2}(L-l1)/2)}{\sinh(\gamma_{Ai,1} l1/2)} \frac{\cosh(\zeta_{Bj,2}(L-l2)/2)}{\cosh(\zeta_{Bj,1} l2/2)} \\ A_2 &= \frac{\zeta_{Bj,1}}{\kappa_{Bj,1}} \frac{\cosh(\zeta_{Bj,2}(L-l2)/2)}{\cosh(\zeta_{Bj,1} l2/2)} \\ A_3 &= \frac{\zeta_{Bj,2}}{\kappa_{Bj,2}^2} \\ A_4 &= \frac{\gamma_{Ai,1}}{\kappa_{Bj,1}^2} \frac{\sinh(\gamma_{Ai,2}(L-l1)/2)}{\sinh(\gamma_{Ai,1} l1/2)} \frac{\cosh(\zeta_{Bj,2}(L-l2)/2)}{\cosh(\zeta_{Bj,1} l2/2)} \\ A_5 &= \frac{\gamma_{Ai,2}}{\kappa_{Bj,1}^2} \frac{\cosh(\zeta_{Bj,2}(L-l2)/2)}{\cosh(\zeta_{Bj,1} l2/2)} \\ A_6 &= \frac{\gamma_{Ai,2}}{\kappa_{Bj,2}^2} \end{aligned} \tag{3.105}$$

and

$$
\begin{aligned}
z_1 &= \int_0^{l1} \sinh(\gamma_{Ai,1} z) \sinh(\zeta_{Bj,1} z) dz \\
z_2 &= \int_{l1}^{l2} \sinh(\gamma_{Ai,2}(L/2 - z)) \sinh(\zeta_{Bj,1} z) dz \\
z_3 &= \int_{l2}^{L/2} \sinh(\gamma_{Ai,2}(L/2 - z)) \sinh(\zeta_{Bj,2}(L/2 - z)) dz \\
z_4 &= \int_0^{l1} \cosh(\gamma_{Ai,1} z) \cosh(\zeta_{Bj,1} z) dz \\
z_5 &= \int_{l1}^{l2} \cosh(\gamma_{Ai,2}(L/2 - z)) \cosh(\zeta_{Bj,1} z) dz \\
z_6 &= \int_{l2}^{L/2} \cosh(\gamma_{Ai,2}(L/2 - z)) \cosh(\zeta_{Bj,2}(L/2 - z)) dz
\end{aligned}
\tag{3.106}
$$

and for a PMC wall at $z = 0$

$$
\begin{aligned}
A_1 &= \frac{\zeta_{Bj,1}}{\kappa^2_{Bj,1}} \frac{\sinh(\gamma_{Ai,2}(L - l1)/2)}{\cosh(\gamma_{Ai,1} l1/2)} \frac{\cosh(\zeta_{Bj,2}(L - l2)/2)}{\sinh(\zeta_{Bj,1} l2/2)} \\
A_2 &= \frac{\zeta_{Bj,1}}{\kappa^2_{Bj,1}} \frac{\cosh(\zeta_{Bj,2}(L - l2)/2)}{\sinh(\zeta Bj, 1 l2/2)} \\
A_3 &= \frac{\zeta_{Bj,2}}{\kappa^2_{Bj,2}} \\
A_4 &= \frac{\gamma_{Ai,1}}{\kappa^2_{Bj,1}} \frac{\sinh(\gamma_{Ai,2}(L - l1)/2)}{\cosh(\gamma_{Ai,1} l1/2)} \frac{\cosh(\zeta_{Bj,2}(L - z)/2)}{\sinh(\zeta_{Bj,1} l2/2)} \\
A_5 &= \frac{\gamma_{Ai,2}}{\kappa^2_{Bj,1}} \frac{\cosh(\zeta_{Bj,2}(L - l2)/2)}{\sinh(\zeta_{Bj,1} l2/2)} \\
A_6 &= \frac{\gamma_{Ai,2}}{\kappa^2_{Bj,2}}
\end{aligned}
\tag{3.107}
$$

and

$$
\begin{aligned}
z_1 &= \int_0^{l1} \cosh(\gamma_{Ai,1} z) \cosh(\zeta_{Bj,1} z) dz \\
z_2 &= \int_{l1}^{l2} \sinh(\gamma_{Ai,2}(L/2 - z)) \cosh(\zeta_{Bj,1} z) dz \\
z_3 &= \int_{l2}^{L/2} \sinh(\gamma_{Ai,2}(L/2 - z)) \sinh(\zeta_{Bj,2}(L/2 - z)) dz \\
z_4 &= \int_0^{l1} \sinh(\gamma_{Ai,1} z) \sinh(\zeta_{Bj,1} z) dz \\
z_5 &= \int_{l1}^{l2} \cosh(\gamma_{Ai,2}(L/2 - z)) \sinh(\zeta_{Bj,1} z) dz \\
z_6 &= \int_{l2}^{L/2} \cosh(\gamma_{Ai,2}(L/2 - z)) \cosh(\zeta_{Bj,2}(L/2 - z)) dz
\end{aligned}
\tag{3.108}
$$

**Inner Products (TM mode in region A, TE mode in region B)**

Here it is true that

$$\langle \hat{\mathrm{e}}_{Ai}, \hat{\mathrm{h}}_{Bj} \rangle = \frac{n}{\rho\beta_{Ai}^2}\left(A_1 z_1 - A_2 z_2 - A_3 z_3\right) + \frac{n}{\rho\beta_{Ai}^2}\left(A_4 z_4 + A_5 z_5 - A_6 z_6\right) \tag{3.109}$$

and

$$\langle \hat{\mathrm{e}}_{Bj}, \hat{\mathrm{h}}_{Ai} \rangle = 0 \tag{3.110}$$

where for a PEC wall at $z = 0$

$$A_1 = \frac{\gamma_{Ai,1}}{\kappa_{Ai,1}^2} \frac{\cosh\left(\gamma_{Ai,2}(L - l1)/2\right)}{\cosh\left(\gamma_{Ai,1} l1/2\right)} \frac{\sinh\left(\zeta_{Bj,2}(L - l2)/2\right)}{\sinh\left(\zeta_{Bj,1} l2/2\right)} \tag{3.111}$$

$$A_2 = \frac{\gamma_{Ai,2}}{\kappa_{Ai,2}^2} \frac{\sinh\left(\zeta_{Bj,2}(L - l2)/2\right)}{\sinh\left(\zeta_{Bj,1} l2/2\right)} \tag{3.112}$$

$$A_3 = \frac{\gamma_{Ai,2}}{\kappa_{Ai,2}^2}$$

$$A_4 = \frac{\zeta_{Bj,1}}{\kappa_{Ai,1}^2} \frac{\cosh\left(\gamma_{Ai,2}(L - l1)/2\right)}{\cosh\left(\gamma_{Ai,1} l1/2\right)} \frac{\sinh\left(\zeta_{Bj,2}(L - l2)/2\right)}{\sinh\left(\zeta_{Bj,1} l2/2\right)}$$

$$A_5 = \frac{\zeta_{Bj,1}}{\kappa_{Ai,2}^2} \frac{\sinh\left(\zeta_{Bj,2}(L - l2)/2\right)}{\sinh\left(\zeta_{Bj,1} l2/2\right)} \tag{3.113}$$

$$A_6 = \frac{\zeta_{Bj,2}}{\kappa_{Ai,2}^2}$$

and

$$z_1 = \int_0^{l1} \sinh\left(\gamma_{Ai,1} z\right) \sinh\left(\zeta_{Bj,1} z\right) dz \tag{3.114}$$

$$z_2 = \int_{l1}^{l2} \sinh\left(\gamma_{Ai,2}(L/2 - z)\right) \sinh\left(\zeta_{Bj,1} z\right) dz$$

$$z_3 = \int_{l2}^{L/2} \sinh\left(\gamma_{Ai,2}(L/2 - z)\right) \sinh\left(\zeta_{Bj,2}(L/2 - z)\right) dz$$

$$z_4 = \int_0^{l1} \cosh\left(\gamma_{Ai,1} z\right) \cosh\left(\zeta_{Bj,1} z\right) dz$$

$$z_5 = \int_{l1}^{l2} \cosh\left(\gamma_{Ai,2}(L/2 - z)\right) \cosh\left(\zeta_{Bj,1} z\right) dz$$

$$z_6 = \int_{l2}^{L/2} \cosh\left(\gamma_{Ai,2}(L/2 - z)\right) \cosh\left(\zeta_{Bj,2}(L/2 - z)\right) dz$$

and for a PMC wall at $z = 0$

$$A_1 = \frac{\gamma_{Ai,1}}{\kappa^2_{Ai,1}} \frac{\cosh(\gamma_{Ai,2}(L-l1)/2)}{\sinh(\gamma_{Ai,1}l1/2)} \frac{\sinh(\zeta_{Bj,2}(L-l2)/2)}{\cosh(\zeta_{Bj,1}l2/2)} \tag{3.115}$$

$$A_2 = \frac{\gamma_{Ai,2}}{\kappa^2_{Ai,2}} \frac{\sinh(\zeta_{Bj,2}(L-l2)/2)}{\cosh(\zeta_{Bj,1}l2/2)} \tag{3.116}$$

$$A_3 = \frac{\gamma_{Ai,2}}{\kappa^2_{Ai,2}}$$

$$A_4 = \frac{\zeta_{Bj,1}}{\kappa^2_{Ai,1}} \frac{\cosh(\gamma_{Ai,2}(L-l1)/2)}{\sinh(\gamma_{Ai,1}l1/2)} \frac{\sinh(\zeta_{Bj,2}(L-l2)/2)}{\cosh(\zeta_{Bj,1}l2/2)}$$

$$A_5 = \frac{\zeta_{Bj,1}}{\kappa^2_{Ai,2}} \frac{\sinh(\zeta_{Bj,2}(L-l2)/2)}{\cosh(\zeta_{Bj,1}l2/2)} \tag{3.117}$$

$$A_6 = \frac{\zeta_{Bj,2}}{\kappa^2_{Ai,2}}$$

and

$$z_1 = \int_0^{l1} \cosh(\gamma_{Ai,1}z)\cosh(\zeta_{Bj,1}z)dz \tag{3.118}$$

$$z_2 = \int_{l1}^{l2} \sinh(\gamma_{Ai,2}(L/2-z))\cosh(\zeta_{Bj,1}z)dz$$

$$z_3 = \int_{l2}^{L/2} \sinh(\gamma_{Ai,2}(L/2-z))\sinh(\zeta_{Bj,2}(L/2-z))dz$$

$$z_4 = \int_0^{l1} \sinh(\gamma_{Ai,1}z)\sinh(\zeta_{Bj,1}z)dz$$

$$z_5 = \int_{l1}^{l2} \cosh(\gamma_{Ai,2}(L/2-z))\sinh(\zeta_{Bj,1}z)dz$$

$$z_6 = \int_{l2}^{L/2} \cosh(\gamma_{Ai,2}(L/2-z))\cosh(\zeta_{Bj,2}(L/2-z))dz$$

The solutions of the integrations of products of hyperbolic sinusoids as founds in functions $z_1 \ldots z_6$ in the inner product equations are provided in Appendix C.

### Solving for the Resonant Frequencies

The first step in the implementation is to solve for N axial propagation constants $\gamma_i$ of the waveguide modes that exist in region A as well as N axial propagation constants $\zeta_j$ for the fields in region B by finding the roots of the respective characteristic equation. The root finding algorithm used, was largely based on the work done by Lehmensiek [18]. These propagation constants are then used to calculate the inner products when matching the modes at the boundary (each mode in region A is matched with all modes in region B and vice versa). The propagation constants are always taken consecutively from the first solved propagation constant, numbered $\gamma_1$. Omitting a propagation constant can have serious consequences on the obtained inner product matrix. Therefore it is very important to test that the root finding algorithm used to search for the

propagation constants is accurate. In order to find the determinant of matrix $\overline{X}$, it must be square. This means that one must take equal numbers of modes in both regions. Therefore, if one wants to solve for TE modes, $N \times TE$ modes in region A are matched with $N \times TE$ modes in region B at the boundary $\rho = a$ resulting in a matrix that has dimensions of $N \times N$ and if one wants to solve for TM modes, $N \times TM$ modes in region A are matched with $N \times TM$ modes in region B at the boundary. For hybrid modes equal numbers of TE and TM modes must be matched. Therefore one can choose to match $N \times TE$ modes and $N \times TM$ modes in regions A and B with each other again resulting in a matrix with dimensions of $2N \times 2N$. Note that the number N can be chosen to be an arbitrary real integer. It represents the amount of TE and/or TM modes from each region that are matched at the boundary.

Now it is possible to solve for the resonant frequencies by setting up matrix $X_{ij}$ in Equation 3.58. As the number of modes used in each regions increases, so does the accuracy of the obtained results. The usual approach is to start with a small matrix size and find the zero points of the determinant of $\overline{X}$. These zero points correspond to rough estimates of the resonant frequency of the dielectric resonator. Each successive increase in matrix size leads the zero points to converge towards the actual resonant frequency. After increasing the matrix beyond a certain size, any further increases will have very little effect on the derived zero point. Therefore, one can assume that the answer has converged to very close to the resonant frequency of the dielectric resonator and one can take it as the final answer. Different modes converge towards the actual resonant frequency at different rates. This convergence is one of the aspects that are considered when the mode matching technique is investigated with respect to efficiency.

Before the results of the implemented mode matching technique are discussed in more detail it is necessary to define the way in which the individual modes are labelled. There is no standard method used to label a specific dielectric resonator waveguide mode and several different methods can be found in literature. Since most of the fundamental work of this report is based on work done by Chen [9], his mode-labelling method is adopted.

Therefore each mode is described by three letters followed by a subscript of two numbers. The first two letters are either TE (for TE modes), TM (for TM modes) or HE (for hybrid modes). The third letter is either E (E-plane) or H (H-plane). This refers to the type of symmetry conditions that are applied at the longitudinal axis of symmetry (z=0) for a cylindrical structure such as that shown in Figure 3.1. The first subscript refers to the number of angular variations, $n$, and the second subscript, $m$. is the order in which the mode occurs with respect to frequency, where $m = 1$ designates the first resonant frequency of that particular mode. One disadvantage of this mode designation is that it does not give an idea of the radial ($\rho$) or the axial ($z$) distributions of the fields in the resonator. This means that the $TEH_{01}$ mode is a TE mode with a magnetic wall at $z = 0$. It has no angular variation and is the first such mode to occur. In other words it has the lowest resonant frequency of all $TEH_{0m}$ modes. It can be proved [32] that the modes that exist in a dielectric loaded waveguide resonator can be $TEE_{0m}$, $TEH_{0m}$ $TME_{0m}$, $TMH_{0m}$, $HEE_{nm}$ or $HEH_{nm}$ modes.

Now that the theory of radial mode matching has been discussed, several results obtained by the implemented radial mode matching method are presented. The method is discussed with respect to convergence and accuracy.

### Implementation of Two-layer Radial Mode Matching

The results of the implementation are compared to the resonant frequencies derived by Zaki and Chen [32]. The mode chart from this article, gives computed and measured resonant frequencies for a dielectric resonator with relative permittivity of $\epsilon_r = 35.74$, that has a height of $l = 7.62$ mm (0.3 in), a radius of $a = 8.636$ mm (0.34 in.) which is placed centrally inside the cylindrical cavity. The resonator is surrounded by a metallic shield with a radius of $b = 14.48$ mm (0.57 in.) and a variable height, $L$. The chart then plots the measured and derived changes of the resonant frequency of several modes as a function of $L/l$. In the implementation discussed in this report, $L$ was chosen to be 35.56 mm (1.41 in). The results obtained by Chen were compared to measured results that were stated to be within $\pm 0.5\%$ of the calculated results with the exception of $HEH_{12}$ (the chart showing measured points as compared to the computed points shows a difference of approximately 0.1 GHz).

As stated previously, the accuracy of the calculated resonant frequency increases as the size of matrix $X_{ij}$ in Equation 3.58 increases. The convergence can be investigated by increasing the size of matrix $X_{ij}$ in steps, and determining the size that the matrix has to reach before the frequency is accurate with respect to a certain tolerance set by the user. The convergence of several modes is plotted in Figure 3.4 - 3.5, where Figure 3.4 shows the calculated convergence of the TE and TM modes for a simple post resonator and Figure 3.5 shows the convergence of the hybrid modes. It can be seen that the TE and TM modes have largely converged for $N > 2$ while for the hybrid modes $N > 4$. Take note that $N = N_j = N_i$ represents the number of modes in each region. Therefore if N=2 for a TE mode implementation, 2 TE modes in region A are matched with 2 TE modes in region B, or for a TM mode implementation, 2 TM modes in region A are matched with 2 TM modes in region B. For hybrid modes, N = 2 means that 2 TE modes and 2 TM modes in each region are matched with the modes in the other region. Therefore the ratio of modes needed for convergence of non-hybrid to hybrid modes is 1:4.

The values derived from the implementation are compared to those read off Chen's chart in Table 3.1. As can be seen the greatest discrepancy is for the $HEH_{12}$ hybrid mode. Chen states that the derived resonant frequency of this mode is less accurate than the other modes. In the chart, there seems to be a difference of about 0.1 GHz between the measured and the computed value. Therefore the 3.25 % error between the value derived by the implementation and the value derived by Chen might not be as great when the implementation is compared to the true measured frequency. For all the values stated in the above discussion the possibility of inaccurate plotting on the chart and errors reading the values off the chart must be kept in mind.

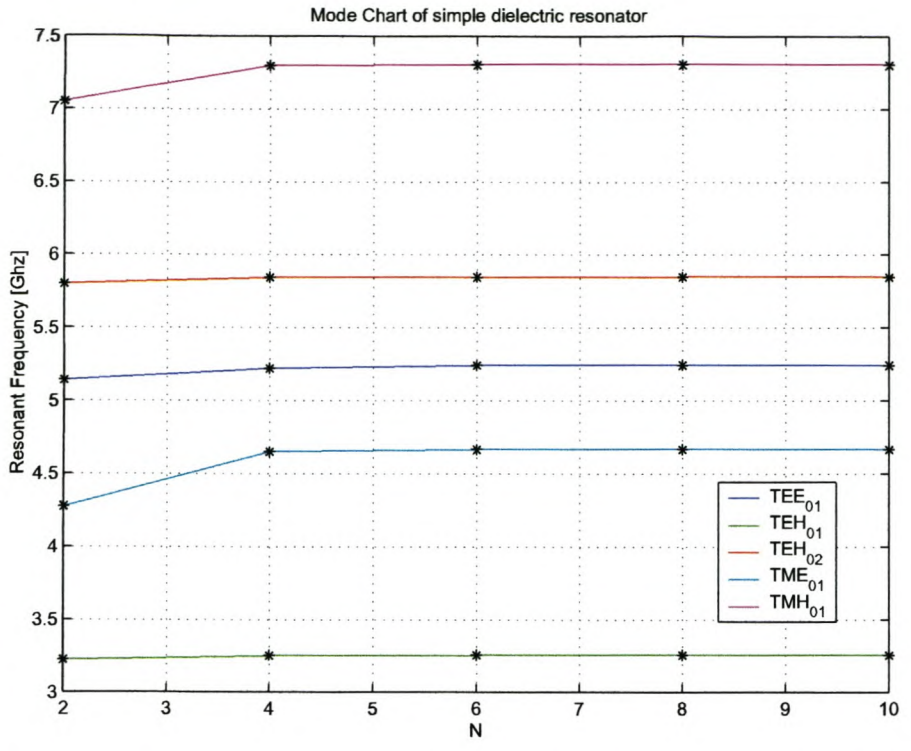


**Figure 3.4:** *Calculated Convergence of the $TE_{0m}$ and $TM_{0m}$ modes for the post resonator*

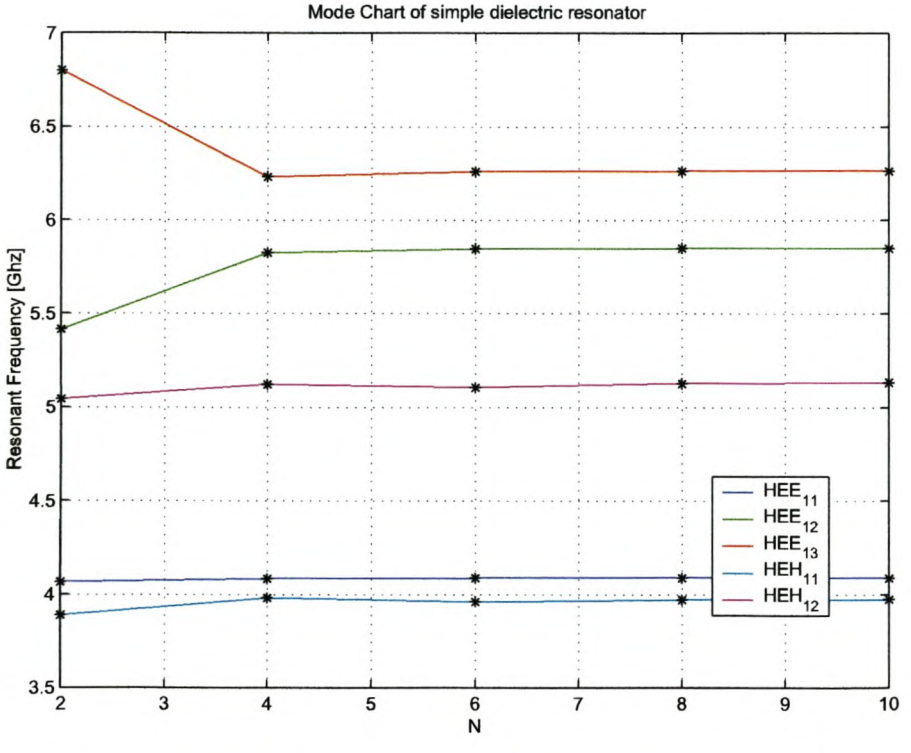


**Figure 3.5:** *Calculated Convergence of the $HE_{nm}$ modes for the post resonator*

**Table 3.1:** *Comparison of Resonant Frequencies derived by the Implementation and those derived by Chen [32] for the post resonator showing the percentage error*

| Mode | Implementation [GHz] | Chen's [GHz] | Percent % |
|---|---|---|---|
| $TEE_{01}$ | 5.2431 | 5.3 | 1.07 |
| $TEH_{02}$ | 3.2556 | 3.3 | 1.35 |
| $TME_{01}$ | 4.6669 | 4.65 | 0.36 |
| $TMH_{01}$ | 7.303 | 7.3 | 0.41 |
| $TEH_{02}$ | 5.8470 | 5.9 | 0.89 |
| $HEE_{11}$ | 4.0868 | 4.15 | 1.52 |
| $HEE_{12}$ | 5.8501 | 5.85 | 1.7 |
| $HEE_{13}$ | 6.2623 | 6.3 | 0.7 |
| $HEH_{11}$ | 3.9730 | 3.98 | 0.18 |
| $HEH_{12}$ | 5.1275 | 5.3 | 3.25 |

In order to more precisely investigate the accuracy of the hybrid modes derived by the implementation, the resonant frequencies provided by [9] were derived and compared in Table 3.2. It can be seen that the accuracy is better than 0.6 percent. Additionally, when using the inner products derived by [9] to implement the radial mode matching technique, the obtained resonant frequencies are also the same as those of the implementation using the inner products stated in this report.

**Table 3.2:** *Comparison of Hybrid Mode Resonant Frequencies for the post resonator [GHz]. The matrix size, N=10*

| Mode | Chen's | Implementation | Percent % |
|---|---|---|---|
| $HEH_{01}$ | 4.147 | 4.1445 | 0.6 |
| $HEH_{21}$ | 5.150 | 5.1474 | 0.5 |

Another aspect that was investigated was the effect of changing the height ratio of the dielectric resonator and the metallic waveguide. The resultant graphs are shown in Figures 3.6, 3.7 and 3.8. The stars (*) show the actual values derived from the radial mode matching implementation, and the circles show the points read off the mode chart provided by Chen [32]. The obtained results are very accurate for TE and TM modes, with slight discrepancies for the hybrid modes. Once again, this could be as a result of inaccurate reading off the chart.

At this point radial mode matching has only been discussed as applied to a simple dielectric resonator with a single radial boundary. The next subsection discusses the expansion of this method to structures with multiple boundaries. This is necessary if one wants to obtain an idea of the resonant modes of the layered structure that was proposed in Chapter 1.

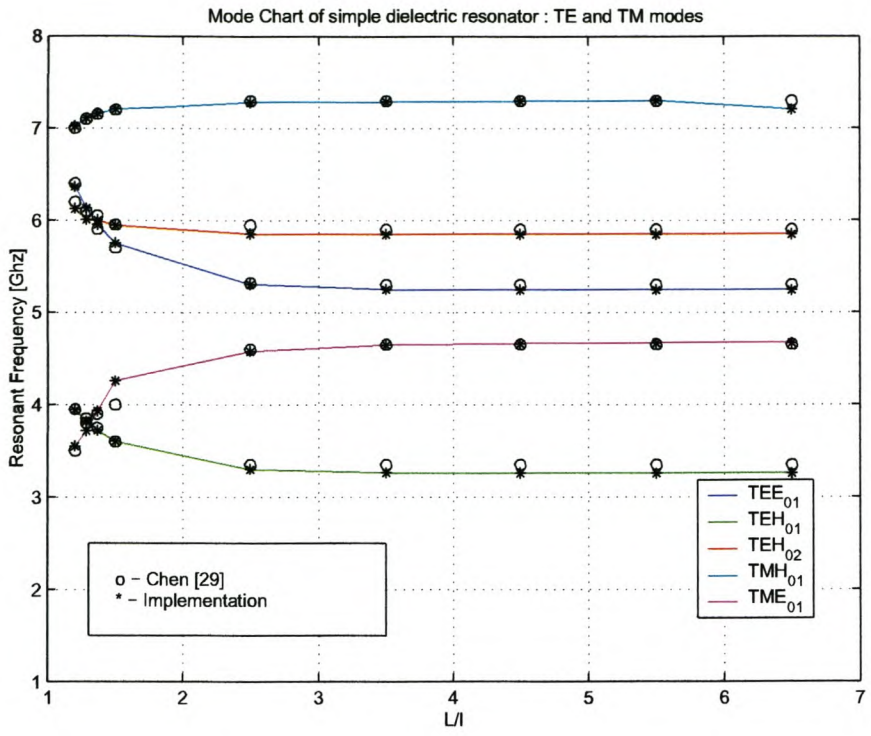


**Figure 3.6:** *Effect of changing the $L/l$ ratio on the $TE_{0m}$ and $TM_{0m}$ modes for the post resonator*

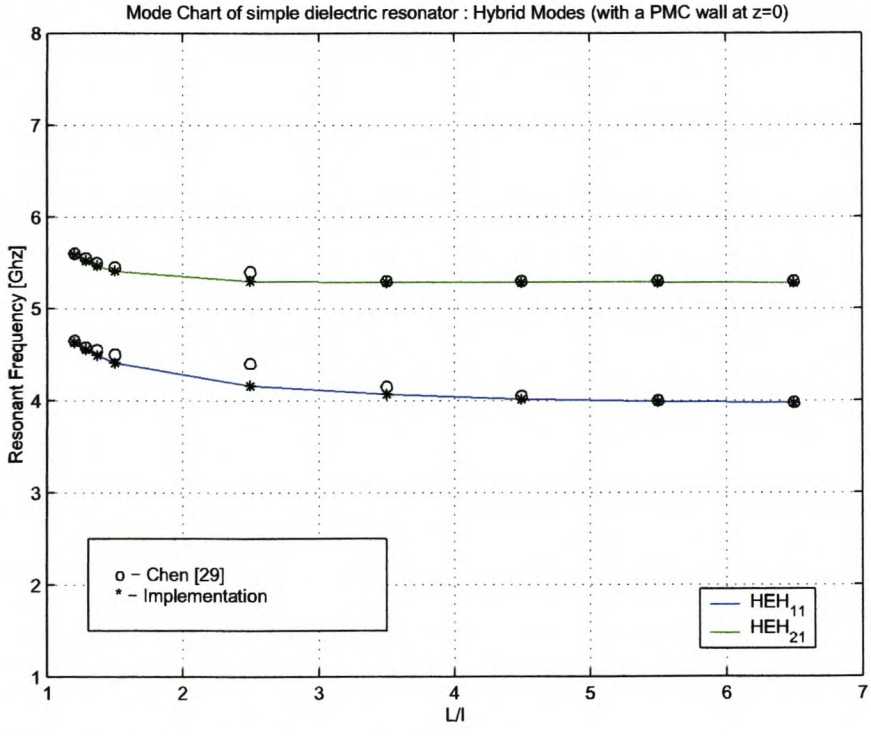


**Figure 3.7:** *Effect of changing the $L/l$ ratio on the $HEH_{nm}$ modes for the post resonator*

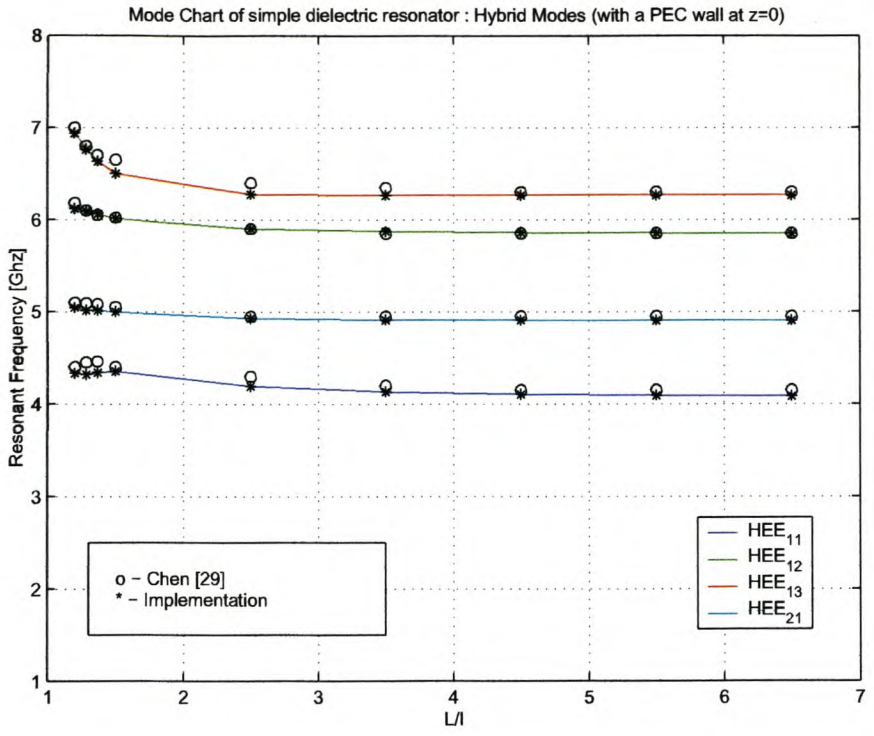


**Figure 3.8:** *Effect of changing the L/l ratio on thee $HEE_{nm}$ modes for the post resonator*

### 3.2.3 Multiple layered Structures

#### Ring Resonator

First, the method is applied to a dielectric ring resonator, as is shown in Figure 3.9 contained in a metallic air-filled cavity. This means that the fields have to be matched at two boundaries. In this derivation the resonator can once again be divided into symmetrical sections with either a PEC or PMC wall at $z = 0$. The resonator is divided into three regions : regions A,B and C.

Region A is the inner region within $0 \leq \rho = a$ and extending from $0 \leq z < L/2$. The electric and magnetic fields are given as

$$\begin{aligned} \overline{E}_A(\rho,\phi,z) &= \sum_i A_i \hat{\mathrm{e}}_{A_i}(z,\phi) f^e_{A_i}(\rho) \\ \overline{H}_A(\rho,\phi,z) &= \sum_i A_i \hat{\mathrm{h}}_{A_i}(z,\phi) f^h_{A_i}(\rho) \end{aligned} \tag{3.119}$$

The next region, Region B is bounded by $a \leq \rho < b$ and extends from $0 \leq z < L/2$. Since in regions B the field can be separated into the forward moving wave and the backward moving

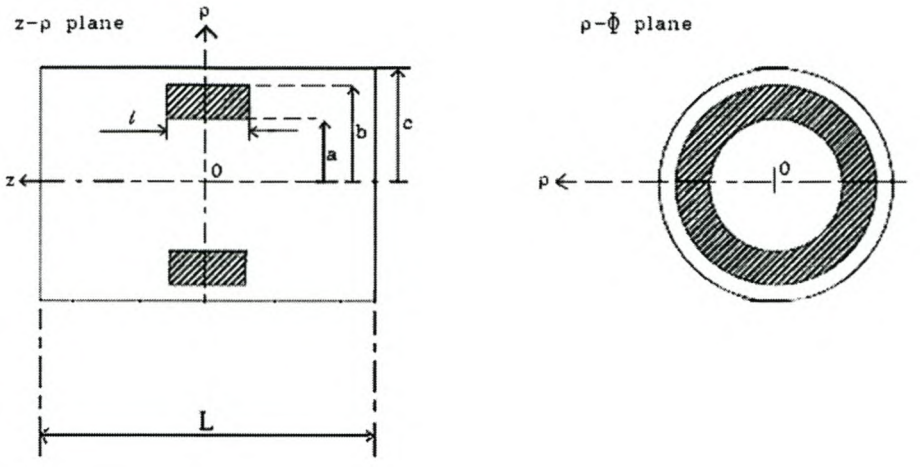


**Figure 3.9:** *A ring resonator enclosed by a metallic sheath*

wave, the fields in region B can be written as

$$\begin{aligned} \overline{E}_B(\rho,\phi,z) &= \sum_j \hat{\mathrm{e}}_{B_j}(z,\phi)\left[B_j^+ f^e_{B_j^+}(\rho) + B_j^- f^e_{B_j^-}(\rho)\right] \\ \overline{H}_B(\rho,\phi,z) &= \sum_j \hat{\mathrm{h}}_{B_j}(z,\phi)\left[B_j^+ f^h_{Bj^+}(\rho) + B_j^- f^h_{B_j^-}(\rho)\right] \end{aligned} \tag{3.120}$$

and finally, Region C is contained within $b \leq \rho \leq c$ and extends from $0 \leq z < L/2$ and has fields such that

$$\begin{aligned} \overline{E}_C(\rho,\phi,z) &= \sum_k C_k \hat{\mathrm{e}}_{C_k}(z,\phi) f^e_{C_k}(\rho) \\ \overline{H}_C(\rho,\phi,z) &= \sum_k C_k \hat{\mathrm{h}}_{C_k}(z,\phi) f^h_{C_k}(\rho) \end{aligned} \tag{3.121}$$

The tangential fields must match at the two boundary at $\rho = a$ and $\rho = b$. Therefore

$$\overline{E}_A(\rho = a,\phi,z) = \overline{E}_B(\rho = a,\phi,z) \tag{3.122}$$

$$\overline{H}_A(\rho = a,\phi,z) = \overline{H}_B(\rho = a,\phi,z) \tag{3.123}$$

and

$$\overline{E}_B(\rho = b,\phi,z) = \overline{E}_C(\rho = b,\phi,z) \tag{3.124}$$

$$\overline{H}_B(\rho = b,\phi,z) = \overline{H}_C(\rho = b,\phi,z) \tag{3.125}$$

The cross product of Equation 3.122 with $\hat{\mathrm{h}}_{Ai}$ is taken and integrated over the interface, and similarly, the cross-product of Equation 3.123 is taken with $\hat{\mathrm{e}}_{Ai}$ and integrated over the interface

surface, S. We can now derive the following homogenous linear set of equations

$$\sum_j \left[ X_{ij}^+ B_j^+ + X_{ij}^- B_j^- \right] = 0 \tag{3.126}$$

where

$$X_{ij}^+ = \langle \hat{\mathrm{e}}_{B_j}, \hat{\mathrm{h}}_{A_i} \rangle f_{B_j^+}^e(a) f_{A_i}^h(a) - \langle \hat{\mathrm{e}}_{A_i}, \hat{\mathrm{h}}_{B_j} \rangle f_{B_j^+}^h(a) f_{A_i}^e(a) \tag{3.127}$$

and

$$X_{ij}^- = \langle \hat{\mathrm{e}}_{B_j}, \hat{\mathrm{h}}_{A_i} \rangle f_{B_j^-}^e(a) f_{A_i}^h(a) - \langle \hat{\mathrm{e}}_{A_i}, \hat{\mathrm{h}}_{B_j} \rangle f_{B_j^-}^h(a) f_{A_i}^e(a) \tag{3.128}$$

The same principal can be applied at the boundary $\rho = b$ and we can derive a set of linear equations which is given by

$$\sum_j \left[ Y_{ij}^+ B_j^+ + Y_{ij}^- B_j^- \right] = 0 \tag{3.129}$$

where

$$Y_{kj}^+ = \langle \hat{\mathrm{e}}_{B_j}, \hat{\mathrm{h}}_{C_k} \rangle f_{B_j^+}^e(b) f_{C_k}^h(b) - \langle \hat{\mathrm{e}}_{C_k}, \hat{\mathrm{h}}_{B_j} \rangle f_{B_j^+}^h(b) f_{C_k}^e(b) \tag{3.130}$$

and

$$Y_{kj}^- = \langle \hat{\mathrm{e}}_{B_j}, \hat{\mathrm{h}}_{C_k} \rangle f_{B_j^-}^e(b) f_{C_k}^h(b) - \langle \hat{\mathrm{e}}_{C_k}, \hat{\mathrm{h}}_{B_j} \rangle f_{B_j^-}^h(b) f_{C_k}^e(b) \tag{3.131}$$

The derived homogenous equations therefore be combined as a single matrix which is given by

$$\begin{bmatrix} X_{ij}^+ & X_{ij}^- \\ Y_{kj}^+ & X_{kj}^- \end{bmatrix} \begin{bmatrix} B^+ \\ B^- \end{bmatrix} = \overline{H} B = 0 \tag{3.132}$$

Again, the points where the determinant of $\overline{H}$ is zero, represent non-trivial solutions of the linear system. It is important to be very careful when substituting the TE and TM modes into matrix, $\overline{H}$, when implementing hybrid modes. The field in the individual regions can once again be modelled as cylindrical or two-layer stratified waveguides. The only difference occurs in region B where the radial dependency, $R(\beta_j \rho)$, does not have an external boundary, and can therefore not be simplified as was the case when radial mode matching was applied to a simple dielectric resonator. Therefore, in this region we simply take the radial dependency as

$$\begin{aligned} R(\beta_j \rho) &= E f(\rho)^+ + F\ f(\rho)^- \\ &= E\ J_n(\beta_j \rho) + F\ Y_n(\beta_j \rho) \end{aligned} \tag{3.133}$$

where $J_n(\beta_j \rho)$ is the radial dependency of the forward travelling wave and $Y_n(\beta_j \rho)$ is the radial dependency of the backwards travelling wave. The electric and magnetic fields for the various modes can be solved for as before.

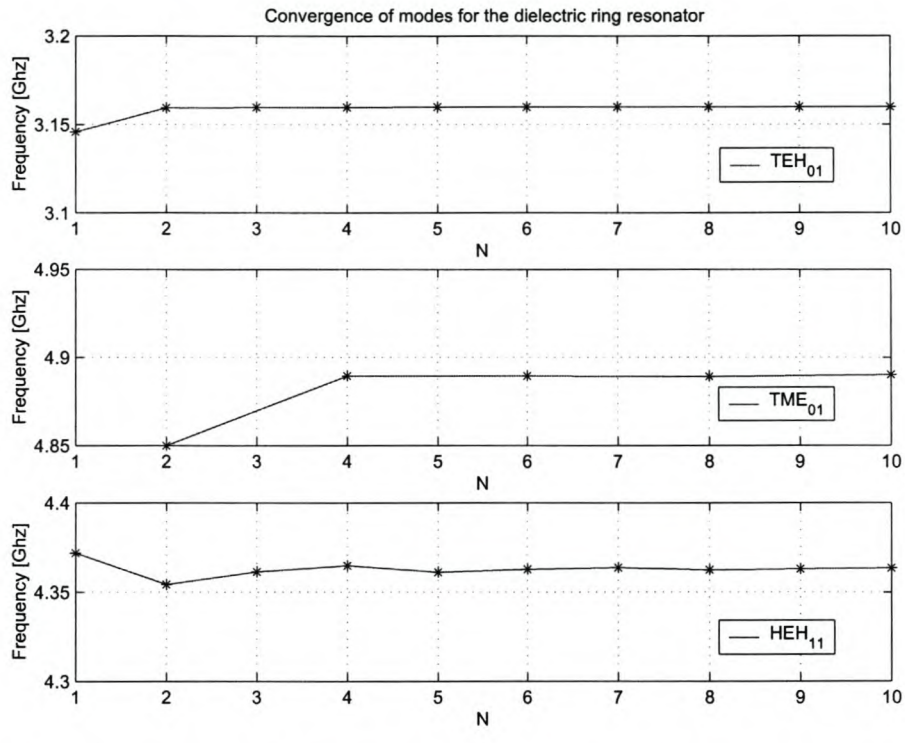


**Figure 3.10:** *The convergence of several mode of the dielectric ring resonator. The dimensions of the resonator are a = 2.54 mm, b = 10.16 mm, c = 15.24 mm, l = 6.35 mm and L = 19.05 mm*

### Implementation of Three-layer Radial Mode Matching

The three-layer radial mode matching technique is tested with regard to accuracy and convergence. Figure 3.10 shows the convergence of the $TEH_{01}$, the $TME_{01}$ and the $HEH_{11}$ mode. The derived resonant frequencies are compared with those derived by Chen [9] in Table 3.3. Once again the values are accurate. Take note that as defined previously, the N for the hybrid modes means that NxTE and NxTM modes are matched at the boundary. Therefore for the same N, the number of modes is double for hybrid modes than for the TE or TM modes.

**Table 3.3:** *Comparison of Resonant Frequencies derived by the Implementation and those derived by Chen [9] for the ring resonator showing the percentage error [N = 10]*

| Mode | Implementation [GHz] | Chen's [GHz] | Percent % |
|---|---|---|---|
| $TEH_{01}$ | 3.1614 | 3.165 | 0.11 |
| $TME_{02}$ | 4.8893 | 4.895 | 0.4 |
| $HEH_{11}$ | 4.3635 | 4.365 | 0.34 |

**Four-layer Mode Matching Implementation**

For a structure with three radial boundaries at $\rho = a$, $\rho = b$ and $\rho = c$ , the same method is applied. Now there are four regions and the fields in them are defined as before. In region A

$$\begin{aligned} \overline{E}_A(\rho,\phi,z) &= \sum_i A_i \hat{\mathrm{e}}_{A_i}(z,\phi) f^e_{A_i}(\rho) \\ \overline{H}_A(\rho,\phi,z) &= \sum_i A_i \hat{\mathrm{h}}_{A_i}(z,\phi) f^h_{A_i}(\rho) \end{aligned} \tag{3.134}$$

in region B

$$\begin{aligned} \overline{E}_B(\rho,\phi,z) &= \sum_j \hat{\mathrm{e}}_{B_j}(z,\phi) \left[ B^+_j f^e_{B^+_j}(\rho) + B^-_j f^e_{B^-_j}(\rho) \right] \\ \overline{H}_B(\rho,\phi,z) &= \sum_j \hat{\mathrm{h}}_{B_j}(z,\phi) \left[ B^+_j f^h_{B^+_j}(\rho) + B^-_j f^h_{B^-_j}(\rho) \right] \end{aligned} \tag{3.135}$$

in region C

$$\begin{aligned} \overline{E}_C(\rho,\phi,z) &= \sum_k \hat{\mathrm{e}}_{C_k}(z,\phi) \left[ C^+_k f^e_{C^+_k}(\rho) + C^-_k f^e_{C^-_k}(\rho) \right] \\ \overline{H}_C(\rho,\phi,z) &= \sum_k \hat{\mathrm{h}}_{C_k}(z,\phi) \left[ C^+_k f^h_{C^+_k}(\rho) + C^-_k f^h_{C^-_k}(\rho) \right] \end{aligned} \tag{3.136}$$

Finally, in region D

$$\begin{aligned} \overline{E}_D(\rho,\phi,z) &= \sum_l D_l \hat{\mathrm{e}}_{D_l}(z,\phi) f^e_{D_l}(\rho) \\ \overline{H}_D(\rho,\phi,z) &= \sum_l D_l \hat{\mathrm{h}}_{D_l}(z,\phi) f^h_{D_l}(\rho) \end{aligned} \tag{3.137}$$

We assume that the tangential electric and magnetic fields match at all boundaries, therefore

$$\overline{E}_A(\rho = a,\phi,z) = \overline{E}_B(\rho = a,\phi,z) \tag{3.138}$$

$$\overline{H}_A(\rho = a,\phi,z) = \overline{H}_B(\rho = a,\phi,z) \tag{3.139}$$

and

$$\overline{E}_B(\rho = b,\phi,z) = \overline{E}_C(\rho = b,\phi,z) \tag{3.140}$$

$$\overline{H}_B(\rho = b,\phi,z) = \overline{H}_C(\rho = b,\phi,z) \tag{3.141}$$

and finally that

$$\overline{E}_C(\rho = c,\phi,z) = \overline{E}_D(\rho = c,\phi,z) \tag{3.142}$$

$$\overline{H}_C(\rho = c,\phi,z) = \overline{H}_D(\rho = c,\phi,z) \tag{3.143}$$

Using the method as previously, suitable cross-products are applied to the linear equations and multiplied over the boundary. At boundary $\rho = a$ we find the following linear equations:

$$\langle \hat{\mathrm{e}}_{A_i}, \hat{\mathrm{h}}_{A_i} \rangle f^e_{A_i}(a) A_i = \langle \hat{\mathrm{e}}_{B_j}, \hat{\mathrm{h}}_{A_i} \rangle \left\{ f^e_{B_j^+}(a) B_j^+ + f^e_{B_j^-}(a) B_j^- \right\} \tag{3.144}$$

$$\langle \hat{\mathrm{e}}_{A_i}, \hat{\mathrm{h}}_{A_i} \rangle f^h_{A_i}(a) A_i = \langle \hat{\mathrm{e}}_{A_i}, \hat{\mathrm{h}}_{B_j} \rangle \left\{ f^h_{B_j^+}(a) B_j^+ + f^h_{B_j^-}(a) B_j^- \right\} \tag{3.145}$$

This can be expressed in matrix form as

$$\overline{H}_1 = \begin{bmatrix} \tilde{\mathrm{P}}_A \tilde{\mathrm{G}}^{ea}_A & -R_{AB} \tilde{\mathrm{G}}^{ea}_{B+} & -R_{AB} \tilde{\mathrm{G}}^{ea}_{B-} \\ \tilde{\mathrm{P}}_A \tilde{\mathrm{G}}^{ha}_A & -Q_{AB} \tilde{\mathrm{G}}^{ha}_{B+} & -Q_{AB} \tilde{\mathrm{G}}^{ha}_{B-} \end{bmatrix} \begin{bmatrix} \overline{A} \\ \overline{B}^+ \\ \overline{B}^- \end{bmatrix} = 0 \tag{3.146}$$

where

$$\begin{aligned} \tilde{\mathrm{P}}_{Aii} &= \langle \hat{\mathrm{e}}_{A_i}, \hat{\mathrm{h}}_{A_i} \rangle \\ \tilde{\mathrm{G}}^{ea}_{Aii} &= f^e_{A_i}(a) \\ \tilde{\mathrm{G}}^{ha}_{Aii} &= f^h_{A_i}(a) \\ G^{ea}_{Bij+} &= f^e_{B_j}(a) \\ G^{ea}_{Bij-} &= f^e_{B_j}(a) \\ G^{ha}_{Bij+} &= f^h_{B_j}(a) \\ G^{ha}_{Bij-} &= f^h_{B_j}(a) \\ R_{ABij} &= \langle \hat{\mathrm{e}}_{B_j}, \hat{\mathrm{h}}_{A_i} \rangle \\ Q_{ABij} &= \langle \hat{\mathrm{e}}_{A_i}, \hat{\mathrm{h}}_{B_j} \rangle \end{aligned}$$

The linear equations at boundary $\rho = b$ are

$$\langle \hat{\mathrm{e}}_{B_j}, \hat{\mathrm{h}}_{B_j} \rangle \left\{ f^e_{B_j^+}(b) B_j^+ + f^e_{B_j^-}(b) B_j^- \right\} = \langle \hat{\mathrm{e}}_{C_k}, \hat{\mathrm{h}}_{B_j} \rangle \left\{ f^e_{C_k^+}(b) C_k^+ + f^e_{C_k^-}(b) C_k^- \right\} \tag{3.147}$$

$$\langle \hat{\mathrm{e}}_{B_j}, \hat{\mathrm{h}}_{B_j} \rangle \left\{ f^h_{B_j^+}(b) B_j^+ + f^h_{B_j^-}(b) B_j^- \right\} = \langle \hat{\mathrm{e}}_{B_j}, \hat{\mathrm{h}}_{C_k} \rangle \left\{ f^h_{C_k^+}(b) C_k^+ + f^h_{C_k^-}(b) C_k^- \right\} \tag{3.148}$$

Expressing this in matrix form the following equation results:

$$\overline{H}_2 = \begin{bmatrix} \tilde{\mathrm{P}}_B \tilde{\mathrm{G}}^{eb}_{B+} & \tilde{\mathrm{P}}_B \tilde{\mathrm{G}}^{eb}_{B-} & -R_{BC} \tilde{\mathrm{G}}^{eb}_{C+} & -R_{BC} \tilde{\mathrm{G}}^{eb}_{C-} \\ \tilde{\mathrm{P}}_B \tilde{\mathrm{G}}^{hb}_{B+} & \tilde{\mathrm{P}}_B \tilde{\mathrm{G}}^{hb}_{B-} & -Q_{BC} \tilde{\mathrm{G}}^{hb}_{C+} & -Q_{BC} \tilde{\mathrm{G}}^{hb}_{C-} \end{bmatrix} \begin{bmatrix} \overline{B}^+ \\ \overline{B}^- \\ \overline{C}^+ \\ \overline{C}^- \end{bmatrix} = 0 \tag{3.149}$$

where

$$\begin{aligned}
\tilde{\mathrm{P}}_{Bjj} &= \langle \hat{\mathrm{e}}_{B_j}, \hat{\mathrm{h}}_{B_j} \rangle \\
\tilde{\mathrm{G}}^{eb}_{Bjj+} &= f^{e}_{Bj+}(b) \\
\tilde{\mathrm{G}}^{eb}_{Bjj-} &= f^{e}_{Bj-}(b) \\
\tilde{\mathrm{G}}^{hb}_{Bjj+} &= f^{h}_{Bj+}(b) \\
\tilde{\mathrm{G}}^{hb}_{Bjj-} &= f^{h}_{Bj-}(b) \\
G^{eb}_{Cjk+} &= f^{e}_{Ck+}(b) \\
G^{eb}_{Cjk-} &= f^{e}_{Ck-}(b) \\
G^{hb}_{Cjk+} &= f^{h}_{Ck+}(b) \\
G^{hb}_{Cjk-} &= f^{h}_{Ck-}(b) \\
R_{BCjk} &= \langle \hat{\mathrm{e}}_{C_k}, \hat{\mathrm{h}}_{B_j} \rangle \\
Q_{ABjk} &= \langle \hat{\mathrm{e}}_{B_j}, \hat{\mathrm{h}}_{C_k} \rangle
\end{aligned}$$

Finally at boundary $\rho = c$,

$$\langle \hat{\mathrm{e}}_{D_l}, \hat{\mathrm{h}}_{D_l} \rangle f^{e}_{D_l}(c) D_l = \langle \hat{\mathrm{e}}_{C_k}, \hat{\mathrm{h}}_{D_l} \rangle \left\{ f^{e}_{C_k^+}(c) C_k^+ + f^{e}_{C_k^-}(c) C_k^- \right\} \tag{3.150}$$

$$\langle \hat{\mathrm{e}}_{D_l}, \hat{\mathrm{h}}_{D_l} \rangle f^{h}_{D_l}(c) D_l = \langle \hat{\mathrm{e}}_{D_l}, \hat{\mathrm{h}}_{C_k} \rangle \left\{ f^{h}_{C_k^+}(c) C_k^+ + f^{h}_{C_k^-}(c) C_k^- \right\} \tag{3.151}$$

which can be written as

$$\overline{H}_3 = \begin{bmatrix} Q_{CD}\tilde{\mathrm{G}}^{ec}_{C+} & Q_{CD}\tilde{\mathrm{G}}^{ec}_{C-} & -\tilde{\mathrm{P}}_D\tilde{\mathrm{G}}^{ec}_{D} \\ R_{CD}\tilde{\mathrm{G}}^{hc}_{C+} & R_{CD}\tilde{\mathrm{G}}^{hc}_{C-} & -\tilde{\mathrm{P}}_D\tilde{\mathrm{G}}^{hc}_{D} \end{bmatrix} \begin{bmatrix} \overline{C^+} \\ \overline{C^-} \\ \overline{D} \end{bmatrix} = 0 \tag{3.152}$$

where

$$\begin{aligned}
\tilde{\mathrm{P}}_{Dll} &= \langle \hat{\mathrm{e}}_{D_l}, \hat{\mathrm{h}}_{D_l} \rangle \\
\tilde{\mathrm{G}}^{ec}_{Dll} &= f^{e}_{D_l}(c) \\
\tilde{\mathrm{G}}^{hc}_{Dll} &= f^{h}_{D_l}(c) \\
G^{ec}_{Ckl+} &= f^{e}_{C_k}(c) \\
G^{ec}_{Ckl-} &= f^{e}_{C_k}(c) \\
G^{hc}_{Ckl+} &= f^{h}_{C_k}(c) \\
G^{hc}_{Ckl-} &= f^{h}_{C_k}(c) \\
R_{CDkl} &= \langle \hat{\mathrm{e}}_{D_l}, \hat{\mathrm{h}}_{C_k} \rangle \\
Q_{CDkl} &= \langle \hat{\mathrm{e}}_{C_k}, \hat{\mathrm{h}}_{D_l} \rangle
\end{aligned}$$

The matrix equations, Equation 3.146, Equation 3.149 and Equation 3.152 can be combined into a single matrix which is given by

$$\begin{bmatrix} \tilde{\mathrm{P}}_A\tilde{\mathrm{G}}_A^{ea} & -R_{AB}\tilde{\mathrm{G}}_{B+}^{ea} & -R_{AB}\tilde{\mathrm{G}}_{B-}^{ea} & Z & Z & Z \\ \tilde{\mathrm{P}}_A\tilde{\mathrm{G}}_A^{ha} & -Q_{AB}\tilde{\mathrm{G}}_{B+}^{ha} & -Q_{AB}\tilde{\mathrm{G}}_{B-}^{ha} & Z & Z & Z \\ Z & \tilde{\mathrm{P}}_B\tilde{\mathrm{G}}_{B_+}^{eb} & \tilde{\mathrm{P}}_B\tilde{\mathrm{G}}_{B_-}^{eb} & -R_{BC}\tilde{\mathrm{G}}_{C+}^{eb} & -R_{BC}\tilde{\mathrm{G}}_{C-}^{eb} & Z \\ Z & \tilde{\mathrm{P}}_B\tilde{\mathrm{G}}_{B_+}^{hb} & \tilde{\mathrm{P}}_B\tilde{\mathrm{G}}_{B_-}^{hb} & -Q_{BC}\tilde{\mathrm{G}}_{C+}^{hb} & -Q_{BC}\tilde{\mathrm{G}}_{C-}^{hb} & Z \\ Z & Z & Z & Q_{CD}\tilde{\mathrm{G}}_{C+}^{ec} & Q_{CD}\tilde{\mathrm{G}}_{C-}^{ec} & -\tilde{\mathrm{P}}_D\tilde{\mathrm{G}}_D^{ec} \\ Z & Z & Z & R_{CD}\tilde{\mathrm{G}}_{C+}^{hc} & R_{CD}\tilde{\mathrm{G}}_{C-}^{hc} & -\tilde{\mathrm{P}}_D\tilde{\mathrm{G}}_D^{hc} \end{bmatrix} \begin{bmatrix} \overline{A} \\ \overline{B}^+ \\ \overline{B}^- \\ \overline{B}^+ \\ \overline{B}^- \\ \overline{D} \end{bmatrix} = 0$$

where Z is a NxN zero filled matrix. This matrix can now be simplified into a matrix which is only in terms of $B^+$ and $C^+$. Searching for the zeros of the determinant of the system of linear equations gives the resonant frequencies of the modes being considered.

### Implementation of Four-layer Radial Mode Matching

In order to have a point of comparison, the four-layer implementation was used to investigate a dielectric pill resonator in the central region, surrounded by 3 air-filled regions. The results were then compared to the results derived by the two-layer implementation for the pill resonator. Similarly, the ring resonator surrounded by two air filled regions was modelled and the results compared to the results derived from the three-layer implementation for the simple ring resonator implementation. The results are compared in Table 3.4 for the post resonator and Table 3.5 for the post resonator. Once again, the hybrid modes with a PMC symmetry wall at $z = 0$ seem to be more inaccurate than results for other modes, especially in the case of the ring resonator.

**Table 3.4:** *Comparison of Resonant Frequencies [GHz] for the modes in pill resonator for the two layer and four layer implementation, for matrix size, N=10*

| Mode | Two-layer | Four-layer | Percent % |
|---|---|---|---|
| $TEE_{01}$ | 5.2440 | 5.2450 | 0.00 |
| $TME_{01}$ | 4.6650 | 4.6620 | 0.06 |
| $TEH_{01}$ | 3.2560 | 3.2590 | 0.09 |
| $HEE_{11}$ | 4.1010 | 4.1010 | 0.00 |
| $HEE_{12}$ | 5.8600 | 5.8587 | 0.22 |
| $HEH_{11}$ | 4.0074 | 4.0040 | 0.084 |
| $HEH_{12}$ | 5.2151 | 5.2090 | 0.11 |

**Table 3.5:** *Comparison of Resonant Frequencies [GHz] for the modes in ring resonator for the two layer and four layer implementation, for matrix size, N=10*

| Mode | Two-layer | Four-layer | Percent % |
|---|---|---|---|
| $TEH_{01}$ | 3.1650 | 3.1614 | 0.11 |
| $TME_{01}$ | 4.8950 | 4.8886 | 0.13 |
| $HEH_{11}$ | 4.3636 | 4.2140 | 3.4 |
| $HEH_{21}$ | 5.3809 | 5.2393 | 2.63 |
| $HEH_{31}$ | 7.6371 | 7.6231 | 0.18 |

Since, it takes more time and more modes, to derive properly converged resonant frequencies for the four layer implementation, it seems likely that these results would have been more accurate if a larger matrix size had been used. Due to time constraints this aspect was not investigated further.

## 3.3 Axial Mode Matching

To apply axial mode matching to a structure as is shown in Figure 3.1, the resulting regions are either homogenous or dielectric loaded waveguides. The fields in homogenous lossless cavities have been derived in the previous chapter. However, it is still necessary to derive the fields in a dielectric loaded dielectric waveguide. This section first derives the fields in dielectric loaded waveguides. The fields of an infinite dielectric loaded waveguide are then plotted and discussed. Then the theory of axial mode matching is presented.

### 3.3.1 Dielectric loaded Waveguides

In this case it is assumed that the waveguide extends to infinity in the $\pm z$ direction. The radius of the dielectric rod is $a$, and the radius of the cylindrical metallic sheath is $b$. The permittivity of the dielectric is defined as $\epsilon_1 = \epsilon_{r1}\epsilon_0$, and the permittivity of the material in the outer region is $\epsilon_2 = \epsilon_{r2}\epsilon_0$. Figure 3.11 shows such a dielectric loaded waveguide. The structure is divided into 2 regions with a radial boundary, where region 1 is bounded by $0 \leq \rho < a$ and region 2 is bounded by $a \leq \rho < b$.

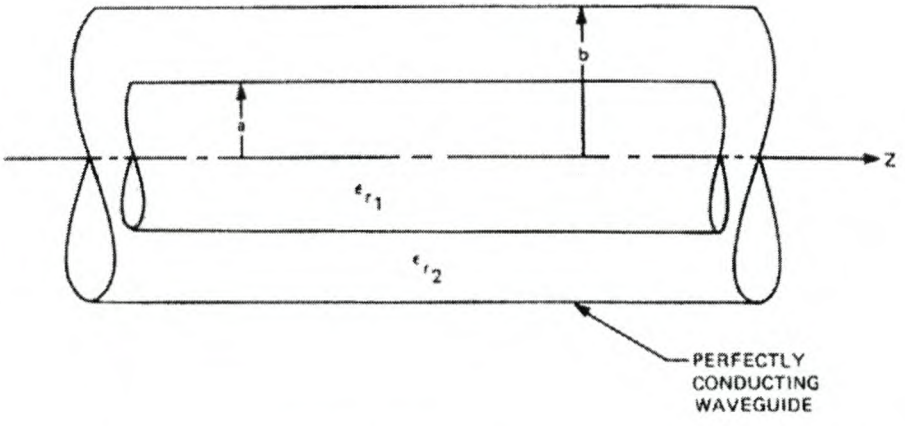


**Figure 3.11:** *A circular dielectric loaded waveguide. It is important to note that both the dielectric rod and the enclosing metallic sheath extend to infinity in the $\pm z$ directions.*

The fields in this structure are divided into pure $TE_{0m}$, $TM_{0m}$ and hybrid mode fields $HE_{nm}$, where the hybrid modes consist of combinations of TE and TM modes. It is important to note that only $TE_{0m}$ and $TM_{0m}$ modes can exist in this structure where (as was the case for modes in cylindrical structure) $n$ describes the amount of angular field variations and $m$ describes the amount of radial variations. The TE and TM modes are investigated separately.

**TE fields**

From Equation 2.45 we can write

$$\Psi_i^f = (A_i e^{\gamma z} + B_i e^{-\gamma z}) * (C_i \cos(n\phi) + D_i \sin(n\phi)) * (E_i J_n(\beta_i \rho) + F_i Y_n(\beta_i \rho)) \quad (3.153)$$

where $i = 1, 2$ in region 1 and 2. Once again the structure can be divided into LEC and LMC solutions. In this derivation we choose to work with LMC fields. Therefore $C_1 = C_2 = 0$ for the TE solution.

The next step is to investigate the $\rho$ dependency. In region 1 the solution must be finite. Therefore $F_1 = 0$ and the radial dependance $R_1(\beta_1\rho) = E_1 J_n(\beta_1\rho)$ where $\beta_1^2 = \kappa_1^2 + \gamma^2$. Additionally, $\kappa_1^2 = \epsilon_{r1}\kappa_0^2$. In region 2, the Bessel functions $J_n$ and $Y_n$ can be re-written as $I_n$ and $K_n$. In this section it is assumed that the fields in region 2 are non-propagating and $\beta_2 = -(\gamma^2 + \kappa_2^2) > 0$ where $\kappa_2^2 = \epsilon_{r2}\kappa_0^2$. If $\beta_2 = \gamma^2 - \kappa_2^2 < 0$, then the fields are propagating in region 2 and it is necessary to replace $I_n$ with $J_n$ and $K_n$ with $Y_n$. The $\rho$ dependency in region 2 is therefore written as $R(\beta_2\rho) = (E_2 I_n(\beta_2\rho) + F_2 K_n(\beta\rho)$. The boundary at $\rho = b$, is assumed to be a perfect electric conductor (PEC). Therefore $H_{\rho,2} = 0$ and

$$\beta_2 * (E_2 I_n'(\beta_2 b) + F_2 K_n'(\beta_2 b)) = 0 \quad (3.154)$$

This means that

$$F_2 = -\frac{E_2 I_n'(\beta_2 b)}{K_n'(\beta_2 b)} \quad (3.155)$$

The tangential magnetic and electric fields must match at the boundary. Therefore $H_{\phi,1} = H_{\phi,2}$, $H_{z,1} = H_{z,2}$, $E_{\phi,1} = E_{\phi,2}$ and $E_{z,1} = E_{z,2}$. Given Equations 2.49 and 2.46, we can derive the electric and magnetic fields. From $H_{\phi,1} = H_{\phi,2}$ and $H_{z,1} = H_{z,2}$ it follows that at $\rho = a$

$$\begin{aligned} E_1 J_n(\beta_1 a) &= E_2 I_n(\beta_2 a) + F_2 K_n(\beta_2 a) \quad (3.156) \\ &= E_2 I_n(\beta_2 a) - \frac{E_2 I_n'(\beta_2 b)}{K_n'(\beta_2 b)} K_n(\beta_2 a) \\ &= E_2 \left( I_n(\beta_2 a) - \frac{I_n'(\beta_2 b)}{K_n'(\beta_2 b)} K_n(\beta_2 a) \right) \end{aligned}$$

and

$$E_2 = E_1 \frac{J_n(\beta_1 a) K_n'(\beta_2 b)}{I_n(\beta_2 a) K_n'(\beta_2 b) - I_n'(\beta_2 b) K_n(\beta 2_a)} \quad (3.157)$$

The $\rho$ dependency in region 2 can now be written as

$$\begin{aligned} R(\rho) &= E_2 I_n(\beta_2 \rho) + F_2 K_n(\beta_2 \rho) \quad (3.158) \\ &= E_1 J_n(\beta_1 a) \frac{I_n(\beta_2 \rho) K_n'(\beta_2 b) - I_n'(\beta_2) K_n(\beta_2 \beta)}{I_n(\beta_2 a) K_n'(\beta_2 b) - I_n'(\beta_2 b) K_n(\beta_2 a)} \quad (3.159) \end{aligned}$$

This gives us the final wave equations

$$\Psi_1^f = (A_1 e^{\gamma z} + B_1 e^{-\gamma z}) * D_1 \sin(n\phi) * (E_1\ J_n(\beta_1 \rho)) \tag{3.160}$$

and

$$\Psi_2^f = (A_2 e^{\gamma z} + B_2 e^{-\gamma z}) * D_2 \sin(n\phi) * E_1 J_n(\beta_1 a) \frac{I_n(\beta_2\rho)K_n'(\beta_2 b) - I_n'(\beta_2)K_n(\beta_2\beta)}{I_n(\beta_2 a)K_n'(\beta_2 b) - I_n'(\beta_2 b)K_n(\beta_2 a)} \tag{3.161}$$

Combining all the constants, the field equation can be written as

$$\Psi_i^f = K_i^f Z(\gamma z) \sin(n\phi) R_i(\beta_i \rho) \tag{3.162}$$

where $R_i(\rho) = \begin{cases} R_1(\beta_1\rho) & = J_n(\beta_1\rho), \\ R_2(\beta_2\rho) & = J_n(\beta_1 a) * \frac{I_n(\beta_2\rho)K_n'(\beta_2 b) - I_n'(\beta_2)K_n(\beta_2\beta)}{I_n(\beta_2 a)K_n'(\beta_2 b) - I_n'(\beta_2 b)K_n(\beta_2 a)}. \end{cases}$

It is important to remember that due to the way in which $Z(\gamma z)$ was defined,

$$Z(\gamma z) = \gamma \frac{dZ(\gamma z)}{dz} = \gamma Z(z) \tag{3.163}$$

Substituting Equation 3.162 into Equations 2.26 - 2.31, it is possible to derive the TE field components from $\Psi^f$ where $\Psi^a = 0$ and

$$H_{z,i} = \frac{1}{\jmath\omega\mu}\left(\frac{d^2}{dz^2} + \kappa^2\right)\Psi_i^f \tag{3.164}$$

with $i = 1, 2$ representing fields in regions 1 or region 2. This gives us

$$H_{z,i} = \begin{cases} H_{z,1} & = \frac{1}{\jmath\omega\mu}\beta_1^2 K_1^f Z(\gamma z)\sin(n\phi)J_n(\beta_1\rho), \\ H_{z,2} & = \frac{-1}{\jmath\omega\mu}\beta_2^2 K_2^f Z(\gamma z)\sin(n\phi)J_n(\beta_1 a) * \frac{I_n(\beta_2\rho)K_n'(\beta_2 b) - I_n'(\beta_2)K_n(\beta_2\beta)}{I_n(\beta_2 a)K_n'(\beta_2 b) - I_n'(\beta_2 b)K_n(\beta_2 a)}, \end{cases} \tag{3.165}$$

To simplify the previous equation, a function $P_n(\beta_2\rho)$ is defined so that

$$P_n(\beta_2\rho) = J_n(\beta_1 a) * \frac{I_n(\beta_2\rho)K_n'(\beta_2 b) - I_n'(\beta_2)K_n(\beta_2\beta)}{I_n(\beta_2 a)K_n'(\beta_2 b) - I_n'(\beta_2 b)K_n(\beta_2 a)} \tag{3.166}$$

and $H_{z,i}$ can be re-written as

$$H_{z,i} = \begin{cases} H_{z,1} & = \frac{1}{\jmath\omega\mu}\beta_1^2 K_1^f Z(\gamma z)\sin(n\phi)J_n(\beta_1\rho), \\ H_{z,2} & = \frac{-1}{\jmath\omega\mu}\beta_2^2 K_2^f Z(\gamma z)\sin(n\phi)P_n(\beta_2\rho), \end{cases} \tag{3.167}$$

In order to derive fields in the same format as Chen [9], it is necessary to re-write $K_1^f = A\gamma\alpha/\beta_1^2$ and $K_2^f = -A\gamma\alpha/\beta_2^2$ where

$$\alpha = -\frac{U_n}{V_n} = -\frac{nJ_n(\beta_1 a)\left[\frac{1}{(\beta_1 a)^2} + \frac{1}{(\beta_2 a)^2}\right]}{\frac{J_n'(\beta_1 a)}{\beta_1 a} + \frac{P_n'(\beta_2 a)}{\beta_2 a}} \tag{3.168}$$

This is the solution to the first-order differential equation

$$\frac{dy}{dx} = \tan(\alpha(x,y)) = \frac{E_y(x,y)}{E_x(x,y)} = \frac{E_r\sin(\phi) + E_\phi\cos(\phi)}{E_r\cos(\phi) - E_\phi\sin(\phi)} \tag{3.169}$$

where $\alpha$ is the angle between the field vector at a given point (x,y) and the positive x-axis. The equation was derived by Nagelberg [11].

Therefore, the TE field equations are given by

$$E_{rho,i} = \begin{cases} E_{\rho 1} = \frac{-d\Psi_1^f}{\rho d\phi} = -\frac{AZ(\gamma z)\cos(n\phi)\gamma}{\beta_1^2}[\frac{\alpha n J_n(\beta_1\rho)}{\rho}], \\ E_{\rho,2} = \frac{-d\Psi_2^f}{\rho d\phi} = \frac{AZ(\gamma z)\cos(n\phi)\gamma}{\beta_2^2}[\frac{\alpha n P_n(\beta_2\rho)}{\rho}]. \end{cases} \tag{3.170}$$

$$E_{\phi,i} = \begin{cases} E_{\phi 1} = \frac{d\Psi_1^f}{d\rho} = \frac{AZ(\gamma z)\sin(n\phi)\gamma}{\beta_1^2}[\alpha\beta_1 J_n'(\beta_1\rho)], \\ E_{\phi,2} = \frac{d\Psi_2^f}{d\rho} = -\frac{AZ(\gamma z)\sin(n\phi)\gamma_2}{\beta_2^2}[\alpha\beta_2 P_n'(\beta_2\rho)]. \end{cases} \tag{3.171}$$

$$H_{\rho,i} = \begin{cases} H_{\rho 1} = \frac{1}{j\omega\mu}\frac{d^2\Psi_1^f}{d\rho dz} = \frac{AZ(\gamma z)\sin(n\phi)}{\beta_1^2 j\omega\mu}[\alpha\gamma^2\beta_1 J_n'(\beta_1\rho)], \\ H_{\rho,2} = \frac{1}{j\omega\mu}\frac{d^2\Psi_2^f}{d\rho dz} = -\frac{AZ(\gamma z)\sin(n\phi)}{\beta_2^2 j\omega\mu}[\alpha\gamma^2\beta_2 P_n'(\beta_2\rho)]. \end{cases} \tag{3.172}$$

$$H_{\phi,i} = \begin{cases} H_{\phi 1} = \frac{1}{j\omega\mu\rho}\frac{d^2\Psi_1^f}{d\phi dz} = \frac{AZ(\gamma z)\cos(n\phi)}{\beta_1^2 j\omega\mu}[\frac{\alpha\gamma^2 n J_n(\beta_1\rho)}{\rho}], \\ H_{\phi,2} = \frac{1}{j\omega\mu\rho}\frac{d^2\Psi_2^f}{d\phi dz} = \frac{-AZ(\gamma z)\cos(n\phi)}{\beta_2^2 j\omega\mu}[\frac{\alpha\gamma^2 n P_n(\beta_2\rho)}{\rho}]. \end{cases} \tag{3.173}$$

**TM fields**

From Equation 2.63 we can write

$$\Psi_i^a = (A_i e^{\gamma z} + B_i e^{-\gamma z}) * (C_i\cos(n\phi) + D_i\sin(n\phi)) * (E_i J_n(\beta_i\rho) + F_i Y_n(\beta\rho)) \tag{3.174}$$

where $i = 1, 2$. The structure is divided into LEC and LMC solutions. Working with LMC fields, results in $D_1 = D_2 = 0$.

Now the $\rho$ dependency is looked at. In region 1 the solution must be finite. Therefore $F_1 = 0$. In region 2, the Bessel functions $J_n$ and $Y_n$ are re-written as $I_n$ and $K_n$. The $\rho$ dependency in region 2 is written as $R(\beta_2\rho) = E_2 I_n(\beta_2\rho) + F_2 K_n(\beta\rho)$ and the boundary at $\rho = b$, is assumed to be a perfect electric conductor (PEC). Therefore $E_z = 0$ and

$$E_2 I_n(\beta_2 b) + F_2 K_n(\beta_2 b) = 0 \tag{3.175}$$

This means that

$$F_2 = -\frac{E_2 I_n(\beta_2 b)}{K_n(\beta_2 b)} \tag{3.176}$$

The tangential magnetic and electric fields must match at the boundary. Therefore $H_{\phi,1} = H_{\phi,2}$, $H_{z,1} = H_{z,2}$, $E_{\phi,1} = E_{\phi,2}$ and $E_{z,1} = E_{z,2}$. From Equations 2.49 and 2.46, we can derive the electric and magnetic fields and from $E_{\phi,1} = E_{\phi,2}$ and $E_{z,1} = E_{z,2}$ it follows that at $\rho = a$

$$\begin{aligned} E_1 J_n(\beta_1 a) &= E_2 I_n(\beta_2 a) + F_2 K_n(\beta_2 a) \\ &= E_2 I_n(\beta_2 a) - \frac{E_2 I_n(\beta_2 b)}{K_n(\beta_2 b)} K_n(\beta_2 a) \\ &= E_2\left(I_n(\beta_2 a) - \frac{I_n(\beta_2 b)}{K_n(\beta_2 b)} K_n(\beta_2 a)\right) \end{aligned} \tag{3.177}$$

and

$$E_2 = E_1 \frac{J_n(\beta_1 a)K_n(\beta_2 b)}{I_n(\beta_2 a)K_n(\beta_2 b) - I_n(\beta_2 b)K_n(\beta 2_a)} \tag{3.178}$$

The $\rho$ dependency in region 2 can now be written as

$$R(\rho) = E_2 I_n(\beta_2 \rho) + F_2 K_n(\beta_2 \rho) \tag{3.179}$$

$$= E_1 J_n(\beta_1 a) \frac{I_n(\beta_2 \rho)K_n(\beta_2 b) - I_n(\beta_2)K_n(\beta_2 \beta)}{I_n(\beta_2 a)K_n(\beta_2 b) - I_n(\beta_2 b)K_n(\beta_2 a)} \tag{3.180}$$

This gives us the final wave equations

$$\Psi_1^a = (A_1 e^{\gamma z} + B_1 e^{-\gamma z}) * C_1 \cos(n\phi) * (E_1\ J_n(\beta_1 \rho)) \tag{3.181}$$

and

$$\Psi_2^a = (A_2 e^{\gamma z} + B_2 e^{-\gamma z}) * C_2 \cos(n\phi) * E_1 J_n(\beta_1 a) \frac{I_n(\beta_2 \rho)K_n(\beta_2 b) - I_n(\beta_2)K_n(\beta_2 \beta)}{I_n(\beta_2 a)K_n(\beta_2 b) - I_n(\beta_2 b)K_n(\beta_2 a)} \tag{3.182}$$

Combining all the constants, the field equation can be written as

$$\Psi_i^a = K_i^a Z(\gamma z) \cos(n\phi) R_i(\beta_i \rho) \tag{3.183}$$

where $R_i(\rho) = \begin{cases} R_1(\beta_1\rho) = J_n(\beta_1\rho) & \text{in Region 1,} \\ R_2(\beta_2\rho) = J_n(\beta_1 a) * \frac{I_n(\beta_2\rho)K_n(\beta_2 b) - I_n(\beta_2)K_n(\beta_2\beta)}{I_n(\beta_2 a)K_n(\beta_2 b) - I_n(\beta_2 b)K_n(\beta_2 a)} & \text{in Region 2.} \end{cases}$

By substituting Equation 3.183 into Equations 2.26 - 2.31, it is possible to derive the TM field components from $\Psi^a$ where $\Psi^f = 0$ and

$$E_{z,i} = \frac{1}{j\omega\epsilon}\left(\frac{d^2}{dz^2} + \kappa^2\right)\Psi_i^a \tag{3.184}$$

This gives us

$$E_{z,i} = \begin{cases} E_{z,1} = \frac{1}{j\omega\epsilon}\beta_1^2 K_1^a Z(\gamma z)\cos(n\phi)J_n(\beta_1\rho), \\ E_{z,2} = \frac{-1}{j\omega\epsilon}\beta_2^2 K_2^a Z(\gamma z)\cos(n\phi)J_n(\beta_1 a) * \frac{I_n(\beta_2\rho)K_n(\beta_2 b) - I_n(\beta_2)K_n(\beta_2\beta)}{I_n(\beta_2 a)K_n(\beta_2 b) - I_n(\beta_2 b)K_n(\beta_2 a)}, \end{cases} \tag{3.185}$$

To simplify the previous equation, a function $R_n(\beta_2\rho)$ is defined so that

$$R_n(\beta_2\rho) = J_n(\beta_1 a) * \frac{I_n(\beta_2\rho)K_n(\beta_2 b) - I_n(\beta_2)K_n(\beta_2\beta)}{I_n(\beta_2 a)K_n(\beta_2 b) - I_n(\beta_2 b)K_n(\beta_2 a)} \tag{3.186}$$

and $E_{z,i}$ can be re-written as

$$E_{z,i} = \begin{cases} E_{z,1} = \frac{1}{j\omega\epsilon}\beta_1^2 K_1^a Z(\gamma z)\cos(n\phi)J_n(\beta_1\rho), \\ E_{z,2} = \frac{-1}{j\omega\epsilon}\beta_2^2 K_2^a Z(\gamma z)\cos(n\phi)R_n(\beta_2\rho), \end{cases} \tag{3.187}$$

To derive fields in the same format as Chen [9], re-write $K_1^a = -A\jmath\omega\epsilon/\beta_1^2$ and $K_2^a = A\jmath\omega\epsilon/\beta_2^2$. The TM field equations are now given by

$$H_{\rho,i} = \begin{cases} H_{\rho 1} = \frac{d\Psi_1^a}{\rho d\phi} = -\frac{AZ(\gamma z)\sin(n\phi)\kappa_1^2}{\beta_1^2\jmath\omega\mu}[\frac{nJ_n(\beta_1\rho)}{\rho}], \\ H_{\rho,2} = \frac{d\Psi_2^a}{\rho d\phi} = \frac{AZ(\gamma z)\sin(n\phi)\kappa_2^2}{\beta_2^2}[\frac{nP_n(\beta_2\rho)}{\rho}]. \end{cases} \tag{3.188}$$

$$H_{\phi,i} = \begin{cases} H_{\phi 1} = \frac{-d\Psi_1^a}{d\rho} = \frac{-AZ(\gamma z)\cos(n\phi)\kappa_1^2}{\beta_1^2\jmath\omega\mu}[\beta_1 J_n'(\beta_1\rho)], \\ H_{\phi,2} = \frac{-d\Psi_2^a}{d\rho} = \frac{AZ(\gamma z)\cos(n\phi)\kappa_2^2}{\beta_2^2\jmath\omega\mu}[\beta_2 P_n'(\beta_2\rho)]. \end{cases} \tag{3.189}$$

$$E_{\rho,i} = \begin{cases} E_{\rho 1} = \frac{1}{\jmath\omega\epsilon}\frac{d^2\Psi_1^a}{d\rho dz} = \frac{-AZ(\gamma z)\cos(n\phi)}{\beta_1^2}[\gamma\beta_1 J_n'(\beta_1\rho)], \\ E_{\rho,2} = \frac{1}{\jmath\omega\epsilon}\frac{d^2\Psi_2^a}{d\rho dz} = \frac{AZ(\gamma z)\cos(n\phi)}{\beta_2^2}[\gamma\beta_2 P_n'(\beta_2\rho)]. \end{cases} \tag{3.190}$$

$$E_{\phi,i} = \begin{cases} E_{\phi 1} = \frac{1}{\jmath\omega\epsilon\rho}\frac{d^2\Psi_1^a}{d\phi dz} = \frac{AZ(\gamma z)\sin(n\phi)}{\beta_1^2}[\frac{\gamma nJ_n(\beta_1\rho)}{\rho}], \\ E_{\phi,2} = \frac{1}{\jmath\omega\epsilon\rho}\frac{d^2\Psi_2^a}{d\phi dz} = \frac{-AZ(\gamma z)\sin(n\phi)}{\beta_2^2}[\frac{\gamma nP_n(\beta_2\rho)}{\rho}]. \end{cases} \tag{3.191}$$

### Characteristic Equation

In order to solve for the axial propagation constant, $\gamma$, it is necessary to derive the characteristic equation for fields in dielectric loaded waveguides. This is done by examining the fields at the boundary. In this case, we concentrate on $H_{\phi,1} = H_{\phi,2}$ at the boundary where $\rho = a$. Using the field solutions for hybrid modes, we obtain the following equation:

$$\frac{1}{\beta_1^2}\left[-\kappa_1^2\beta_1 J_n'(\beta_1 a) + \frac{\alpha\gamma^2 nJ_n(\beta_1 a)}{a}\right] = \frac{1}{\beta_2^2}\left[\kappa_2^2\beta_2 R_n'(\beta_2 a) - \frac{\alpha\gamma^2 nP_n(\beta_2 a)}{a}\right] \tag{3.192}$$

If $\gamma^2$ is factored out one finds that

$$\gamma^2\left[\frac{\alpha nJ_n(\beta_1 a)}{a}\frac{1}{\beta_1^2} + \frac{\alpha nP_n(\beta_2 a)}{a}\frac{1}{\beta_2^2}\right] = \frac{\kappa_1^2\beta_1 J_n'(\beta_1 a)}{\beta_1^2} + \frac{\kappa_2^2\beta_2 R_n'(\beta_2 a)}{\beta_2^2} \tag{3.193}$$

To simplify the equation, two functions are defined such that

$$X = \frac{\alpha nJ_n(\beta_1 a)}{a}\frac{1}{\beta_1^2} + \frac{\alpha nP_n(\beta_2 a)}{a}\frac{1}{\beta_2^2} \tag{3.194}$$

$$Y = \frac{\kappa_1^2\beta_1 J_n'(\beta_1 a)}{\beta_1^2} + \frac{\kappa_2^2\beta_2 R_n'(\beta_2 a)}{\beta_2^2} \tag{3.195}$$

Working with X,

$$X = \frac{\alpha nJ_n(\beta_1 a)}{a}\frac{1}{\beta_1^2} + \frac{\alpha nP_n(\beta_2 a)}{a}\frac{1}{\beta_2^2} \tag{3.196}$$

$$= \alpha n\left[\frac{J_n(\beta_1 a)}{a}\frac{1}{\beta_1^2} + \frac{P_n(\beta_2 a)}{a}\frac{1}{\beta_2^2}\right] \tag{3.197}$$

$$= \alpha nJ_n(\beta_1 a)\left[\frac{1}{\beta_1^2 a} + \frac{1}{\beta_2^2 a}\right] \tag{3.198}$$

$$= -\frac{U_n}{V_n}aU_n \tag{3.199}$$

from the definition of $\alpha$ 3.168 and the fact that at $\rho = a$, $P_n(\beta_2\rho) = J_n(\beta_1\rho)$. Furthermore, Y can also be re-written as

$$Y = \frac{\kappa_1^2\beta_1 J_n'(\beta_1 a)}{\beta_1^2} + \frac{\kappa_2^2\beta_2 R_n'(\beta_2 a)}{\beta_2^2} \tag{3.200}$$

$$= \kappa_0^2 W_n a \tag{3.201}$$

Therefore by substituting X and Y into Equation 3.193, we can derive the characteristic equation in terms of $\gamma^2$ as

$$U_n^2\gamma^2 + \kappa_0^2 V_n W_n = 0 \tag{3.202}$$

The values of $\gamma$ that satisfy this equation are valid propagation constants for modes at a particular frequency. Once $\gamma$ has been computed it is possible to compute $\beta_1$ and $\beta_2$ necessary to determine the field distributions. TE and TM modes can be considered as special cases of hybrid modes, where $n = 0$. If $n = 0$, $U_0 = 0$ and the characteristic equation simplifies to $V_0 W_0 = 0$, where $V_0 = 0$ is the eigenvalue equation for the TE modes, and $W_0 = 0$ is the eigenvalue equation for the TM modes.

Next the dielectric loaded waveguide implementation is discussed. This model can be used as a building block in the implementation of the axial mode matching technique that was previously discussed. It can also give insight into the potential field distribution of resonant modes in a dielectric resonator. This aspect has been made use of in the design process. Knowledge of the field distributions can also provide valuable information which can be used to place probes in the correct position to excite the desired fields.

### 3.3.2 Implementation of Dielectric Loaded Waveguide

In an attempt to gain a better understanding of the field distributions in dielectric resonators, the fields in dielectric loaded waveguides were investigated in detail. Since the fields in the central plane ($z = 0$) of a simple dielectric resonator can be modelled with the use of a dielectric loaded waveguide, the resultant plotted fields should be a good model of fields in the central region of a dielectric loaded resonator. It should be understood that the field distribution of a dielectric loaded resonator will change more and more from that of a dielectric loaded waveguide as one moves away from the central plane of the resonator.

The fields that exist in a dielectric loaded waveguide have been derived in Section 3.3.1. The first step in modelling these fields is to solve for the axial propagation constant $\gamma$ at the desired frequency. This is done by solving the characteristic equation using some sort of root finding algorithm. Once $\gamma$ is known, we can substitute it back into the field equations and plot the electric and magnetic fields along the $\rho - \phi$ axis. To test the accuracy of the implementation, the resultant $\gamma$ values were compared to work done by Chen in [7]. Some of the modes that were compared are summarized in Table 3.6. It can be seen that the obtained results were almost identical to those obtained by Chen.

**Table 3.6:** *Parameters of the Field Plots in Figures 3.12 - 3.15*

| Figure | Mode | Frequency [GHz] | $\gamma$ [7] | $\gamma$ (this implementation) | Percent error % |
|---|---|---|---|---|---|
| 3.12 | HE11 | 4.0 | 0.0574 | 0.0574 | 0.00 |
| 3.13 | HE12 | 4.0 | 0.1119 | 0.1119 | 0.00 |
| 3.14 | HE21 | 4.0 | 0.9364 | 0.9363 | 0.10 |
| 3.15 | HE24 | 8.0 | 0.2254 | 0.2255 | 0.44 |

Table 3.6 provides the information necessary to explain the obtained results as shown in the figures. The first column consists of a list of the figures that were included. Each row provides the necessary information for each mode that is plotted in the figure. The information provided consists of the name of the mode, the frequency at which it was investigated, the axial propagation factor obtained from [7], and the actual propagation factor used in the analysis. The structure has the following parameters: The inner radius is given by $\rho = 9.9mm$ and the outer radius is given by $\rho = 12.7mm$. The relative permittivity of the inner dielectric is $\epsilon_{r1} = 37.6$ and the outer region is assumed to be air-filled with $\epsilon_{r2} = 1$.

The first sub-figure (a) of each figure shows the normalized electric and magnetic field intensity as it changes along the $\rho$ axis from the central axis to the outer circumference while keeping $\phi$ constant. One important fact to note is that at the inner boundary $E_\phi$, $H_\phi$ and $H_\rho$ are continuous. This means that the important condition of tangential field continuity at the boundary has been satisfied. The second sub-figure (b) shows the magnetic field distribution in the $\rho - \phi$ plane. The arrows indicate the direction of the transverse electric fields and the color in the background indicates the normalized field intensity at that specific point. The lightest values indicate the highest values, and the darkest colors indicate the lowest values. Subfigure (c) shows the electric field distribution in the $\rho - \phi$ plane.

The fields in this section are used to gain a more detailed understanding of what fields in a dielectric loaded resonator would look like. However, they are only approximations. In order to derive the exact fields, it is necessary to use mode matching. In this case, one would solve for the resonant frequencies of the dielectric resonator. Then the field coefficients, $A_i$ and $B_j$ are solved for and substituted into the field equations for each region. While this technique was not implemented, the theory is described below for the sake of completeness.

**Figure 3.12:** *Field Distribution of the $HE_{11}$ hybrid mode in an infinite dielectric loaded waveguide*

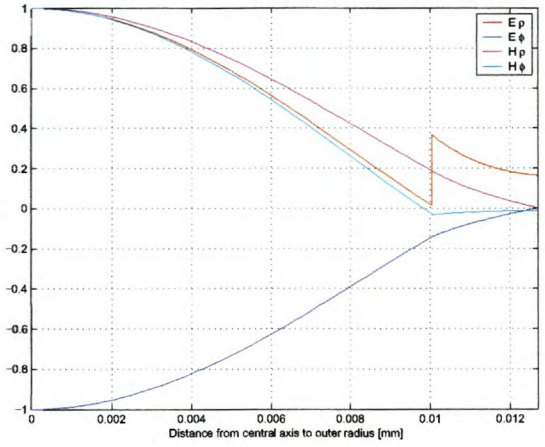


(a) Normalized Field Intensity along the $\rho$ axis for $\phi = 0$

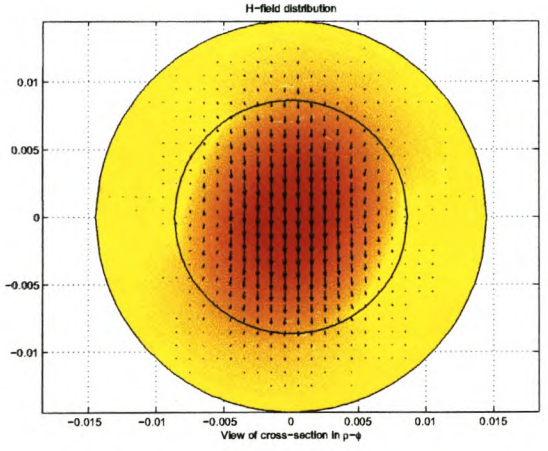


(b) $\rho$-$\phi$ plane Magnetic Field distribution

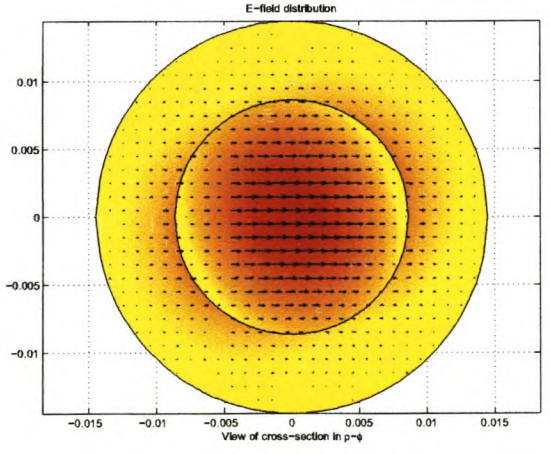


(c) $\rho$-$\phi$ plane Electric Field distribution

**Figure 3.13:** *Field Distribution of the $HE_{12}$ hybrid mode in an infinite dielectric loaded waveguide*

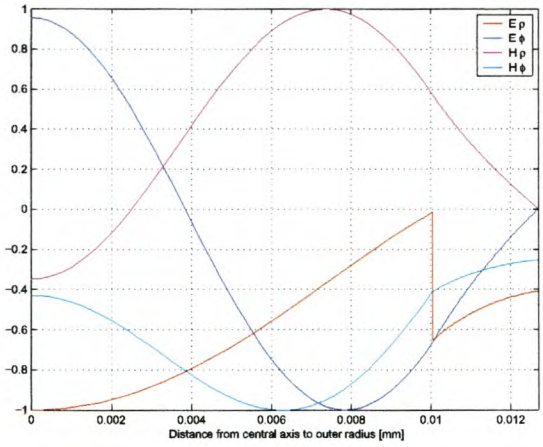


(a) Normalized Field Intensity along the $\rho$ axis for $\phi = 0$

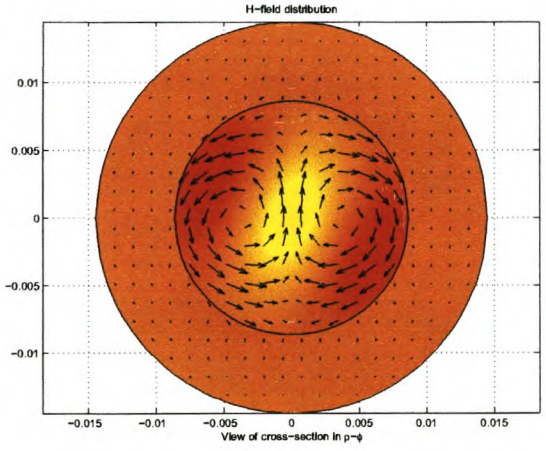


(b) $\rho$-$\phi$ plane Magnetic Field distribution

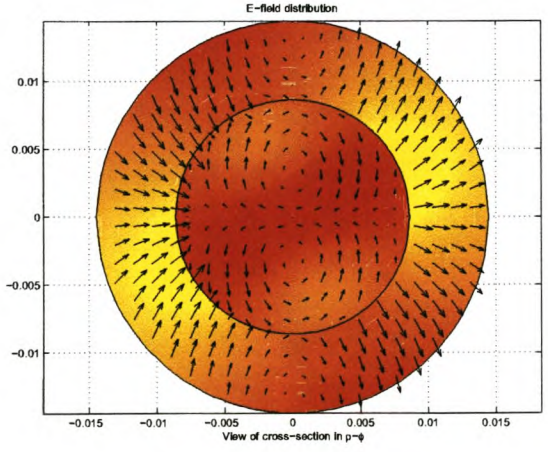


(c) $\rho$-$\phi$ plane Electric Field distribution

**Figure 3.14:** *Normalized Field Distribution of the $HE_{21}$ hybrid mode in an infinite dielectric loaded waveguide*

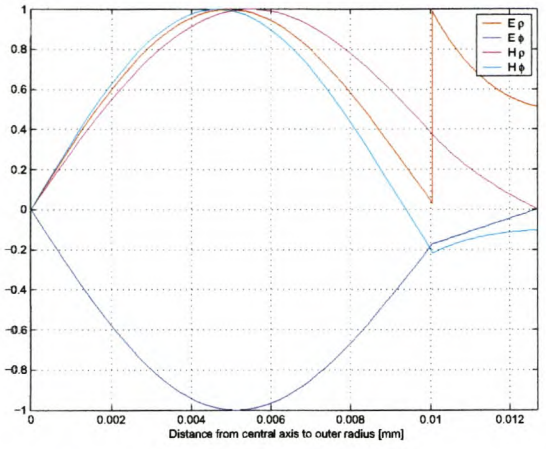


(a) Normalized Field Intensity along the $\rho$ axis for $\phi = 0$

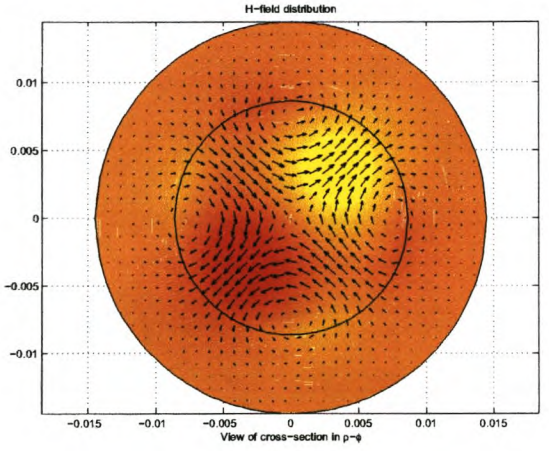


(b) $\rho$-$\phi$ plane Magnetic Field distribution

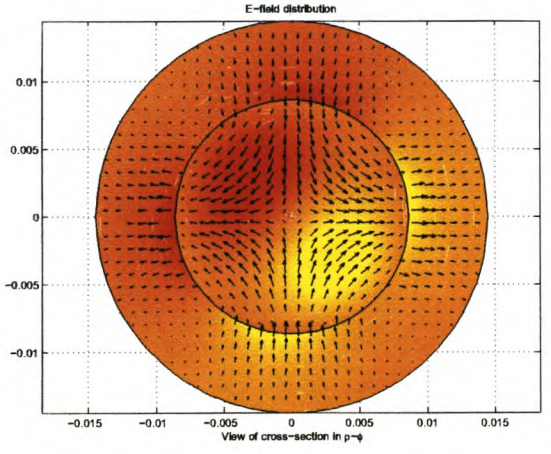


(c) $\rho$-$\phi$ plane Electric Field distribution

**Figure 3.15:** *Normalized Field Distribution of the $HE_{24}$ hybrid mode in an infinite dielectric loaded waveguide*

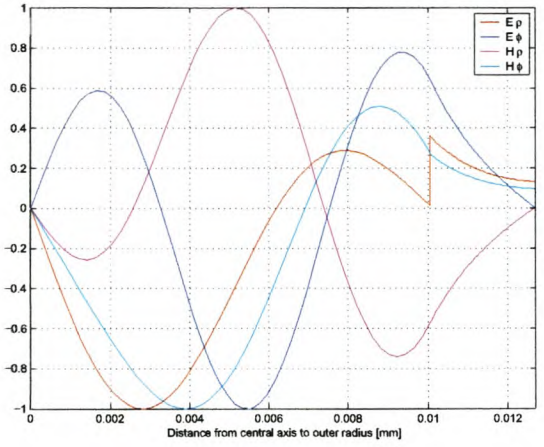


(a) Field Intensity along the $\rho$ axis for $\phi = 0$

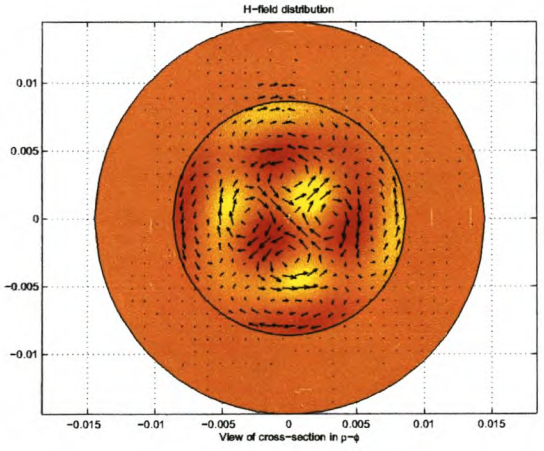


(b) $\rho$-$\phi$ plane Magnetic Field distribution

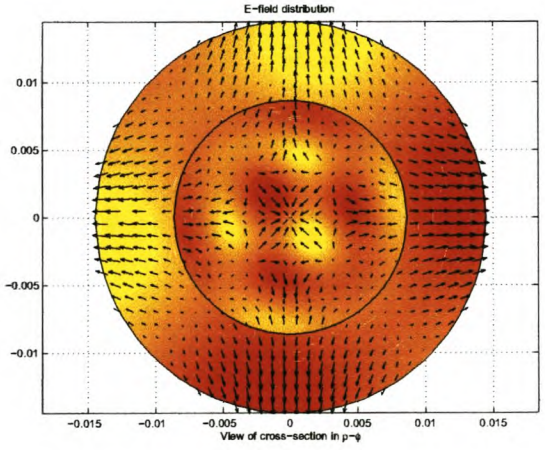


(c) $\rho$-$\phi$ plane Electric Field distribution

### 3.3.3 Theory of Axial Mode Matching

The theory is explained with reference to the structure shown in Figure 3.1. Note that the resonator is surrounded by a cylindrical metallic shield. In this method, the boundaries of interest are at $z = \pm l/2$. Due to symmetry only half of the structure needs to modelled to obtain the correct results. The dielectric resonator and the surrounding air-filled annular region contained between $0 \leq \rho \leq b$ and $0 \leq z \leq l/2$ are modelled as a dielectric loaded radial waveguide, where the permittivity $\epsilon_r$ is independent of the axial co-ordinate $z$. This will be referred to as region A. The second region is contained between $0 \leq \rho \leq b$ and $l/2 \leq z \leq L/2$. This region will be referred to as region B. The transverse fields in each region are expanded in terms of cylindrical waveguide modes and tangential continuity must be enforced at the boundary at $z = l/2$. The equations describing the electric and magnetic fields in the dielectric waveguide are given in Section 3.3.1.

We can express the electric and magnetic fields s linear combinations of eigenmodes. In region A, the electric and magnetic fields are given as

$$\begin{aligned} \overline{E}_A(\rho, \phi, z = l/2) &= \sum_i A_i \hat{\mathrm{e}}_{Ai}(\rho, \phi) f^e_{Ai}(z = l/2) \\ \overline{E}_A(\rho, \phi, z = l/2) &= \sum_i A_i \hat{\mathrm{h}}_{Ai}(\rho, \phi) f^h_{Ai}(z = l/2) \end{aligned} \tag{3.203}$$

where $e_i$ and $h_i$ represent functions that are dependant on $\rho$ and $\phi$. Additionally, $f^e_i$ and $f^h_i$ are functions that are dependant on z. The fields in region B are given by

$$\begin{aligned} \overline{E}_B(\rho, \phi, z = l/2) &= \sum_j B_j \hat{\mathrm{e}}_{Bj}(\rho, \phi) f^e_{Bj}(z = l/2) \\ \overline{E}_B(\rho, \phi, z = l/2) &= \sum_j B_j \hat{\mathrm{h}}_{Bj}(\rho, \phi) f^h_{Bj}(z = l/2) \end{aligned} \tag{3.204}$$

In this particular case the tangential fields must match at the boundary between the two regions. Therefore we know that

$$\overline{E}_A(\rho, \phi, z = l/2) = \overline{E}_B(\rho, \phi, z = l/2) \tag{3.205}$$

$$\overline{H}_A(\rho, \phi, z = l/2) = \overline{H}_B(\rho, \phi, z = l/2) \tag{3.206}$$

Now the cross product of Equation 3.205 with $\hat{\mathrm{h}}_{Ai}$ is taken and the entire equation is integrated over the interface, resulting in the following equation

$$A_i \langle \hat{\mathrm{e}}_{Ai}, \hat{\mathrm{h}}_{Ai} \rangle f^e_{Ai}(l/2) = \sum_j B_j \langle \hat{\mathrm{e}}_{Bj}, \hat{\mathrm{h}}_{Ai} \rangle f^e_{Bj}(l/2) \tag{3.207}$$

where the inner products are defined as

$$\begin{aligned} \langle \hat{\mathrm{e}}_{Ai}, \hat{\mathrm{h}}_{Ai} \rangle &= \int\int_s \hat{\mathrm{e}}_{Ai}(\rho, \phi) \times \hat{\mathrm{h}}_{Ai}(\rho, \phi) \cdot \hat{\mathrm{z}} \; \rho d\rho d\phi \\ \langle \hat{\mathrm{e}}_{Bj}, \hat{\mathrm{h}}_{Ai} \rangle &= \int\int_s \hat{\mathrm{e}}_{Bj}(\rho, \phi) \times \hat{\mathrm{h}}_{Ai}(\rho, \phi) \cdot \hat{\mathrm{z}} \; \rho d\rho d\phi \end{aligned} \tag{3.208}$$

We also made use of the orthogonality property of eigenmodes that

$$\langle \hat{\mathrm{e}}_{Ai}, \hat{\mathrm{h}}_{Aj} \rangle = 0 \text{ for i} \neq j \tag{3.209}$$

Similarly the cross-product of Equation 3.206 is taken with $\hat{\mathrm{e}}_{Ai}$ and integrated over the interface surface, S. This results in the following equation

$$A_i \langle \hat{\mathrm{e}}_{Ai}, \hat{\mathrm{h}}_{Ai} \rangle f^h_{Ai}(l/2) = \sum_j B_j \langle \hat{\mathrm{e}}_{Ai}, \hat{\mathrm{h}}_{Bj} \rangle f^h_{Bj}(l/2) \tag{3.210}$$

If Equation 3.210 is subtracted from Equation 3.207 we can re-write the resulting equation as the following homogenous linear set of equations:

$$\sum_j X_{ij} B_j = 0 \tag{3.211}$$

where

$$X_{ij} = \langle \hat{\mathrm{e}}_{Ai}, \hat{\mathrm{h}}_{Bj} \rangle f^e_{Ai}(l/2) f^h_{Bj}(l/2) - \langle \hat{\mathrm{e}}_{Bj}, \hat{\mathrm{h}}_{Ai} \rangle f^h_{Ai}(l/2) f^e_{Bj}(l/2) \tag{3.212}$$

constitute the coefficients of the linear system. This systems has the following matric form

$$\begin{bmatrix} X_{11} & X_{12} & \dots & X_{1N} \\ X_{21} & X_{22} & \dots & X_{2N} \\ \dots & \dots & \dots & \dots \\ \dots & \dots & \dots & \dots \\ X_{N1} & X_{N2} & \dots & X_{NN} \end{bmatrix} \begin{bmatrix} B1 \\ B2 \\ .. \\ .. \\ B_N \end{bmatrix} = \overline{X} B = 0 \tag{3.213}$$

Once again, the frequencies satisfying the equation

$$\det \overline{X} = 0 \tag{3.214}$$

are the resonant frequencies of the structure. Since axial mode method was not implemented, the exact axial inner products are not provided in this report. For exact descriptions of the inner products, the reader is referred to the article by Chen [32] and his PhD thesis [9].

## 3.4 Conclusion

This chapter outlined the modelling technique that was developed to model inhomogenously filled dielectric cavities (dielectric resonators). First different modelling approaches were discussed and then both radial and axial mode matching were discussed in more detail. This section also introduced the fields in a two-layer stratified waveguide and an infinite dielectric loaded waveguide. The results of the radial mode matching technique were looked at in detail with respect to accuracy and convergence. The next chapter details the proposed design that was obtained in order to implement a high-Q dielectric resonator with an improved SFR

# Chapter 4

# Resonator Design

## 4.1 Introduction

The necessary tools needed to determine the resonant frequencies of dielectric resonators have been developed. At this point, it is possible to generate a design to meet certain requirements. This report focusses on testing whether the proposed structure shown in Figure 4.2 can be used as a high-Q resonator with an improved SFR. In order to obtain a high Q resonator, whispering gallery modes have been proposed. These modes have been shown to have a relatively narrow SFR, and the use of a layered dielectric structure has been proposed to remedy this. A structure consisting of a pill and a ring resonator is proposed that both resonate at the same frequency. This chapter discusses the process followed to come up with a satisfactory design and then evaluates it.

## 4.2 Simple Resonator

In order to have a clear idea of what the SFR of a certain post resonator would look like, all resonant frequencies over a certain frequency band must be determined. As a starting point, the dimensions of the post resonator as examined by Chen [32], are retained. This means that for a resonator as shown in Figure 3.1, a=8.636 mm and l=14.48 mm. The permittivity of the dielectric is taken as $\epsilon_r = 35.74$ In order to prevent the external shield from influencing the resonant frequencies significantly, the length, L, of the shield is chosen to be 35.18 mm and the outer radius, b, is 27.18 mm . For this resonator, the modes that exist between 1 GHz and 12 GHz are provided in Tabel 4.1 where the size of the matrix is chosen to be N=10. Note that at 6.853 GHz a false zero crossing was detected which appeared for all modes with a PMC wall at z=0. That is for TEH, $HEH_{1m}$ etc. This mode was omitted from the table as it does not represent a true resonant frequency. The reason for the occurrence these roots is not known at this stage.

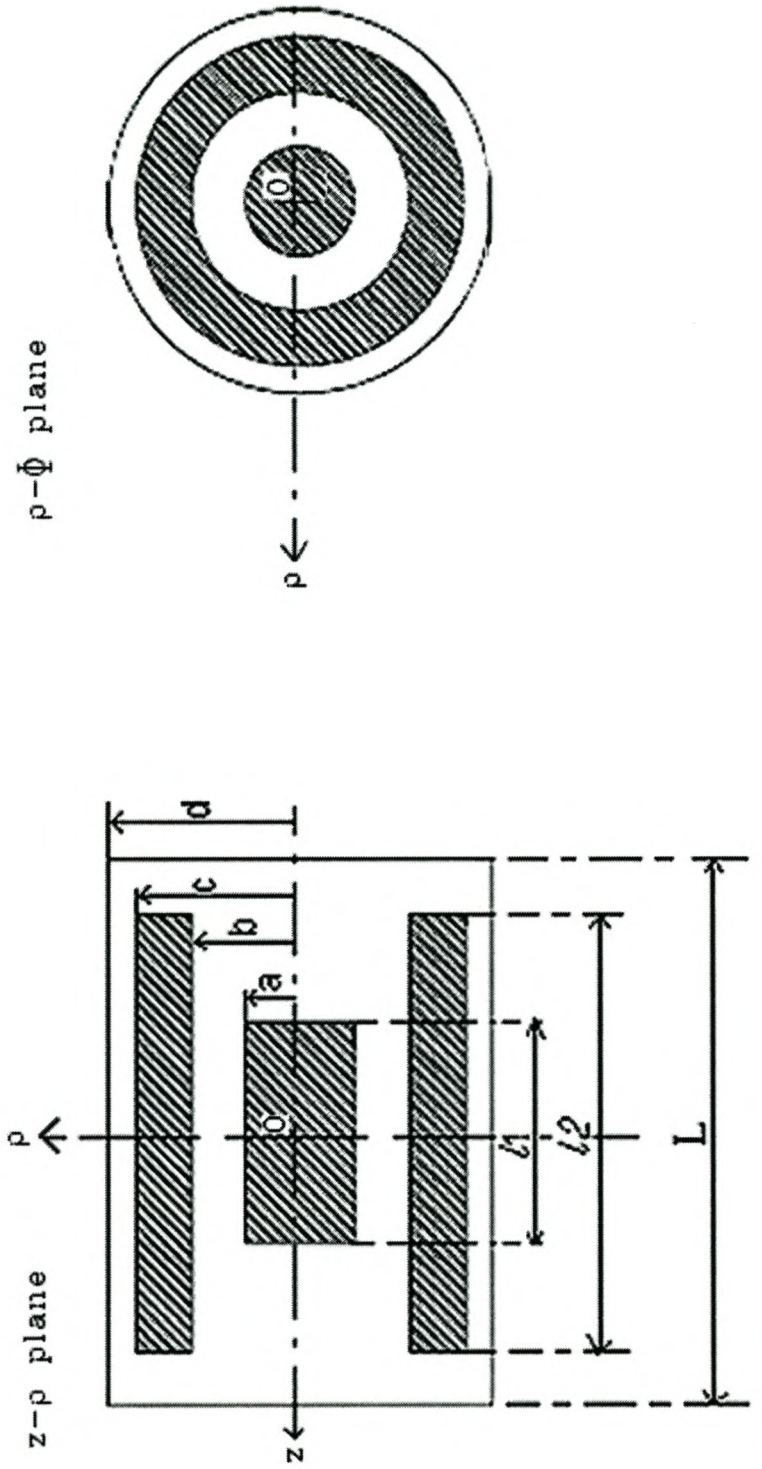


**Figure 4.1:** *The postulated resonating structure.*

**Table 4.1:** *Resonant frequencies [GHz] of a simple post resonator from 1 GHz to 12 GHz [a=8.636 mm, b=27.18 mm, l=14.48 mm L=35.18 mm, $\epsilon_1 = 35.74$ and $\epsilon_2 = 1$]*

| m | 1 | 2 | 3 | 4 | 5 | 6 | 7 | 8 | 9 | 10 | 11 | 12 | 13 |
|---|---|---|---|---|---|---|---|---|---|---|---|---|---|
| $TEE_{0m}$ | 5.206 | 7.443 | 9.829 | 10.617 | 11.209 | | | | | | | | |
| $TEH_{0m}$ | 1.057 | 3.091 | 5.713 | 6.853 | 7.742 | 8.332 | 9.138 | 9.779 | 11.346 | 11.843 | | | |
| $TME_{0m}$ | 3.890 | 4.782 | 7.119 | 8.885 | 9.456 | 9.984 | 10.367 | 11.702 | | | | | |
| $TMH_{0m}$ | 5.903 | 7.329 | 9.143 | 10.404 | 11.397 | | | | | | | | |
| $HEE_{1m}$ | 3.991 | 5.859 | 6.188 | 6.800 | 8.588 | 9.200 | 9.893 | 10.855 | 10.964 | 11.050 | 11.406 | 11.575 | 11.984 |
| $HEE_{2m}$ | 4.849 | 6.921 | 7.276 | 9.030 | 9.536 | 9.794 | 10.078 | | | | | | |
| $HEE_{3m}$ | 5.781 | 7.902 | 8.418 | 10.559 | 10.956 | 11.096 | 11.163 | 11.360 | | | | | |
| $HEE_{4m}$ | 6.748 | 9.564 | 11.410 | 11.833 | | | | | | | | | |
| $HEE_{5m}$ | 7.735 | 9.802 | 10.702 | | | | | | | | | | |
| $HEE_{6m}$ | 8.733 | 10.749 | 11.827 | | | | | | | | | | |
| $HEE_{7m}$ | 9.736 | 11.699 | | | | | | | | | | | |
| $HEE_{8m}$ | 10.741 | | | | | | | | | | | | |
| $HEH_{1m}$ | 4.039 | 4.610 | 6.645 | 7.087 | 7.689 | 8.144 | 8.611 | 9.381 | 10.159 | 10.208 | 10.747 | 11.996 | |
| $HEH_{2m}$ | 5.293 | 6.610 | 7.409 | 8.223 | 8.999 | 9.422 | 9.830 | 10.825 | 11.264 | 11.602 | 11.921 | | |
| $HEH_{3m}$ | 6.387 | 8.107 | 8.448 | 9.392 | 9.879 | 10.342 | 11.907 | | | | | | |
| $HEH_{4m}$ | 7.450 | 8.865 | 10.221 | 10.548 | 10.753 | 11.269 | | | | | | | |
| $HEH_{5m}$ | 8.498 | 9.654 | 11.619 | 11.683 | | | | | | | | | |
| $HEH_{6m}$ | 9.534 | | | | | | | | | | | | |
| $HEH_{7m}$ | 10.562 | 11.336 | | | | | | | | | | | |
| $HEH_{8m}$ | 11.584 | | | | | | | | | | | | |

The next step is to identify a valid whispering gallery mode. It is known that a whispering gallery mode has a high angular variation. The $HEH_{51}$ mode is at a low enough frequency to be convenient for future measurements. It is also desirable since it is the first resonant mode of it's particular hybrid subset. The question now remains whether this mode is a valid hybrid mode or not. Appendix B provides a simple model of whispering gallery modes. The most important properties are the caustic radius, $\rho_c$, the critical radius, $\rho_p$ and the minimum angular variation, $n_{min}$. Whispering gallery modes consist of waves that mainly travel in the angular direction along the radial circumference. The critical radius defines the critical boundary within which the wave travelling in the resonator must be confined in order to be classified as a whispering gallery mode. It is given by

$$\rho_p = a\sqrt{\frac{\epsilon_2}{\epsilon_1}} \tag{4.1}$$

where a is the radius of the dielectric cylinder, $\epsilon_2$ is the permittivity of the outer region surrounding the dielectric, and $\epsilon_1$ is the permittivity of the inner dielectric material. The caustic radius is the actual boundary within which the waves are confined It is given as

$$\rho_c = \frac{n}{\sqrt{(\epsilon_1\epsilon_0\mu_0)}2\pi f} = \frac{n}{\beta_1} \tag{4.2}$$

Therefore a condition that follows is that

$$a > \rho_c > \rho_p \tag{4.3}$$

We can find $n_{min}$ by setting the caustic radius equal to the critical radius which gives us

$$n_{min} = \beta_1\ a\sqrt{\frac{\epsilon_2}{\epsilon_1}} \tag{4.4}$$

In order to gain an insight into the field distribution of this proposed mode, the $HEH_{51}$ is examined in the dielectric loaded waveguide. Using radial mode matching, the resonant frequency is determined as 8.498 GHz. Solving for the axial propagation constant in the dielectric loaded waveguide, it is given as $\beta_1 = 1.238^3$ and $\rho_c = 4.04$ mm. The critical radius of a dielectric loaded waveguide with radius $a = 8.636$ mm is $\rho_p = 1.445$ mm and the minimum angular variation $n_{min} = 2$. We can also prove that Equation 4.3 holds true. This means that the $HEH_{51}$ mode complies with the requirements of whispering gallery modes. It must be noted that an angular variation of $n = 5$ is still at the low spectrum of whispering gallery mode angular variations. These modes have been implemented with $n > 25$! As the angular variation increases, the radiation becomes more and more confined and the Q factor increases. The resonances with higher angular variations will obviously occur at higher frequencies and should be more difficult to measure when implemented. This is the main reason for choosing a mode with a relatively low angular variation. Figure 4.3 (a) shows the magnetic and Figure 4.3 (b) shows the electric field distributions of the $HE_{51}$ mode in the dielectric loaded resonator. Figure 4.3 (c) shows a close-up of a quarter of the dielectric resonator, showing the magnetic fields. One can confirm from this figure that the calculation of $\rho_c = 4.04$ mm is quite accurate. Note that the fields that

are plotted are the accurate fields as determined for dielectric loaded waveguides. The model for whispering gallery waveguides from which the equation for the caustic radius is derived is an approximation. Using the insight gained from the dielectric loaded waveguide implementation it was assumed that the $HEH_{51}$ mode is indeed a whispering gallery mode in the dielectric loaded resonator.

**Table 4.2:** *The resonant frequencies of the post resonator over a frequency range from 8.2 GIIz to 8.6 GIIz*

| Mode | Frequency [GIIz] |
|---|---|
| $HEH_{24}$ | 8.223 |
| $TEH_{04}$ | 8.332 |
| $HEE_{33}$ | 8.418 |
| $HEH_{33}$ | 8.448 |
| $HEH_{51}$ | 8.498 |
| $HEE_{15}$ | 8.588 |

The frequency spectrum from 8.2 GIIz to 8.6 GIIz the simple dielectric resonator, is shown in Figure 4.2. The order of these modes from the lowest frequency point to the highest frequency point is listed in Table 4.2. The SFR can be seen to be only (8.498 - 8.448)/8.498 $-$ 0.59%.

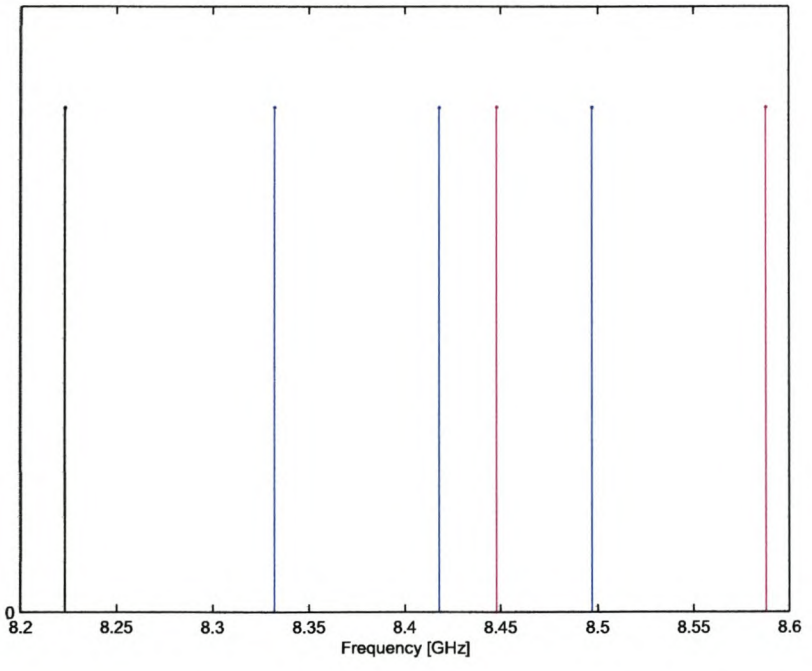


**Figure 4.2:** *The mode chart of the single post resonator for a frequency range from 8.2 GIIz to 8.6 GIIz*

**Figure 4.3:** *Field Distribution of the $HE_{51}$ hybrid mode in an infinite dielectric loaded waveguide*

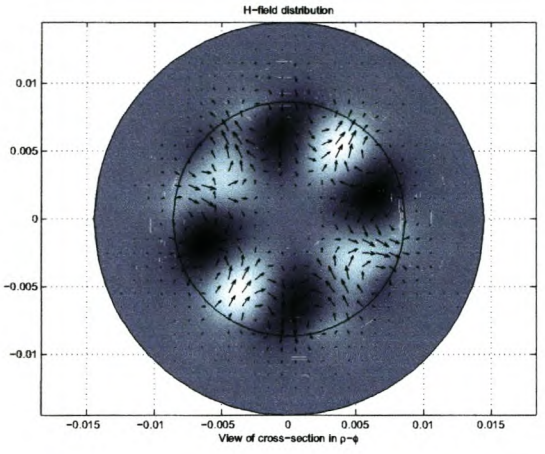


(a) $\rho$-$\phi$ plane Magnetic Field distribution

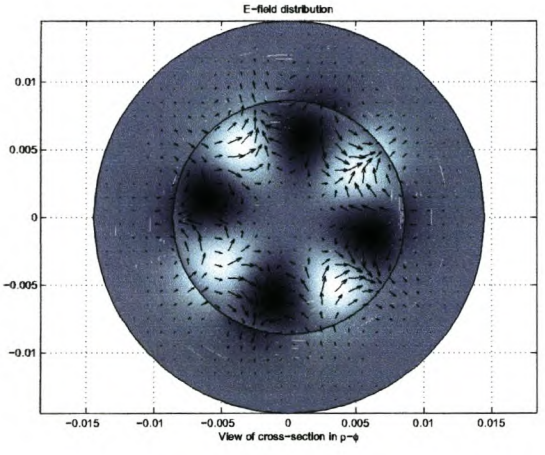


(b) $\rho$-$\phi$ plane Electric Field distribution

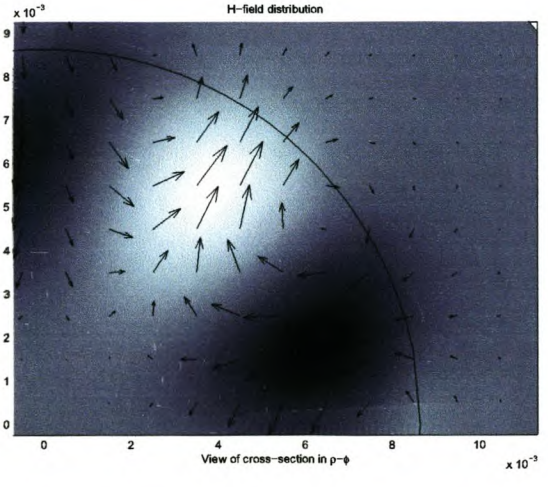


(c) Zoomed view of Figure 4.3(a)

## 4.3 Ring Resonator

The next step in the design is to find a ring resonator that will have a $HEH_{51}$ mode resonating at the same frequency as the post resonator. One can change the resonant frequency by either changing the height of the ring resonator, or by changing the inner and outer radii. Changing the radii has certain problems as the inner radius has to be larger than the radius of the post resonator. As the inner radius increases (with a corresponding increase of the outer radius), the resonant frequency becomes lower. In the implementation, it was found that it was impossible to obtain a high enough frequency to obtain a satisfactory result. Additionally, moving the resonator too close to the boundary causes the boundary to have significant effects on the resonant frequency. The conduction losses also should increase, resulting in a lowered Q factor. Therefore fixed radii were arbitrarily chosen to be a=11.43 mm and b=16.51 mm and the frequency was changed by changing the height of the resonator. The shield dimensions were set to be the same as those defined for the post resonator. The length, L, of the shield was to be 35.18 mm and the outer radius, b, was 27.18 mm . Figure 4.4 shows the effect that changing the ring height has on the resonant frequency of the $HEH_{51}$ mode. One can determine that a ring height of 2.013 mm would produce a ring resonator with the same resonant frequency as that of the post resonator analyzed previously. The resonant frequencies of this ring resonator are shown in Table 4.3 for frequencies between 1 GHz and 12 GHz. Note that at 1.944 GHz a false zero crossing was again detect for all modes with a PMC wall at z=0.

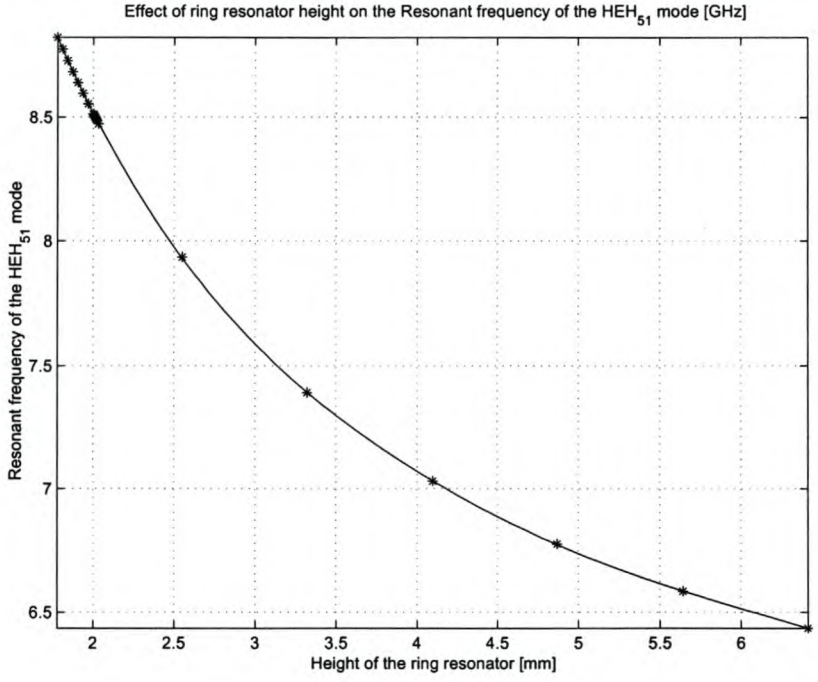


**Figure 4.4:** *The effect of changing the ring height on the resonant frequency of the $HEH_{51}$ mode [a = 11.43 mm, b=16.51 mm, c=27.18 mm and L=35.18 mm,]*

**Table 4.3:** *Resonant frequencies [GHz] of a ring resonator from 1 GHz to 12 GHz [ a = 11.43 mm, b=16.51 mm, c=27.18 mm, l=2.013 mm and L=35.18 mm]*

| m | 1 | 2 | 3 | 4 |
|---|---|---|---|---|
| $TEE_{0m}$ | 10.568 | | | |
| $TEH_{0m}$ | 1.944 | 4.053 | 8.448 | 10.349 |
| $TME_{0m}$ | 4.168 | 9.264 | 9.597 | |
| $TMH_{0m}$ | 5.843 | 10.462 | | |
| $HEE_{1m}$ | 6.608 | 8.908 | 10.516 | 11.843 |
| $HEE_{2m}$ | 8.822 | 9.865 | 11.766 | |
| $HEE_{3m}$ | 10.815 | 11.114 | | |
| $HEH_{1m}$ | 4.270 | 6.738 | 8.000 | 11.464 |
| $HEH_{2m}$ | 5.914 | 8.036 | 9.248 | 10.617 |
| $HEH_{3m}$ | 7.573 | 8.485 | 11.066 | |
| $HEH_{4m}$ | 8.227 | 9.901 | | |
| $HEH_{5m}$ | 8.498 | 11.691 | | |
| $HEH_{6m}$ | 9.534 | | | |
| $HEH_{8m}$ | 9.421 | | | |

The frequency spectrum from 8.2 GIIz to 8.6 GIIz for the ring resonator is shown in Figure 4.5. The order of these modes from the lowest frequency point to the highest frequency point is listed in Table 4.4.

**Table 4.4:** *The resonant frequencies of the ring resonator over a frequency range from 8.2 GIIz to 8.6 GIIz*

| Mode | Frequency [GIIz] |
|---|---|
| $HEH_{41}$ | 8.227 |
| $TEH_{02}$ | 8.448 |
| $HEE_{32}$ | 8.485 |
| $HEH_{51}$ | 8.498 |

The SFR in this case is (8.498 - 8.485)/8.498 − 0.15%. One can see that although the overall amount of modes in the region being considered has decreased, the SFR of the $HEH_{51}$ mode has not been improved. This is not a desirable result, and an effort should be made in future iterations of this design to find a hybrid mode that has an improved SFR for the ring resonator.

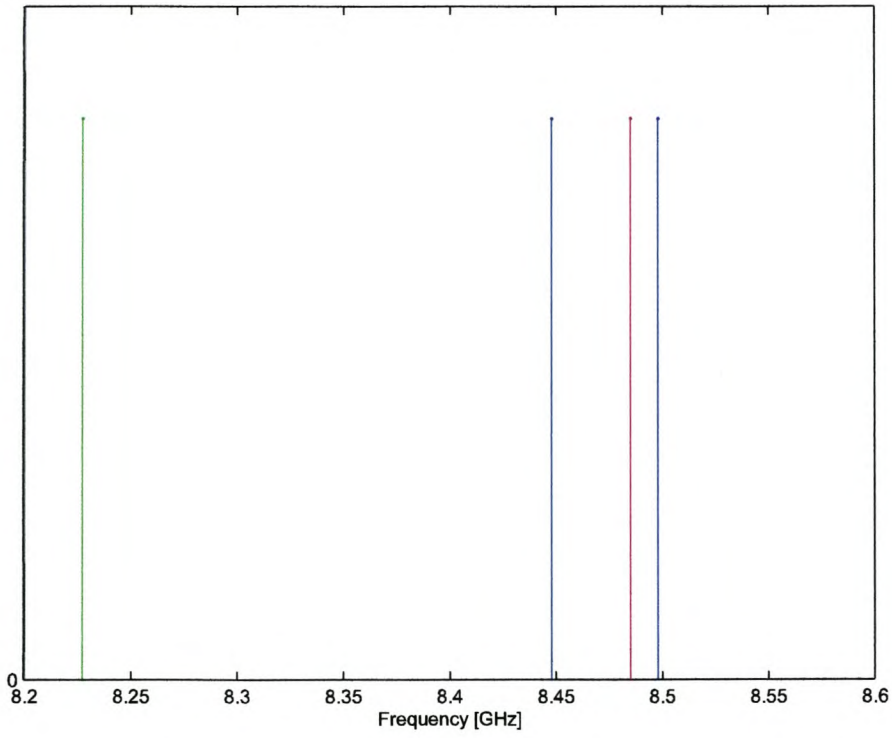


**Figure 4.5:** *The mode chart of the ring resonator for a frequency range from 8.2 GIIz to 8.6 GIIz*

## 4.4 Combined Structure

Finally, the resonator consisting of the post and the ring resonator was modelled. Table 4.5 shows the first two resonant frequencies of the TE and TM modes. It is clear that the modes of the combined structure consist of an overlap of the frequencies of the individual resonators.

**Table 4.5:** *The first two Resonant frequencies [GIIz] for the TE and TM modes of the combined resonator*

| m | 1 | 2 |
|---|---|---|
| $TEE_{0m}$ | 5.1990 | 7.4290 |
| $TEH_{0m}$ | 2.9478 | 4.4001 |
| $TME_{0m}$ | 3.8522 | 4.7723 |
| $TMH_{0m}$ | 5.7670 | 7.326 |

Due to time constraints, only the specific frequency band from 8.2 to 8.6 GIIz was considered for the hybrid modes. Therefore it is not possible to group the modes according to what point they occur in the frequency domain. The modes are described in the same manner as before where m is designated as x to indicate this uncertainty. Figure 4.6 shows the resulting mode chart over the specific frequency band. The order of these modes is $HEH_{4x}$, $HEH_{2x}$, $TEH_{0x}$, $HEH_{3x}$, $HEH_{5x}$, $HEH_{5x}$, and $HEE_{1x}$.

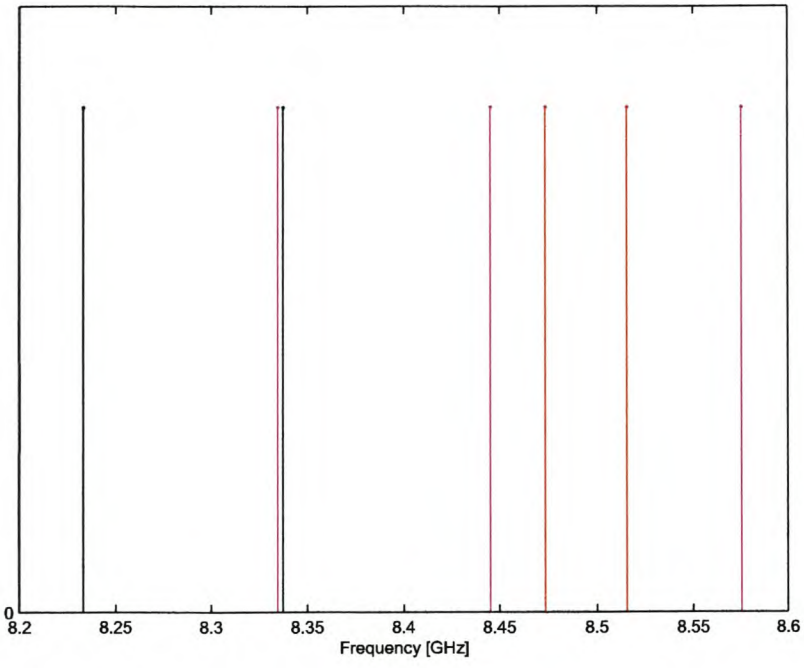


**Figure 4.6:** *The mode chart of the combined resonator for a frequency range from 8.2 GIIz to 8.6 GIIz*

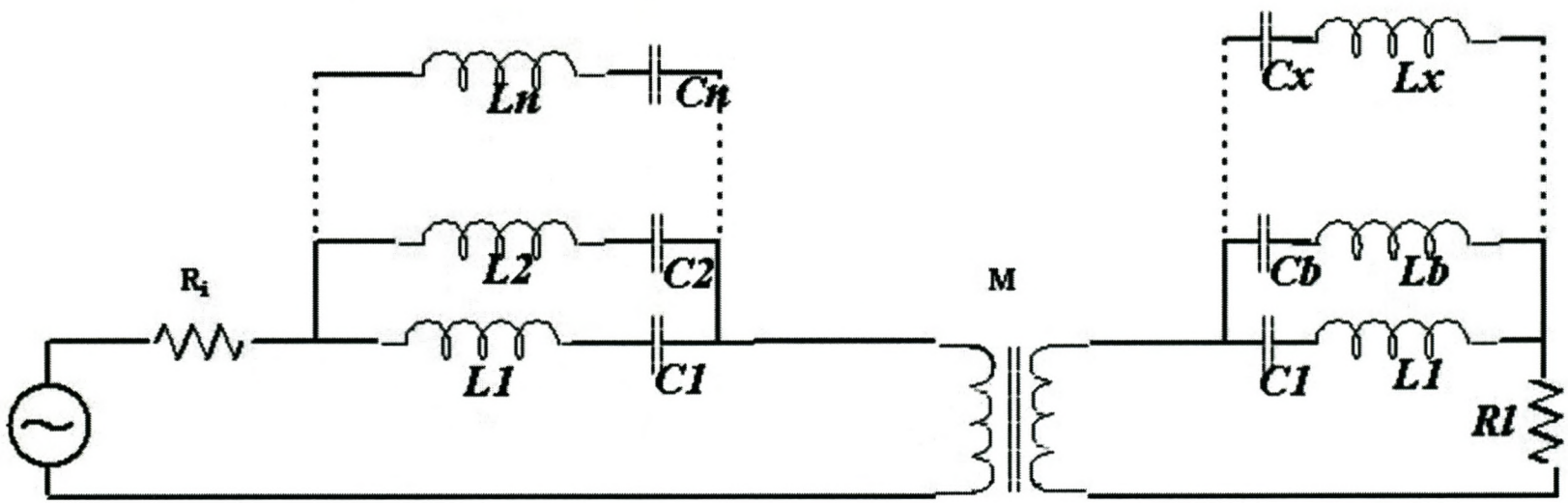


**Figure 4.7:** *Equivalent circuit diagram of the postulated resonating structure.*

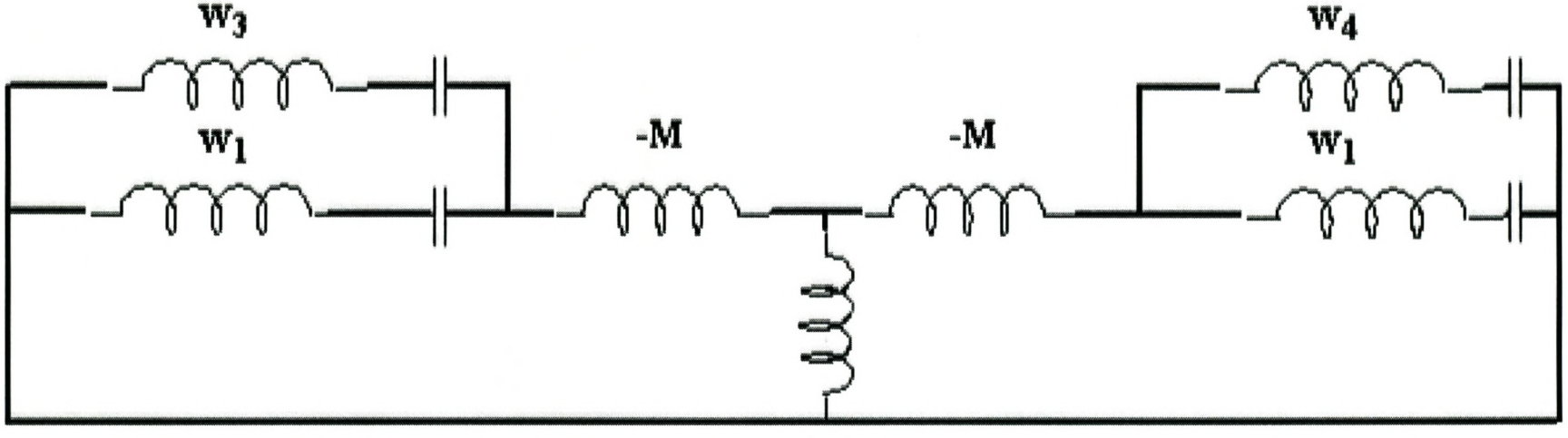


**Figure 4.8:** *Simplified Equivalent circuit diagram of the postulated resonating structure showing short circuited source and load as implemented by the mode matching technique.*

Once again, the frequency band consists of an overlap of the individual resonant frequency responses in addition to a double resonance around the design frequency. This double resonance is due to the coupling between the two resonators. This can be explained with reference to the equivalent circuit diagram of the proposed structure shown in Figure 4.4.

Since I am not taking the source and the load into account in my mode matching technique, one can apply a short circuit across the source and source resistance and across the load resistance. This is seen in Figure 4.4. Here only two resonances of each resonator are indicated for simplicity. The resonance $\omega_1 = 1/\sqrt{L_1 C_1}$ is set to be common to both resonators. Mesh current analysis can now be applied to the circuit and a linear homogenous system of equations in terms of the individual impedances and the currents can be set up. Finally, writing this system in matrix form will result in an equation of the shape

$$[Z]\,[I] = [0] \tag{4.5}$$

where [Z] is a square matrix and [I] is a vector matrix. The non-trivial solutions of the system are once again given by the zero points of the determinant of [Z].

When implementing this figure in Matlab, I defined three resonance, $\omega_1, \omega_2$ and $\omega_3$ where $\omega_i = 1/\sqrt{L_i C_i}$. In this case $\omega_1$ was set to be common to both resonators. The ideal transformer was modelled as a T-network as indicated on the figure where M represents the coupling between the two resonating structures. I arbitrarily chose the following resonant frequencies:

**Table 4.6:** *Different resonant frequencies assigned to the resonances of Figure 4.4*

| Resonance | GHz |
|---|---|
| $\omega_1$ | 5 |
| $\omega_2$ | 2 |
| $\omega_3$ | 9 |

The derived resonant frequencies for these resonances, where the coupling M is set to be $0.1\mu H$ are shown in Figure 4.9. One can also clearly see the double resonance that occurs around $\omega_1$. The effect of changing the coupling, M, is investigated in Figure 4.10 for two different coupling factors. One can clearly see the great effect that the coupling between the resonators has on the double resonance.

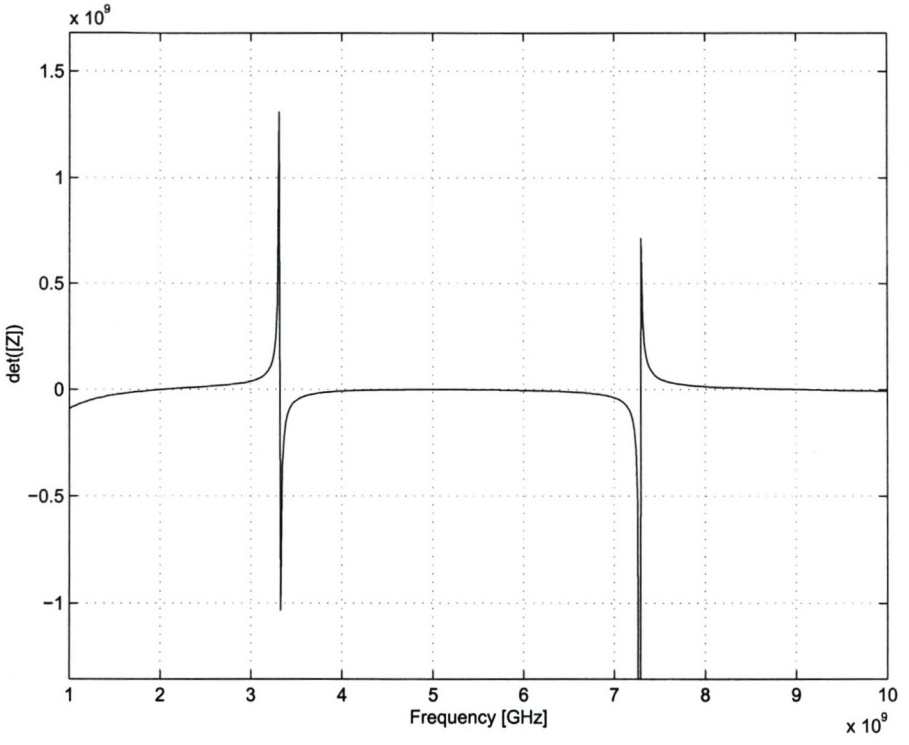


**Figure 4.9:** *The resonant frequencies of the examined resonant circuit.*

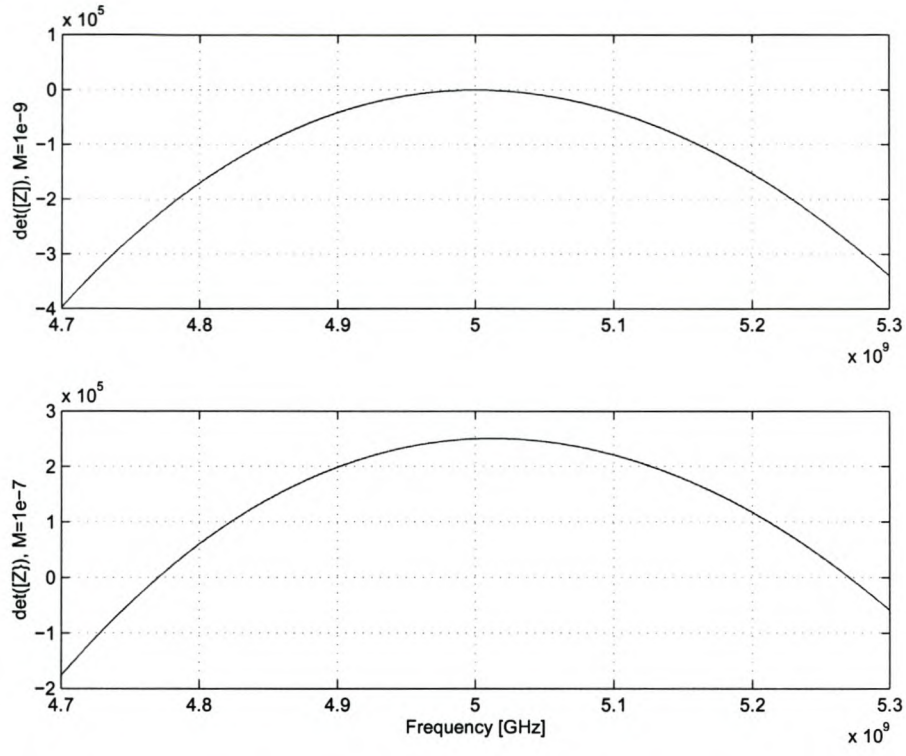


**Figure 4.10:** *The double resonance around the resonant frequency common to both resonators for two different coupling factors, M*

By using the mode matching technique, an accurate equivalent circuit model can therefore be determined. This analysis phase can be combined with optimization algorithms to to design coupled resonators with specific characteristics. This prototype will serve as a starting point for an optimization phase. However, it can be already be seen for the first prototype that the choice of dimensions can be more carefully chosen to improve the coupled structure's SFR.

## 4.5 Conclusion

This chapter details a design consisting of a post and a ring resonator. Both the post and ring resonator were designed to resonate at the same frequency for a chosen whispering gallery mode. The intention was to design a first-order prototype of a combined resonator with an improved SFR as compared to the simple structure.

# Chapter 5

# Conclusion

Starting from basic principles, the theory of radial and axial mode matching was discussed in detail and then applied to a structure with two to three radial boundaries. Post resonators, ring resonators and combinations of the two were implemented, and their resonant frequencies derived. The results were compared to results provided by Chen [32], [9] and were found with an accuracy of better than 1% for the TE and TM modes, and better than 3 % for the hybrid modes. It is also very easy to expand the mode matching method to model a general structure with more than three radial boundaries.

Following this, a design consisting of a post resonator and a ring resonator was investigated. A hybrid mode of the post resonator was chosen and the ring resonator was designed to resonate at the same frequency in an attempt to improve the SFR of the post resonator. The mode matching technique simply provides a list of all possible resonant frequencies that can occur over that frequency range. A final step that is necessary to design a whispering gallery mode resonator, is to take into account the coupling between the two resonators and the coupling between the individual resonators and the external source.

This research has provided the basic analysis tools necessary in resonator designs, but further steps are necessary if a practical design is to be implemented. Several additional refinements to the mode matching implementation are possible:

One critical aspect of resonators, the temperature stability, has not been included in the model. This should really be considered if a commercial resonator is to be built. Also of interest is the implementation of mode matching that can be applied to resonators made from anisotropic materials such as sapphire. These types of resonators have become increasingly popular due to their very high Q factor. Finally, if the resonator is to be built it has to be excited by some type of source, whose effect should be considered

Concerning the present implementation, several criticisms can be made. For one, the run-time is rather long. Although careful attention to streamlining the Matlab code for maximum efficiency could improve this aspect a little, most of this time is spent finding the propagation constants

of the TE and TM modes in each region. Since it is necessary to find all the modes, and since the omission of a single root results in extremely incorrect results, the search algorithm stepped through the respective function at very small intervals. Not much time was spent on determining the best search method for the job, and an improvement seems probable. Additionally, the determinant seems to have several false zero crossings that show up as resonant frequencies for several modes. The origin of these false zero crossings was not yet been determined.

It would be of interest to actually build the structure and take measurements. This report has been theoretical of nature, but has hopefully laid the foundations for future practical investigations into dielectric resonators. Due to time limitations, whispering gallery modes did not achieve as much attentions as they deserve, but it is to be hoped that the work done in this project will be used in the investigation and implementation of dielectric whispering gallery resonators.

# Bibliography

[1] ANNINO, G., CASSETARI, M., and MARTINELLI, M., "Study on Planar Whispering Gallery Dielectric Resonators. II. a multiple band device." World Wide Web, `http://arxiv.org/pdf/physics/0203010`, 2002.

[2] ANNINO, G., CASSETARI, M., and MARTINELLI, M., "Study on Planar Whispering Gallery Dielectric Resonators. I. General Properties." World Wide Web, `http://arxiv.org/pdf/physics/0203009`, 2002.

[3] ANNINO, G., CASSETTARI, M., LONGO, I., and MERTINELLI, M., "Whispering Gallery Modes in a Dielectric Resonator: Characterisation at Millimetre Wavelength." *IEEE Transactions on Microwave Theory and Techniques*, November 1997, Vol. 45, No. 11, pp. 2025–2034.

[4] BLADEL, J. V., "High-Permittivity Dielectrics in Waveguides and Resonators." *IEEE Transactions on Microwave Theory and Techniques*, January 1974, Vol. MTT-22, No. 1, pp. 32–37.

[5] BLADEL, J. V., "The Excitation od Dielectric Resonators of Very High Permittivity." *IEEE Transactions on Microwave Theory and Techniques*, February 1975, Vol. MTT-23, No. 2, pp. 198–217.

[6] BLADEL, J. V., "High-Permittivity Dielectrics in Waveguides and Resonators." *IEEE Transactions on Microwave Theory and Techniques*, February 1975, Vol. MTT-23, No. 2, pp. 199–207.

[7] CHEN, C. and ZAKI, K. A., "Intensity and Distribution of Hybrid Mode Fields in Dielectric-Loaded Waveguides." *IEEE Transactions on Microwave Theory and Techniques*, December 1985, Vol. 33, No. 12, pp. 1442–1447.

[8] CHEN, C. and ZAKI, K. A., "Resonant Frequency of Dielectric Resonators Containing Complex Modes." *IEEE Transactions on Microwave Theory and Techniques*, October 1988, Vol. 36, No. 10, pp. 1455–1457.

[9] CHEN, S.-W., *Analysis and Modelling of Dielectric Loaded Resonators, Filters and Periodic Structure*. PhD thesis, University of Maryland, 1990.

[10] COHN, S. B., "Microwave Bandpass Filters containing High-Q Dielectric Resonators." *IEEE Transactions on Microwave Theory and Techniques*, April 1968, Vol. 16, No. 4, p. 227.

[11] E.R.NAGELBERY and J.M.HOFFSPIEGEL, "Computer-graphic analysis of dielectric waveguides." *IEEE Trans.Microwave Theory.Tech.*, March 1967, Vol. MTT-15, pp. 187–189.

[12] HAN, Q., KOGAMI, Y., TOMABECHI, Y., and MATSUMURA, K., "Resonance Characteristics of a Coupled Dielectric Resonator which consists of a Dielectric Disk Resonator and a Ring Resonator.." *IEICE Trans.Electron.*, February 1997, Vol. E80-C, No. 2, pp. 327–333.

[13] HARRINGTON, R. F., *Time Harmonic Electromagnetic Fields*. McGraw-Hill, Inc., 1961.

[14] ITOH, T. and RUDOKAS, R. S., "New methods for computing the resonant frequencies of Dielectric Resonators." *IEEE Trans. Microwave Theory Tech.*, January 1977, Vol. MTT-25, pp. 52–54.

[15] JI, Y., YAO, X. S., and MALEKI, L., "A High-Q Millimetre-Wave Dielectric Resonator Bandpass Filter Using Whispering Gallery Modes." *TMO Progress Report*, May 2000, Vol. 42, No. 141, p. 111.

[16] KAJFEZ, D. and GUILLON, P. (Eds), *Dielectric Resonators*. second edition. Noble Publishing Corporation, 1998.

[17] KONISHI, Y., "Novel Dielectric Waveguide Components-Microwave Applications of New Ceramic Materials." *Proceedings of the IEEE*, June 1991, Vol. 79, No. 6, pp. 725–740.

[18] LEHMENSIEK, R. and MEYER, P., "Creating Accurate multivariate rational interpolation models of microwave circuits by using efficient adaptive sampling to minimize the number of computational electromagnetic analyses." *IEEE Transactions on Microwave Theory and Techniques*, August 2001, Vol. 49, No. 8, pp. 1419–1430.

[19] MASSE, D. J., "A new low-loss high-k temperature compensated dielectric for microwave applications." *Proc. IEEE*, November 1971, Vol. 59, pp. 1628–1629.

[20] NILSSON, J. W. and RIEDEL, S. A., *Electric Circuits*. fifth edition. Addison-Wesley Publishing Company, 1996.

[21] OKAYA, A., "The Rutile microwave resonator." *Proc. IRE*, November 1960, Vol. 48, p. 921.

[22] OKAYA, A. and BARASH, L. F., "The dielectric microwave resonator." *Proc. IRE*, October 1962, Vol. 50, pp. 2081–2092.

[23] PENG, H., "Study of Whispering Gallery Modes in Double Disk Sapphire Resonators." *IEEE Transactions on Microwave Theory and Techniques*, June 1996, Vol. 44, No. 6, pp. 848–853.

[24] PLOURDE, J. K., LINN, D. F., H.M. O'BRIEN, J., and J. THOMPSON, J., "$Ba_2Ti_9O_20$ as a microwave dielectric resonator." *J. Amer. Ceram. Soc.*, October/November 1975, Vol. 58, pp. 418–420.

[25] POZAR, D. M., *Microwave Engineering*. second edition. John Wiley & Sons, Inc., 1998.

[26] RICHTMEYER, R. D., "Dielectric Resonator." *J. Appl. Phys.*, June 1939, Vol. 10, pp. 391–398.

[27] SOUTHWORTH, G. C., *Forty Years of Radio Research*. Gordon and Breach, 1962.

[28] STRATTON, J. A., *Electromagnetic theory*. McGraw-Hill, 1941.

[29] VEDRENNE, C. and ARNAUD, J., "Whispering Gallery Modes of Dielectric Resonators." *Proc.Inst.Elec.Eng.*, August 1982, Vol. 129, No. H, pp. 183–187.

[30] WANG, C. and ZAKI, K. A., "Generalized Multiplayer Anisotropic Dielectric Resonators." *IEEE Transactions on Microwave Theory and Techniques*, January 2000, Vol. 48, No. 1, pp. 60–66.

[31] WEINSTEIN, L. V., *Open Resonators and Open Waveguides*. Golem, 1969.

[32] ZAKI, K. A. and CHEN, C., "New Results in Dielectric Loaded Resonators." *IEEE Transactions on Microwave Theory and Techniques*, July 1986, Vol. 34, No. 7, pp. 815–824.

# Appendix A

# Quality Factor

This Appendix demonstrates several important characteristics of the quality factor of resonant circuits. The performance of any resonator, be it a dielectric resonator or a lumped circuit resonator, can be characterized by it's quality factor (Q). This parameter is defined as [25]

$$Q = \omega_0 \frac{(\text{average energy stored})}{(\text{energy loss/second})} = \omega_0 \frac{W_m + W_e}{P_l} \tag{A.1}$$

where $\omega_0 = 2\pi f_0$ is the resonant radian frequency. $W_m$ is defined as the average stored magnetic energy at resonance, $W_e$ as the average stored electric energy at resonance and $P_l$ as the power lost in the resonator at the resonant frequency, $f_0$. At a given resonant frequency, the total energy is stored in equal amounts as electric and magnetic energy. This means that the input impedance is purely real. As soon as the structure is excited somewhere off-resonance, the energies in the electric and magnetic fields do not balance and the extra energy needs to be given back to the source. This means that the transmission line acts as a reactive load on the exciting source in addition to a resistance due to loss. The following theory develops a relationship between a resonator's quality factor and its bandwidth. After this, the quality factors due to individual power losses in the resonator structure are investigated.

## A.1 Quality factor relationship to bandwidth

The Q factor can be examined by investigating the behavior of a simple resonant circuit. Consider the simple parallel RLC circuit as shown in Figure A.1. Assume that the switch is opened at $t = 0$. By summing the currents at the top node, in the circuit, the following equation can be generated:

$$\frac{v(t)}{R} + \frac{1}{L}\int_o^t v(x)dx + C\frac{dv(t)}{dt} = I_{dc}u(t) \tag{A.2}$$

We know from Nilsson [20], that the resonant frequency of this circuit is $w_o = \frac{1}{\sqrt{LC}}$ and the neper frequency is $\sigma = \frac{1}{2RC}$. Therefore, by differentiating the equation with time and

substituting $w_o$ and $\sigma$, we can derive the following differential equation [16]:

$$\frac{d^2v}{dt^2} + 2\sigma\frac{dv}{dt} + \omega_o^2 v = f(t) \tag{A.3}$$

This equation can also be obtained by proper manipulation of Maxwell's equations [16].

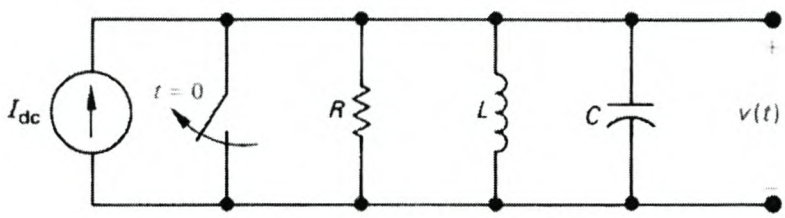


**Figure A.1:** *Discrete components resonator showing symbols used in setting up FT equation [16]*

When $\sigma = 0$ in this equation, the homogenous solution is

$$v(t) = A\sin\omega_o t + B\cos\omega_o t \tag{A.4}$$

If $\sigma > 0$, this implies that the resonator has losses. The equation can now be Laplace transformed and one can solve for the transfer function as follows:

$$T(s) = \frac{V(s)}{F(s)} = \frac{1}{s^2 + 2\sigma s + \omega_o^2} \tag{A.5}$$

The denominator can be factored to give

$$T(s) = \frac{1}{2\omega_l}\left\{\frac{1}{s + \sigma + \jmath\omega_l} - \frac{1}{s + \sigma - \jmath\omega_l}\right\} \tag{A.6}$$

where the loaded natural frequency is defined as $w_l = \sqrt{\omega_o^2 - \sigma^2}$. This shows the presence of loss in the resonator and $\sigma > 0$ results in a change in resonance frequency. This is also known as frequency pulling due to loss. The natural response of the differential equation is [16]

$$v(t) = Ve^{-\sigma t}\sin\omega_l t \tag{A.7}$$

The stored energy is proportional to the average value of $v^2(t)$ and can be written as

$$W = \frac{1}{2}V^2 e^{-2\sigma t} \tag{A.8}$$

for small values of $\sigma$. The average power of the system is therefore given as

$$P = -\frac{dW}{dt} = 2\sigma W \tag{A.9}$$

This gives us

$$\sigma = \frac{P}{2W} \tag{A.10}$$

and we can rewrite the quality factor as

$$Q = \frac{\omega_o}{2\sigma} \tag{A.11}$$

We can now define the loaded natural resonant frequency as

$$\omega_l = \omega_0 \sqrt{1 - \frac{1}{4Q^2}} \tag{A.12}$$

and by substituting Equation A.11 into the differential equation one obtains

$$\frac{d^2v}{dt^2} + \frac{\omega_0}{Q}\frac{dv}{dt} + \omega_0^2 v = f(t) \tag{A.13}$$

For $s = \jmath\omega$ and $\sigma = \omega_0/(2Q)$ the transfer function $T(s)$ becomes

$$T(\jmath\omega) = \frac{V(\jmath\omega)}{F(\jmath\omega)} = \frac{1}{\omega_0^2 - \omega^2 + \jmath\omega_0/Q} \tag{A.14}$$

The denominator can now be rewritten as

$$\omega_0^2 - \omega^2 + \jmath\omega\frac{\omega_0}{Q} = \jmath\omega\omega_0 Q\left\{1 + \jmath Q\left[\frac{\omega}{\omega_0} - \frac{\omega_o}{\omega}\right]\right\} \tag{A.15}$$

Now the $\omega$ dependance can be factored out giving

$$\frac{\omega}{\omega_0} - \frac{\omega_0}{\omega} = \left[\frac{\omega - \omega_0}{\omega_0}\right]\left[\frac{\omega_0}{\omega} + 1\right] \tag{A.16}$$

Assuming a high quality factor, $\omega$ is very close to $\omega_0$ which means that $\omega_0/\omega + 1 \simeq 2$. We can now write the $\omega$ dependance as

$$\frac{\omega}{\omega_0} - \frac{\omega_0}{\omega} = 2\left[\frac{\omega - \omega_0}{\omega_0}\right] = 2\delta \tag{A.17}$$

where $\delta = (\omega - \omega_0)/\omega_0$ is defined as the frequency tuning parameter. We can now define an approximate transfer function

$$T(\jmath\omega) = \frac{\jmath Q/\omega\omega_0}{1 + \jmath Q\delta} \tag{A.18}$$

The magnitude of this approximate transfer function is a bell-shaped curve which is highly dependant on Q. At this point, the half-power bandwidth, B, is defined. B is equal to the frequency range $\triangle\omega$ from the half-power frequencies $\omega_1$ and $\omega_2$ that are found where

$$\mid T(\omega) \mid = \frac{1}{\sqrt{2}} \mid T(\omega_0) \mid \tag{A.19}$$

By using the approximate transfer function, it is possible to rewrite the above equation as

$$\frac{Q/(\omega\omega_0)}{\sqrt{1 + 4Q^2\delta^2}} = \frac{1}{\sqrt{2}}\frac{Q}{\omega_0^2} \tag{A.20}$$

This is true for $4Q^2\delta^2 = 1$ and therefore $\delta = \pm\frac{1}{2Q}$. The half power bandwidths can be solved as

$$\omega_i = \omega_0 \pm \frac{\omega_0}{2Q} \tag{A.21}$$

where $i = 1, 2$ and the approximate bandwidth, B, is given by

$$B = \triangle\omega = \mid \omega_1 - \omega_2 \mid = \frac{\omega_0}{Q} = 2\sigma \tag{A.22}$$

Therefore, for a high quality factor, the quality factor can be approximated by

$$Q = \frac{\omega_0}{\triangle\omega} = \frac{f_o}{\triangle f} \tag{A.23}$$

This gives as an indication of the relationship between the Q factor and the bandwidth. A higher Q factor leads directly to a narrower bandwidth.

## A.2 Individual Quality Factors

The Q factor discussed in the previous section is a characteristic of the resonant circuit in the absence of any loading effects caused by external circuitry. It can be defined as the unloaded Q,

$$Q_0 = \frac{\omega_0 W}{P_0} \tag{A.24}$$

where $P_0$ is the internal power dissipation. For cavity resonators, power is lost through conduction, dielectric losses and radiation. These losses can be used to define individual quality factors $Q_c$, $Q_d$ and $Q_r$ which are respectively defined by conduction, dielectric losses and radiation losses.

Therefore, if the conduction power loss is $P_c$, then $Q_c$ is given by

$$Q_c = \frac{\omega_0 W}{P_c} \tag{A.25}$$

where $\omega_0$ is the resonant radian frequency and W is the maximum stored energy.

For a given dielectric material the relative permittivity, $\epsilon_r$, is defined as

$$\epsilon_r = \frac{\epsilon_c}{\epsilon_0} = \frac{\epsilon - \jmath\frac{\sigma}{\omega}}{\epsilon_0} = \frac{\epsilon}{\epsilon_0} - \jmath\frac{\sigma}{\omega\epsilon_0} = \epsilon' - \jmath\epsilon'' \tag{A.26}$$

where $\epsilon_c$ is the complex dielectric constant of the material and $\epsilon_0 = 8.854 \times 10^{-12}$ farad/meter is the permittivity of free space. The relative permeability is defined as

$$\mu = \frac{\mu}{\mu_0} \tag{A.27}$$

where $\mu_0 = 4\pi \times 10^{-7}$ henry/meter is the permeability of free space. The loss is defined as $\tan\delta = \sigma/(\omega\epsilon)$ where $\sigma$ is the conductivity and $\omega$ is the radian frequency. Therefore the Quality factor due to dielectric losses is defined as [25]

$$Q_d = \frac{\omega_0 W}{P_d} = \frac{\omega_0\epsilon \int \mid E \mid^2 dV}{\sigma \int \mid W \mid^2 dV} = \frac{\omega_0\epsilon}{\sigma} = \frac{1}{\tan\delta} \tag{A.28}$$

Finally, $Q_r$ is affected by the power radiated from the cavity boundaries and can be defined as

$$Q_r = \frac{\omega_0 W}{P_r} \tag{A.29}$$

where $P_r$is the radiated power.

The total power loss is written as $P_o = P_c + P_d + P_r$ and we can write the total unloaded quality factor as

$$Q_o = \frac{\omega_0 W}{P_c + P_d + P_r} \tag{A.30}$$

and therefore we can derive

$$\frac{1}{Q_o} = \frac{P_c}{\omega_0 W} + \frac{P_d}{\omega_0 W} + \frac{P_r}{\omega_0 W} \tag{A.31}$$

It is clear that the lowest Q of the three will dominate the total unloaded quality factor and is approximately equal to $Q_0$. When the resonant circuit is coupled to another circuit, we can define an external Q factor, $Q_e$, dependant on the external circuit. This can be defined as

$$Q_e = \frac{\omega_0 W}{P_e} \tag{A.32}$$

where $P_e$ is the external power loss. The stored energy W, is still the maximum energy stored inside the cavity. The overall Q factor can now be defined as

$$Q_l = \frac{\omega_0 W}{P_t} \tag{A.33}$$

and with $P_t = P_e + P_0$ we can derive

$$\frac{1}{Q_l} = \frac{1}{Q_e} + \frac{1}{Q_0} \tag{A.34}$$

Once again, the lowest quality factor dominates the final quality factor. The following section examines the properties of a parallel RLC resonator.

# Appendix B

# Mathematical Model of Whispering Gallery Modes

This section investigates the characteristics of whispering gallery modes in an unshielded dielectric pill resonator. The model is largely based on the work by Annino [2],[1],[3]. This is not a precise model and several assumptions are made. However, it clearly demonstrates the existence of whispering gallery modes, and the corresponding high Q-factor. Since the emphasis of this section is on the final equations, only the main steps are provided. For a detailed explanation of this model, the reader is referred to [3].

The resonator is modelled as an infinite cylindrical dielectric structure with permittivity $\epsilon_1$ and permeability $\mu_1$ (region 1) surrounded by a medium with permittivity $\epsilon_2$ and permeability $\mu_2$ (region 2). The radius of the cylinder is defined as $a$. The elementary solutions of the wave equation in terms of cylindrical co-ordinates can be written as [28]

$$\Phi_{zn}(\rho,\phi,z,t) = C(n)Z_n(\beta\rho)e^{(jn\phi-j\gamma z+j\omega t)} \tag{B.1}$$

where $n$ defines the number of angular variations, and $w = 2\pi f$ defines the radian frequency. The solutions of $Z_n(\beta\rho)$ are Bessel functions. In region 1 the solutions are Bessel functions of the first kind, $J_n(\beta_1\rho)$, and the argument $\beta_1$ can be defined as $\beta_1^2 = \epsilon_1\mu_1\omega^2 - \gamma^2 = \kappa_1^2 - \gamma^2$. Here $\gamma$ is defined as the axial propagation constant and $\beta_1$ is the radial propagation constant in region 1. Similarly in region 2, outside the cylinder, the solutions are Hankel functions $H_n^{(2)}(\beta_2\rho)$ where $\beta_2$ is defined as $\beta_2^2 = \epsilon_2\mu_2\omega^2 - \gamma^2 = \kappa_2^2 - \gamma^2$. In this case it is assumed that $\mu_1 = \mu_2 = \mu_0$, where $\mu_0$ is the permeability of free space.

By applying boundary conditions, the following characteristic equation can be derived [28]:

$$\left[\frac{J_n'(u)}{uJ_n(u)} - \frac{H_n^{(2)'}(v)}{vH_n^{(2)}(u)}\right]\cdot\left[\epsilon_1\frac{J_n'(u)}{uJ_n(u)} - \epsilon_2\frac{H_n^{(2)'}(v)}{vH_n^{(2)}(u)}\right] = \frac{n^2h^2}{\omega^2\mu_0\epsilon_0}\left(\frac{1}{u^2}-\frac{1}{v^2}\right)^2 \tag{B.2}$$

where $u = \beta_1 a$ and $v = \beta_2 a$.

Equation B.2 is a transcendental equation giving the eigenvalues for $\gamma$. The associated eigenfunctions are the modes of the electromagnetic waves propagating in the structure. From the boundary conditions it can be derived that $\kappa_1^2 > \gamma^2 > \kappa_2^2$, where $\epsilon_1 > \epsilon_2$. It can also be proved [31] that the solution of the Bessel equation is oscillating for $\rho > \rho_c$ and monotonically decreasing for $\rho < \rho_c$. The surface

$$\rho_c = \frac{|\, n \,|}{\beta_1} = \frac{|\, n \,|}{\sqrt{\kappa_1^2 - \gamma^2}} \tag{B.3}$$

defines the modal caustic, which is shown in Figure B.1. The radiation in the cylinder propagates confined between the caustic and the rim. The modal caustic corresponds to the envelope of rays of the considered resonant mode. Particular solutions of equation B.2 can be defined as whispering gallery modes if the caustic is very close to the surface of the cylinder.

The behavior of the electromagnetic waves can be modelled by expanding the modes of the cylinder as plane waves with complex axial propagation. From this model, Annino [3] proves that for $\mathrm{Re}\,(h) < \kappa_2$ a critical angle

$$\Theta_e = \sin^{-1}\left(\frac{\epsilon_2}{\epsilon_1}\right)^{\frac{1}{2}} \tag{B.4}$$

can be defined, where $\Theta_e$ is defined as the travelling waves' critical angle of incidence at the radial boundary. A general angle of incidence is defined in Figure B.1. The damping will be negligible only if the radiation has an angle of incidence at the radial boundary of the cylinder that is greater than $\Theta_e$. This gives an indication of the conditions necessary for low radiation loss at the radial boundary.

From the definition of the critical angle, the surface at which total internal reflection occurs can be defined as follows

$$\rho_p = a \cdot \sqrt{\left(\frac{\epsilon_2}{\epsilon_1}\right)} \tag{B.5}$$

This corresponds to the envelope of rays which incide at the limit angle on the curved surface of the cylinder. The corresponding field distribution has losses weak enough to have a resolved spectrum and a true resonant behavior for incident angles larger than the critical angle. [1]

Using a geometrical optics solution, the problem at the radial boundary can be be looked at from another angle. Figure B.1 shows the modal caustic $\rho_c$ and the angle of incidence, $\Theta_i$, of the propagation in the radial plane. The angle of incidence $\Theta_i$ can be written in terms of the modal caustic as

$$\Theta_i = \sin^{-1}\left(\frac{\rho_c}{a}\right) = \sin^{-1}\left(\frac{n}{\beta_1 a}\right) \tag{B.6}$$

This shows that as the modal index, $n$, increases (and the ray of the caustic increases), the condition $\Theta_i > \Theta_e$ is fulfilled and whispering gallery losses decrease. From the following

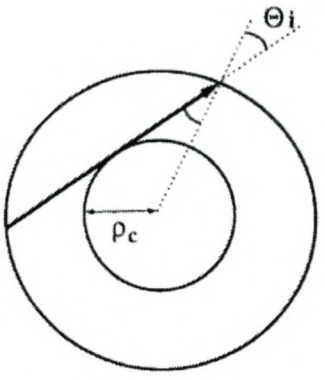


**Figure B.1:** *Cross-section of the dielectric cylinder with the optical ray representing the radiation propagating tangentially to the caustic. The figure is a surface in the $\rho$-$\Phi$ plane*

discussion it is possible to derive a minimum $n$ for which the structure will support a whispering gallery mode. The minimum allowed modal caustic is reached when $\rho_c = \rho_p$. In other words

$$\frac{n}{\beta_1} = a\sqrt{\frac{\epsilon_2}{\epsilon_1}} \tag{B.7}$$

$$\rightarrow n_{min} = \beta_1\, a\sqrt{\frac{\epsilon_2}{\epsilon_1}} \tag{B.8}$$

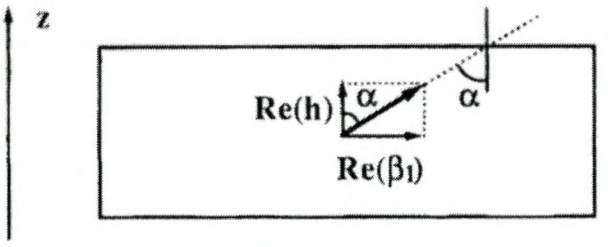


**Figure B.2:** *Schematic representation of propagation inside a finite cylinder. The figure is a surface in the $z$-$\rho$ plane*

The condition for low radiation loss from the axial boundary is also determined from the condition of total reflection. Figure B.2 shows the propagation in the $z$-$\rho$ plane. Total reflection occurs at the boundary if

$$\sinh(\alpha) > \sqrt{\frac{\epsilon_2}{\epsilon_1}} \tag{B.9}$$

where $\alpha$ is defined as the travelling waves' angle of incidence at the axial boundary. Therefore the condition for axial propagation under the weak loss limit becomes

$$\mathrm{Re}\{\gamma\} \leq \sqrt{\left(1 - \frac{\epsilon_2}{\epsilon_1}\right)} \cdot \kappa_1 \tag{B.10}$$

Therefore one can assume that $\mathrm{Re}\{\gamma\} \approx 0$.

A maximum value is assigned to the modal caustic and to the angular variation $n$, by the energy dissipation due to dielectric loss. By calculating the absorption of the infinite homogenous medium in terms of a relative wavelength, Annino [2] derived $n_{max} = 1/\tan\delta$. The Raleigh Criterion was assumed in order to obtain a resolved resonance spectrum. (Effective interference between the input wave and the wave resulting from infinite round-trips along the resonator). The Q factor was solved as $Q \approx (\tan\delta)^{-1}$. This demonstrates the dependance of the Q factor on the material properties.

To summarize: a whispering gallery mode is a low loss mode with a high angular constant. To test for the presence of the mode one can test if the angle of incidence at the cylinder boundary is greater than the critical angle ($\Theta_i > \Theta_e$). This implies that

$$\frac{n_{min}}{\beta_1 a} = \sqrt{\left(\frac{\epsilon_2}{\epsilon_1}\right)} \tag{B.11}$$

Therefore the amount of radiation from the radial boundary is minimal. This also implies that $a > \rho_c > \rho_p$ and the resonant mode is confined effectively. For low losses at the axial boundary, the axial propagation constant should be low. (Annino assumed that $\gamma = 0$ in his simplified model)

# Appendix C

# Sinusoid Integrations

The following integrations of hyperbolic sinusoids are required for determining the inner products in radial mode matching as described in Section 3.2.2. The answers to the integrations are given below.

- $$\int_0^{l_1} \sinh(xz)\sinh(yz)dx = \frac{x}{x^2-y^2}\left(\sinh(yl_1)\cosh(xl_1)\right) - \frac{y}{x^2-y^2}\left(\sinh(xl_1)\cosh(yl_1)\right) \tag{C.1}$$

- $$\int_{l_1}^{l_2} \sinh(x(L-z))\sinh(yz)dx = -X\cosh(xL) + Y\sinh(xL) \tag{C.2}$$

where

$$X = \frac{1}{2}\left(\frac{\sinh((x+y)l_2) - \sinh((x+y)l_1)}{x+y} - \frac{\sinh((x-y)l_2) - \sinh((x-y)l_1)}{x-y}\right)$$

and

$$Y = \frac{1}{2}\left(\frac{\cosh((x+y)l_2) - \cosh((x+y)l_1)}{x+y} - \frac{\cosh((x-y)l_2) - \cosh((x-y)l_1)}{x-y}\right)$$

- $$\int_{l_2}^{L} \sinh(x(L-z))\sinh(y(L-z))dx = \tag{C.3}$$
$$\frac{x}{x^2-y^2}\sinh(y(L-l_2))\cosh(x(L-l_2)) - \frac{y}{x^2-y^2}\sinh(x(L-l_2))\cosh(y(L-l_2))$$

- $$\int_0^{l_1} \cosh(xz)\cosh(yz)dx = \frac{1}{2(x+y)}\sinh((x+y)l_1) \quad (C.4)$$
$$-\frac{1}{2(x-y)}\sinh((x-y)l_1) \quad (C.5)$$

- $$\int_{l_1}^{l_2} \cosh(x(L-z))\cosh(yz)dx = X\cosh(xL) - Y\sinh(xL) \quad (C.6)$$

where

$$X = \frac{1}{2}\left(\frac{\sinh((x+y)l_2) - \sinh((x+y)l_1)}{x+y} + \frac{\sinh((x-y)l_2) - \sinh((x-y)l_1)}{x-y}\right)$$

and

$$Y = \frac{1}{2}\left(\frac{\cosh((x+y)l_2) - \cosh((x+y)l_1)}{x+y} + \frac{\cosh((x-y)l_2) - \cosh((x-y)l_1)}{x-y}\right)$$

- $$\int_{l_2}^{L} \sinh(x(L-z))\sinh(y(L-z))dx = \frac{1}{2(x+y)}\sinh((x+y)(L-l_2)) \quad (C.7)$$
$$+\frac{1}{2(x-y)}\sinh((x-y)(L-l_2))$$

- $$\int_0^{l_1} \cosh(xz)\sinh(yz)dx = \frac{1}{2(x+y)}(\cosh((x+y)l_1) - 1) \quad (C.8)$$
$$= -\frac{1}{2(x-y)}(\cosh((x-y)l_1) - 1) \quad (C.9)$$

- $$\int_{l_1}^{l_2} \cosh(x(L-z))\sinh(yz)dx = X\cosh(xL) + Y\sinh(xL) \quad (C.10)$$

where

$$X = \frac{1}{2}\left(\frac{\cosh((x+y)l_2) - \cosh((x+y)l_1)}{x+y} - \frac{\cosh((x-y)l_2) - \cosh((x-y)l_1)}{x-y}\right)$$

and

$$Y = \frac{1}{2}\left(-\frac{\sinh((x+y)l_2) - \sinh((x+y)l_1)}{x+y} + \frac{\sinh((x-y)l_2) - \sinh((x-y)l_1)}{x-y}\right)$$

- $$\int_{l_1}^{l_2} \sinh(x(L-z))\cosh(yz)dx = X\sinh(xL) - Y\cosh(xL) \tag{C.11}$$

where

$$X = \frac{1}{2}\left(\frac{\sinh((x+y)l_2) - \sinh((x+y)l_1)}{x+y} + \frac{\sinh((x-y)l_2) - \sinh((x-y)l_1)}{x-y}\right)$$

and

$$Y = \frac{1}{2}\left(\frac{\cosh((x+y)l_2) - \cosh((x+y)l_1)}{x+y} + \frac{\cosh((x-y)l_2) - \cosh((x-y)l_1)}{x-y}\right)$$